The Dissertation Committee for Hai-En Tsai
certifies that this is the approved version of the following dissertation:

Tunable Quasi-monoenergetic Compton X-ray Source from Laser-plasma Accelerator

Committee:

Michael Downer, Supervisor

Todd Ditmire

Boris Breizman

John Keto

Adela Ben-Yakar

Tunable Quasi-monoenergetic Compton X-ray Source from Laser-plasma Accelerator

by

Hai-En Tsai, B.S.; M.S.

DISSERTATION

Presented to the Faculty of the Graduate School of

The University of Texas at Austin

in Partial Fulfillment

of the Requirements

for the Degree of

DOCTOR OF PHILOSOPHY

THE UNIVERSITY OF TEXAS AT AUSTIN

May 2015

Dedicated to my parents.

Acknowledgments

I would like to express my deepest gratitude to my advisor, Dr. Michael Downer, for his belief in my abilities by signing me up immediately to the terawatt laser wakefield accelerator project. I still remember my first day joining our group, when he clearly showed me the challenges and importance of this project, he told me " This is a very good project for you to start with." Over time, under his support and guidance, he has been proven right as we have conquered numerous tasks and made progress that has benefited the scientific community. This project indeed starts my research career. I owe a great deal of gratitude to Dr. Michael Downer. He is not only a great physicist but also a visionary.

My sincere appreciation is extended to Dr. Xiaoming Wang for his advise, understanding, patience, and most importantly, his friendship during my graduate studies at UT. I learned a great deal from him of how to work as a serious scientist and, at the same time, an enjoyable person. This work can not be done without him.

I would also like to thank Dr. Chih-Hao Pai for his guidance and expertise during the early stage of constructing a new experimental system. I gratefully thank Josheph Shaw for his teamwork and encouragement during the most critical stage without getting any result to achieving wonderful result.

I truly appreciate Dr. Alex Arefiev and Mr. Xi Zhang for their contribution on simulation work. My grateful thanks are also extended to Dr. Rafal Zgadzaj and Dr. Watson Henderson for their relentless devotion in developing hardware and software for all laser users. I would also like to thank all of the members of Dr. Downer's Femto group, especially Dr. Farbod Shafiai, Mr. Rick Korzekwa and Mr. Vincent Chang for generously sharing me their optics or laser time, Mr. Loucas Loumakos for some needed humor in what could have otherwise been a stressful laboratory environment.

During the experiment, it was indeed stressful when we tried many things without seeing good result. But I always remember the moment, late at night, when Xiaoming, Joey and I saw the CBS signal for the first time, we were jumping up and down. I will always remember that exciting moment as a decoration of an experimentalist.

I have been deeply honored and thankful for being able to work with these most brilliant scientists, physicists, teammates, and friends. You have given me the most valuable inspirations and support. I feel very privileged to have six years of my life experience here. Finally, for those who are about to be or still struggling experimentalists, I solute you!

Tunable Quasi-monoenergetic Compton X-ray Source from Laser-plasma Accelerator

Publication No. _____

Hai-En Tsai, Ph.D.
The University of Texas at Austin, 2015

Supervisor: Michael Downer

This work present an in-depth experimental study of the parameters necessary to optimize a tunable, quasi-monoenergetic, efficient, low-background Compton backscattering (CBS) x-ray source that is based on the self-aligned combination of a laser-plasma accelerator (LPA) and a plasma mirror (PM). The main findings are: (1) an LPA driven in the blowout regime by 30 TW, 30 fs laser pulses produces not only a high-quality, tunable, quasi-monoenergetic electron beam, but also a high-quality, relativistically intense ($a_0 \sim 1$) spent drive pulse that remains stable in profile and intensity over the LPA tuning range. (2) A thin plastic film near the gas jet exit retro-reflects the spent drive pulse efficiently into oncoming electrons to produce CBS x-rays without detectable bremsstrahlung background. Meanwhile anomalous far-field divergence of the retro-reflected light demonstrates relativistic "denting" of

the PM. Exploiting these optimized LPA and PM conditions, we demonstrate *quasi-monoenergetic* (50% FWHM energy spread), *tunable* (75 to 200 KeV) CBS x-rays, characteristics previously achieved only on more powerful laser systems by CBS of a split-off, counter-propagating pulse. Moreover, laser-to-x-ray photon conversion efficiency ($\sim 6 \times 10^{-12}$) exceeds that of any previous LPA-based quasi-monoenergetic Compton source. Particle-in-cell simulations agree well with the measurements.

Table of Contents

List of Tables

List of Figures

Chapter 1

Introduction

Since W. C. Röntgen first discovered x-rays in 1901, x-ray sources have evolved into one of the twenty-first century's most important tools for new discovery. Many Nobel prizes (thirteen in physics, nineteen in chemistry and two in medicine) have been awarded for work using x-rays and associated techniques, including F. Crick, J. Watson, R. Franklin and M. Wilkins for their discovery of the DNA double helix (1962) and three of the most recent laureates — M. Karplus, M. Levitt and A. Warshel — for development of multi-scale models for complex chemical systems associated with x-ray crystallography (2013).

Accelerator-based x-ray sources — including synchrotrons and x-ray free electron lasers — are at the cutting edge of modern x-ray science. However, these "fourth generation" sources are among the largest and most expensive of scientific instruments, and are challenging for much of the scientific community to access on a regular basis. The goal of the research reported in this dissertation was to democratize advanced x-ray science by developing a bright, compact, short-pulsed, narrow bandwidth hard x-ray source for the next generation of small laboratory investigators. This goal was success-

fully realized. The source's tabletop size will enable industrial applications and transform scientific research in various fields, including chemistry [7], medicine [38, 108], x-ray computerized tomography (CT) [51], and photo nuclear activation [57, 90]. The source's narrow spectral bandwidth enables higher signal-to-noise ratio than conventional broadband bremsstrahlung x-rays in spectroscopic applications. The source's femtosecond (fs = 10^{-15}s) pulse duration can resolve atomic motion in condensed matter, where chemical reactions, phase transitions, and surface processes are ultimately driven by the motion of atoms on the time scale of 100 fs. The source's coherence will enable interferometric x-ray imaging. Finally, these advanced capabilities come with a peak brilliance $\sim 10^{19}$ photons s^{-1} mm^{-2} $mrad^{-2}$ per 0.1% bandwidth in the photon energy range 100 to 200 keV that rivals that of large-scale synchrotron sources. Furthermore, the source appears scalable to photon energies of *tens of MeV* (*i.e.* gamma rays) with similar peak brilliance, using capabilities available in our laboratories. Such an extension would give science a bright, directional, femtosecond-pulsed gamma ray source well beyond the capabilities of any conventional light source that would have applications in nuclear spectroscopy and homeland security.

The x-ray source developed here is based on recent advances in the acceleration of electrons to relativistic energy via femtosecond laser-plasma interaction. Laser-plasma electron accelerators are noteworthy for their compactness and extraordinary beam quality: high brightness, low emittance, short pulse duration. Within the past decade, table-top laser-plasma accelerators

(LPAs) — also known as laser-wakefield accelerators (LWFAs) — have emerged [30, 35, 70] that accelerate electrons *nearly mono-energetically* to hundreds of MeV within a few millimeters, or to several GeV within a few centimeters. These LPAs operate in the so-called "bubble regime" [83], a reference to the bubble-shaped, micrometer-sized electron density cavity that the drive laser pulse creates in the plasma by its light pressure, or ponderomotive force. Ambient plasma electrons streaming around the walls of the positively-charged, light-speed bubble converge at its rear, where slight perturbations in the bubble's shape and size as it propagates can induce their injection into, and capture within, the bubble's enormous internal electrostatic field [49]. Since all such electrons enter the bubble at nearly the same point, they accelerate quasi-mono-energetically toward the center of the bubble as it propagates through the plasma in the wake of the drive laser pulse. The trapped, accelerated electrons are then released when the drive laser and bubble reach the end of the millimeter/centimeter-scale plasma medium. For example, in Prof. Downer's 30-terawatt laser lab, $\sim$ 100 pC electron bunches of $\sim$ 100 MeV energy (*i.e.* relativistic Lorentz factor $\gamma \sim 200$) with less than 10 percent energy spread are produced routinely [102], while 2 GeV ($\gamma \sim 4000$) electrons with $\sim$ 5% energy spread are produced at the Texas Petawatt laser facility [107]. Section 2.2 summarizes the physics of LPAs in the bubble regime.

Compton backscatter (CBS) produces femtosecond duration, narrow bandwidth, hard x-rays by colliding a laser pulse with a relativistic electron beam. The electric field oscillations of the laser pulse act as a mini-undulator,

inducing the relativistic electrons to emit coherent x-rays along their propagation direction. In the past, CBS relied on kilometer-long, conventional linear accelerators to produce x-rays [37, 64, 89]. Compact LPA electron sources now enable high-quality tabletop CBS x-ray sources compatible with small university laboratories. We can't always provide a college student in Physics access to a linear accelerator of kilometer length. But now, with advances such as those reported in this dissertation, we can give her/him a mini-accelerator and mini-undulator for advanced x-ray studies. She/he can thereby access unprecedented research opportunities and applications previously unaffordable for a small university lab. This project is thus important for both research and education.

Prior to this dissertation work, CBS x-rays had been generated from LPAs by two methods. In the first, a 100 TW laser system supplied both 1.9 J, 35 fs LPA drive pulses and 0.5 J, 90 fs split-off backscatter pulses. The latter were focused to spot size $w_0 = 22\mu$m, intensity $a_0 \approx 0.3$ onto electrons emerging from the LPA to generate quasi-monoenergetic tunable CBS x-rays up to MeV photon energy [13, 82]. Here $a_0 \equiv eE_{\rm L}/m\omega c = 0.85\sqrt{\lambda^2(\mu{\rm m})I(10^{18}{\rm W/cm}^2)}$ — where $E_{\rm L}$ is the electric field of the laser pulse of frequency ω, wavelength λ, intensity I, and e and m are electron charge and mass, respectively — is a dimensionless laser strength parameter defined such that laser-electron interactions are relativistic for $a_0 \geq 1$. Under these conditions, stable overlap of backscatter pulse and LPA electrons was achieved despite shot-to-shot pointing fluctuations, as indicated by the high

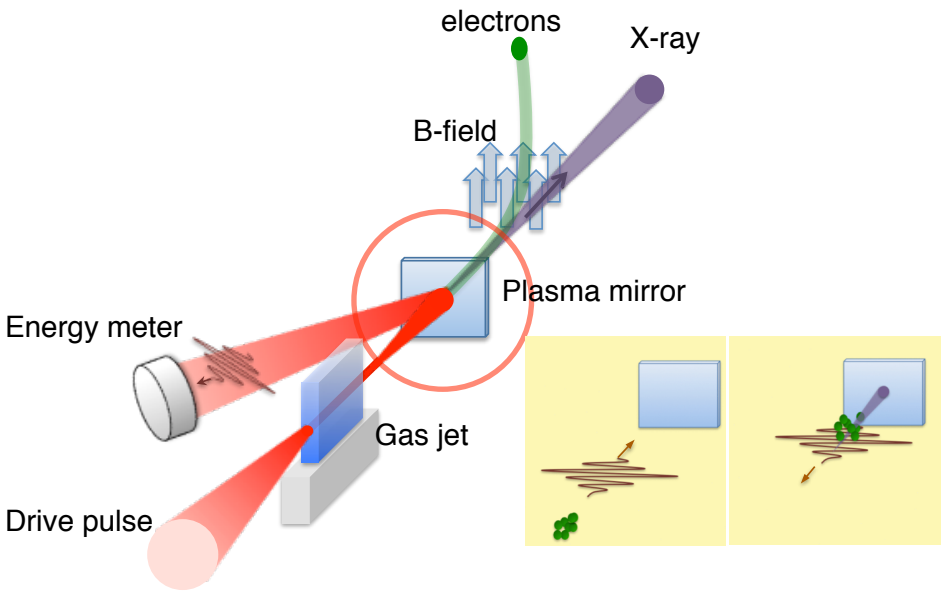

Figure 1.1: Schematic of CBS x-ray source. An ultra-intense laser pulse (red) drives the LPA in a gas jet. A plasma mirror subsequently retro-reflects the spent drive pulse into trailing relativistic electrons after the LPA, as shown in the inset (yellow region). CBS x-rays and accelerated electrons then propagate through the plasma mirror for measurement and analysis.

reproducibility ($> 93\%$) and photon number stability (60%) of the CBS x-rays [13, 82]. Nevertheless, the difficulty of overlapping counter-propagating, micron-size electron and laser beams reliably and regularly remains a major drawback of this method. In the second method, a 30 TW laser system — three times smaller than the laser system used for first method — directly supplied only $\sim$ 1 J, 35 fs LPA drive pulses. A plasma mirror (PM) then retro-reflected the drive pulse into the trailing relativistic electrons after the LPA [98]. Fig. 1.1 shows a schematic of this method, which is *self-aligning*, and thus eliminates sensitivity to laser pointing fluctuations even for very small

spot sizes. It is thus an attractive LPA-based Compton x-ray source for laboratories (like ours) with smaller (tens of TW) laser systems. However, prior to the work of this dissertation, *tunable*, *quasi-monoenergetic* x-rays had not been demonstrated by this method, only broadband x-rays centered at ~ 50 KeV [98]. Moreover, key parameters that determine x-ray brightness, such as the intensity and spatial profile of the laser pulse after driving the LPA and reflecting from the PM, had not been measured, let alone optimized.

This work is an in-depth study of the parameters necessary to optimize CBS x-ray generation — *i.e.* to generate *tunable*, *quasi-monoenergetic* CBS x-rays with *high conversion efficiency* and *low background* — using the self-aligned combination of LPA and PM (the second method). In this study, we produced high quality, relativistic, quasi-monoenergetic, tunable electron bunches from a laser-plasma accelerator (LPA) by optimizing laser and plasma parameters in the bubble regime. We then fully characterized the laser pulse spatial intensity profile immediately after driving the LPA and after reflecting from the PM by both measurement and simulation. There are three major findings from the study. First, a mildly relativistic ($a_0 \approx 1.6$) incident laser pulse remains relativistic ($1 < a_0 < 2$) and of high beam quality after driving an LPA in the bubble regime. Moreover, its intensity profile remains stable as the LPA plasma density $\bar{n}_e$ changes from 1.4 to 2.2×10^{19} cm^{-3}, a range over which electrons remain quasi-monoenergetic ($10-20\%$ FWHM energy spread) and collimated, but tune in energy from 60 to 90 MeV. This a_0 exceeds that achieved using a split-off backscatter pulse, suggesting that a future nonlinear

Compton source [81, 88] may be more readily achievable for some LPAs via the PM method. The detailed experimental results regarding LPAs and laser quality are presented in chapter 3. Second, the PM yielded near unity reflectance at $a_0 \sim 1$, an intensity regime for which PM reflectivity has not been well characterized. This suggests that prepulses, a major source of declining PM reflectivity at relativistic intensity, are suppressed by the act of driving an LPA in the bubble regime. Moreover, use of a plastic film only 90 μm thick for the PM rendered transmitted bremsstrahlung radiation undetectable, resulting in a very high signal-to-noise ratio Compton source. Third, our measurements of far-field angular divergence of the retro-reflected drive pulse together with simulations of its interaction with the PM show that the PM surface curved relativistically [24, 106]. This confirms that the spent drive pulse is relativistically intense, and suggests that higher x-ray yield may be achievable in future work by optimizing this curvature to focus the retro-reflected drive pulse onto trailing electrons. The detailed experimental and simulation results regarding PMs are presented in chapter 4.

Based on findings of this study, we demonstrate generation of quasi-monoenergetic (50% FWHM energy spread), tunable (75 to 200 keV photon energy) CBS x-rays by the LPA-PM method for the first time. Fig. 1.1 shows a schematic diagram of the CBS x-ray source developed in this work. X-ray energy was tuned by varying $\bar{n}_e$, and thus electron energy, over a range that preserved narrow electron energy spread and stable, relativistic spent drive pulse intensity profile. Previously, quasi-monoenergetic, tunable CBS x-rays

had been generated from LPAs only by the split-off pulse method [13, 82]. Moreover, we demonstrate photon conversion efficiency $\sim 6 \times 10^{-12}$ from laser pulse to x-rays that is higher than achieved so far using a split-off scattering pulse by factors ranging from six [13] to thirty [82]. It is thus the highest conversion efficiency so far demonstrated for a LPA-based quasi-monoenergetic Compton source. This high efficiency is the result of our coordinated achievement, and detailed characterization, of a stable spent LPA drive pulse profile with $a_0 \approx 1$ that reflects with near-unity efficiency from a PM that guarantees excellent overlap with 150 pC, quasi-monoenergetic electron bunches. This unique convergence of conditions has been achieved and characterized in this work for the first time [103]. Chapter 5 is a summary of this work including CBS x-ray, LPAs and PMs.

The tunable LPA electron and CBS x-ray sources were developed in Prof. Downer's University of Texas Tabletop Terawatt (UT^3) laser lab. This lab's commercial (Thales Laser) 30-TW laser system operates with 10-Hz repetition rate at central wavelength 800 nm. Appendix A shows the schematic building blocks of this Titanium:Sapphire chirped pulse amplifier (CPA) laser system. In the experiments reported herein, the 30fs, 1J, linearly-polarized laser pulses produced by this system were focused to peak intensity $6 \times 10^{18}\mathrm{W/cm^2}$, equivalent to the intensity obtained by focusing the total sunlight incident on Texas to a 10 μm spot. The CBS x-ray source has been operational for less than one year. Thus we have only begun to explore its possible applications. Chapter 6 lays out detailed experimental plans for what

lies ahead of us.

The next chapter surveys the main elements of laser-plasma interaction physics that underlie the experiments described in subsequent chapters. These elements include the propagation of intense laser pulses in plasma, laser-plasma electron acceleration, plasma mirror reflection, and light scatter from free electrons.

Chapter 2

Laser-matter interaction

The development of ultra-intense lasers based on the chirped pulse amplification (CPA) technique [67, 74, 96] has opened up the new field of "relativistic optics" [75]. In the relativistic optics regime, exposure to light intensity exceeding $\sim 10^{18}$ W/cm^2 induces electrons to oscillate with relativistic velocity. As a result, several fascinating new phenomena occur, including relativistic self-focusing [93], wakefield generation [101], relativistic transparency [46], relativistic plasma mirror (PM) [24], self modulation [48], and nonlinear Thomson scattering [29].

In this chapter, we will focus on relativistic laser-matter interactions that are directly related to the analysis of our experiments: laser-plasma accelerators, plasma mirrors, and Compton backscattering. No attempt is made to describe the underlying physics of each effect exhaustively, nor to derive equations rigorously. Instead, I will summarize well-established facts and elaborate on examples related to the experiments.

First, an overview of laser propagation in underdense plasma is presented. Nonlinear propagation leads naturally to a discussion of laser-plasma accelerations (LPAs). The second section discusses several types of LPAs in-

cluding the basic laser-wakefield accelerator (LWFA), the self-modulated laser-wakefield accelerator (SM-LWFA) and the highly nonlinear blow-out regime, also known as the "bubble" regime. The third section briefly overviews the plasma mirror (PM), a relativistic optics device to which our work makes a substantial new contribution. Finally, we discuss Compton backscattering (CBS) in the linear regime in an all-optical setup. This last section will be the basis for analyzing backscattering experiments described in chapter 5.

2.1 Laser pulse propagation in a plasma

When a laser pulse propagates in a plasma, the electric field of the laser pulse exerts a force on the charged particles. The simplest result of this force is oscillatory particle motion at the optical frequency ω. Additionally, gradients in the cycle-averaged field amplitude of the pulse give rise to a cycle-averaged "ponderomotive" force that creates a plasma wave. The response of the plasma to these forces can be treated with two-fluid theory. One fluid consists of the light, fast, oscillating electrons, which support electron-density (Langmuir) waves. The other consists of heavy, slow oscillating ions, which support ion-acoustic waves. Ion movement can be neglected in our case, because the laser-plasma interaction occurs on a time scale (< 1 ps) shorter than an ion-acoustic wave period. The plasma wave, therefore, can be characterized by an electron oscillation frequency $\omega_p = (e^2 n_e/\epsilon_0 m_e)^{1/2}$, where n_e is electron density, m_e electron mass, and ϵ_0 vacuum permittivity. The dispersion relation of the linear wave equation in a uniform plasma is given by

$$\omega^2 = {\omega_p}^2 + k^2c^2. \tag{2.1}$$

The wavenumber k becomes imaginary when $\omega_p > \omega$. Consequently the forward-propagating light wave rapidly attenuates, since plasma electrons respond collectively on a time scale $1/\omega_p$ shorter than the optical period $1/\omega$, and thus screen the field. For a given frequency ω, the critical density n_c is defined by the condition $\omega_p = \omega$. For electron density $n_e > n_c$ — *i.e.* an "overdense" plasma — forward propagation is impossible. When a light wave propagating in vacuum impinges on an interface with overdense, collisionless plasma it is totally reflected. This is the basis of the plasma mirror (PM) discussed in Section 2.3. For example, the critical density for laser light of $\lambda = 800$ nm, as used in our experiment, is $n_c = 1.1 \times 10^{21}/\lambda^2[\mu m^2]$ cm^{-3} $= 1.7 \times 10^{21}$ cm^{-3}. Underdense (overdense) plasma is the common term to describe target material with density lower (higher) than critical density.

When an ultra-short pulse is focused to intensity $I \sim 5\times10^{18}$ W/cm^2 in a He gas jet, the leading edge of the pulse begins to ionize He gas through multi-photon and tunneling ionization [18] at an intensity of only 10^{14} W/cm^2. Thus the laser front edge has fully ionized the He gas and created plasma before the main pulse arrives. The resulting variation of plasma electron density alters the plasma refractive index, which from Eq. 2.1 is given by

$$\eta = ck/\omega = \sqrt{1 - \omega_p^2/\omega^2} = \sqrt{1 - n_e/n_c}. \tag{2.2}$$

Variations in η, in turn, alter the propagation of the laser pulse. For example,

transverse spatial variations in n_e (and therefore in η) can deflect or defocus the pulse; rapid temporal variations in n_e induce frequency shifts.

2.1.1 Linear propagation

When plasma density and light intensity are low enough, a laser pulse propagates essentially as in vacuum. The criterion for linear propagation is that the phase shift $\Delta\phi$ caused by the laser-matter interaction (*e.g.* by laser ionization or Kerr effect) is too small to distort the wavefront significantly. Near the focal spot, the laser electric field can be approximated by a plane wave $E(z,t) = E_0 \exp(-i\phi)$, where $\phi = k_0\eta(t)z - \omega_0 t$ is the phase of the wave, k_0 the vacuum wavenumber, $\eta(t)$ the time-dependent refractive index of the plasma. Time-dependence can arise, for example, from rapid ionization. For $\omega \gg \omega_p$, $n_e \ll n_c$, The refractive index Eq. 2.2 can be approximated as

$$\eta(t) \approx 1 - \frac{n_e}{2n_c} \tag{2.3}$$

For a fully ionized plasma, ion density $n_i = Zn_e$, where Z is the number of electrons per atom. Thus for a fully ionized He plasma ($Z = 2$), the phase shift along the propagation axis can be written as

$$\Delta\phi = k_0 \frac{n_i}{n_c} \Delta z, \tag{2.4}$$

where Δz is propagation distance into the plasma. For a non-uniform He plasma, one should substitute $\int n_i(z)dz$ for $n_i\Delta z$. For the propagation to be considered linear, the phase shift should satisfy $\Delta\phi \ll 1$. As an example,

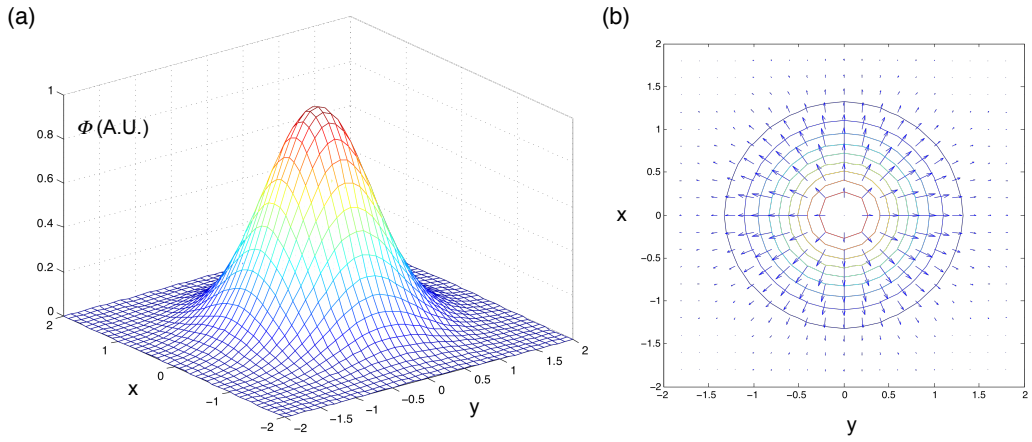

Figure 2.1: (a) Ponderomotive potential of a Gaussian laser pulse. (b) Corresponding ponderomotive force vector field.

for a laser pulse of wavelength 800 nm ($n_c = 1.7 \times 10^{21} cm^{-3}$) propagating in homogeneous plasma of length $\Delta z = 3$ mm, as used in our experiments, gas density n_i has to be lower than 10^{17} cm^{-3} for propagation to be altered negligibly by the plasma refractive index. Since, in fact, $n_i \sim 10^{19}$ cm^{-3} in these experiments, nonlinear propagation effects are very important.

2.1.2 Nonlinear propagation

In contrast to the linear regime, a laser pulse with higher intensity, or that propagates in denser plasma, propagates differently than in vacuum. A sufficiently intense pulse can relativistically alter η, or re-distribute plasma density by creating a plasma wave. The plasma refractive index then depends on laser intensity, which is the hallmark of nonlinear propagation.

Ponderomotive self-focusing

The ponderomotive force $\vec{F}_P$ is a cycle-averaged, nonlinear force that a particle of charge e, mass m experiences in an inhomogeneous electromagnetic field of amplitude $|E|$, frequency ω, and is given by

$$\vec{F}_P = -\frac{e^2}{4m\omega^2}\vec{\nabla}|E|^2. \tag{2.5}$$

The ponderomotive force is directed along the gradient of laser intensity. Thus for a Gaussian pulse, electrons are expelled from the center of the pulse. Fig. 2.1 shows the cycle-averaged ponderomotive potential ϕ_P and the corresponding effective ponderomotive field $\vec{E}_P = -\vec{\nabla}\phi_P$ of a Gaussian pulse. A laser pulse with a Gaussian transverse intensity distribution drives electrons away from the propagation axis until the electrostatic space charge force balances the ponderomotive force. At high laser intensity, the ponderomotive force can lead to complete cavitation [56]. For a long pulse or continuous beam, these opposing forces result in a steady-state transverse electron density distribution $n_e(r)$. One can then rewrite Eq. 2.2 as

$$\eta(r) = \sqrt{1 - \frac{n_e(r)}{n_c}}, \tag{2.6}$$

to indicate that the index depends on r. The effect of a transversely varying $\eta(r)$ depends on the intensity and duration of the pulse and the plasma density. For a transversely Gaussian pulse that is strong enough to ionize a gas, but not strong enough to exert a significant ponderomotive force on the resulting plasma, the foot of the pulse often creates a radial density gradient $\partial n_e/\partial r < 0$,

corresponding to a radial index gradient $\partial\eta/\partial r > 0$, due to stronger ionization on axis. This index gradient is equivalent to a negative lens for the main part of the pulse — *i.e.* the phase velocity $v_{ph} = c\eta(r)$ is faster on axis than away from the axis. Consequently the pulse de-focuses. This effect is called plasma de-focusing, or plasma lensing. For a more intense pulse, the ionization front is created earlier, but a later, more intense part of the foot of the pulse can create a radial density gradient $\partial n_e/\partial r > 0$ ($\partial\eta/\partial r < 0$) of opposite sign by ponderomotively pushing plasma away from the axis. This index gradient is equivalent to a *positive* lens, and causes the main part of the pulse to focus. This effect is called ponderomotive self-focusing. Finally, for ultrashort ($\tau \sim \omega_p^{-1}$), ultra-intense pulses, the delay of order ω_p^{-1} for the ponderomotive density gradient to form must be taken into account. In this case, ponderomotive self-focusing is not instantaneous, but instead increases dynamically during the pulse.

Relativistic self-focusing

An electron in an intense laser field oscillates with relativistic velocity. Its mass is therefore increased by the Lorentz factor $\gamma = \gamma(r)$, which has a spatial dependence matching that of the laser intensity profile. This in turn decreases ω_p and increases n_c by the same factor $\gamma(r)$. Replacing n_c with $\gamma(r)n_c$, the refractive index becomes

$$\eta(r) = \sqrt{1 - \frac{n_e}{\gamma(r)n_c}} \tag{2.7}$$

For mildly relativistic intensity ($a_0 \leq 1$), electrons oscillate mainly

along the electric field vector and $\gamma = \sqrt{1 + (p/mc)^2} \approx 1 + a^2/2$. Therefore an intensity gradient $\partial a^2/\partial r < 0$ implies a refractive index gradient $\partial\eta/\partial r < 0$ that supports self-focusing. The total intensity-dependent refractive index in the regime $\omega_p \ll \omega$ considering ponderomotive and relativistic effects is then

$$\eta(r) \approx (1 - \frac{n_e}{2n_c})(1 - \frac{a^2}{2} + \frac{\delta n}{n_0}) \tag{2.8}$$

where the $a^2/2$ term comes from relativistic self-focusing, and $\delta n_e/n_0$ from ponderomotive self-focusing. Here δn represents the ponderomotive perturbation of homogeneous plasma density n_0 such that $n_e = n_0 + \delta n$.

The critical power P_c for relativistic self-focusing is defined as the laser power at which relativistic self-focusing balances diffraction, and can be shown [75, 97] to depends on laser frequency and plasma frequency according to

$$P_c = \left(\frac{m_e c\omega}{e\omega_p}\right)^2 \simeq 17\left(\frac{\omega}{\omega_p}\right)^2 [GW] = 17\frac{n_c}{n_e}[GW]\,. \tag{2.9}$$

The last two expressions are "engineering" formulas for convenient numerical estimates. For example, as noted earlier $n_c = 1.7 \times 10^{21}$ cm^{-3} for 800 nm light. Thus if a laser pulse with $\lambda = 800$ nm enters a plasma with $n_e = 10^{19} cm^{-3}$, $P_c \approx 3$ TW. Powers $P > 3$ TW are readily achievable with modern lasers, which can exceed PW powers. For example, a laser delivering 30 fs pulses with an energy of 1 J has a peak power of 30 TW.

2.2 Laser-plasma accelerator (LPA)

Tajima and Dawson originally proposed laser-plasma accelerators (LPA) over 35 years ago (1979) [99]. Today plasma-based accelerator research has ex-

panded world-wide, with major experimental programs in Germany, France, Taiwan, Korea, Japan, the United Kingdom and the United States. This expansion was fueled by development, refinement and commercialization of chirped-pulse amplified (CPA) laser systems, pioneered by Mourou and colleagues [5, 74, 80, 96].

LPA experiments prior to 2004 achieved accelerating fields > 100 GV/m, electron energy up to ~ 100 MeV and accelerated charge > 1 nC [60, 69, 73, 76, 101, 104]. However, the electron beam quality was far from ideal. The electron energy distribution typically resembled a decaying exponential, with most electrons < 10 MeV, and only an exponential tail extending to ~ 100 MeV. For practical purposes, the energy spread was $\Delta E/E \sim 100\%$, and applications of the electron beams were thus severely limited.

Groundbreaking progress was made in 2004 when three groups [30, 35, 70] simultaneously reported acceleration of ~ 100 pC of electrons to ~ 100 MeV with *small* energy spread $\Delta E/E \sim 10\%$. Such high-quality e-bunch production is now understood to be a result of the so-called "bubble" regime [83], in which ambient plasma electrons self-inject into the nearly spherical accelerating cavity at a precise spatiotemporal point, leading to quasi-monoenergetic acceleration. In subsequent years, further improvements in electron energy and beam quality have been achieved through more precise control of laser and plasma parameters, by extending laser propagation distance using plasma waveguides, by understanding underlying physics better, and by matching dephasing, depletion and acceleration lengths. For example, using plasma-

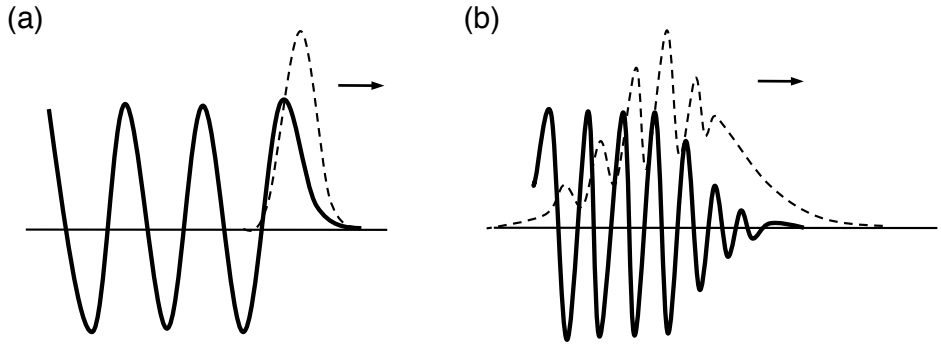

Figure 2.2: Schematic of LPAs: (a) resonant LWFA, (b) self-modulated (SM) LWFA. Shown are the excited plasma wave potentials (solid lines) and right-moving laser intensity envelopes (dashed lines).

channel guided laser, quasi-monoenergetic electron bunches up to 1 GeV were demonstrated in 2006 [62]. Methods for controlled injection of electrons into the wakefield using a colliding laser pulse were demonstrated around the same time [31], and yielded energy spread of $\Delta E/E \sim 1\%$ as well as tunable energy. Highly stable electron bunches were demonstrated by introducing plasma density down ramps [34]. Quasi-monoenergetic electron bunches up to 2 GeV were produced from tenuous ($n_e \sim 10^{17}$ cm^{-3}) plasma of few cm length using the Texas PW laser [107], and 4-GeV bunches were recently demonstrated at the Berkeley Laboratory Laser Accelerator (BELLA) [61]. High quality GeV e-bunches open a wide variety of applications of LPAs, such as front-end injectors for conventional accelerators and drivers for compact short-pulse coherent x-ray sources.

This section provides an overview of the physics of LPAs, in which charged particles are accelerated by plasma waves excited by short-pulse, high-

intensity lasers. There are various LPA configurations, specifically the standard quasi-linear resonant laser wakefield accelerator, which I will denote simply as "LWFA", the self-modulated LWFA, and the highly nonlinear regime of electron cavitation (bubble regime). Fig. 2.2 shows LWFA and self-modulated LWFA configurations schematically.

The accelerating gradients of plasma accelerators are three orders of magnitude higher than those of conventional RF linear accelerators (linacs), which are limited to ~ 100 MV/m due to breakdown at the wall of the structure. The ionized plasma can sustain plasma waves with huge electric fields $E_0 = mc\omega_p/e$ or

$$E_0(\mathrm{V/m}) \simeq 96\sqrt{n_e(\mathrm{cm}^{-3})}. \tag{2.10}$$

For example, $n_e = 10^{19}$ cm^{-3} yields $E_0 \simeq 300$ GV/m. In addition to large accelerating gradients, plasma accelerators can produce very short electron bunches. The longitudinal extent of the bunch is less than a plasma wavelength

$$\lambda_p(\mu\mathrm{m}) = \frac{2\pi c}{\omega_p} = 3.3 \times 10^{10}/\sqrt{n_e(\mathrm{cm}^{-3})}. \tag{2.11}$$

For example, $\lambda_p = 10$ μm for $n_e = 10^{19}$ cm^{-3}. The accelerating e-bunch must fit within half a plasma wavelength to experience an accelerating potential. Thus the temporal duration of an accelerated e-bunch satisfies $\tau_b < \lambda_p/2c$, which means $\tau_b < 16$ fs for $n_e = 10^{19}$ cm^{-3}. In LPAs that accelerate quasi-monoenergetically, τ_b is much less than this upper limit, in order that all electrons in the bunch experience a similar accelerating gradient.

Another important parameter in the discussion of laser-plasma interaction is the laser strength parameter a_0, defined formally as the peak amplitude of the normalized vector potential of laser field $a_0 = eA_0/m_e c^2$. Here A_0 is the amplitude of the usual vector potential $\vec{A}$, which is related to the optical electric field $\vec{E}$ by $\vec{E} = -\partial\vec{A}/\partial t$. The parameter a_0 is related to peak intensity I_0 by $I_0 = (\pi c/2)(mc^2 a_0/e\lambda)^2$, which yields

$$a_0 = 0.85\,[\lambda(\mu\text{m})]\sqrt{I_0(10^{18}\ \text{W/cm}^2)}. \tag{2.12}$$

Physically, $a_0 = p_\perp/m_e c$ is the transverse "quiver" momentum of an electron in the laser field, normalized to $m_e c$. Equivalently, $a_0 = W_L/m_e c^2$ is the work $W_L = eE_L\lambda$ that the laser field E_L does on the electron over a characteristic distance λ, normalized to $m_e c^2$. Using either reasoning, when $a_0 > 1$, the electron quiver motion is relativistic, which requires laser intensities $I > 10^{18}$ W/cm^2 for laser wavelength $\lambda \sim 1$ μm. Such laser intensities are routinely obtained by table-top Ti:S laser systems based on the CPA technique.

2.2.1 Laser wakefield accelerator

The standard laser wakefield accelerator (LWFA) is driven by a single, short (< 1 ps), high intensity ($> 10^{17}$ W/cm^2), laser pulse as shown in Fig. 2.2(a). The ponderomotive force of the intense laser pulse expels plasma electrons from within its envelope as it propagates through the plasma. The LWFA is driven most efficiently at "resonance" — *i.e.* when the laser pulse length L is on the order of the plasma wavelength $\lambda_p \sim L$. The "standard" LWFA is defined to operate near the resonance condition. When Tajima and

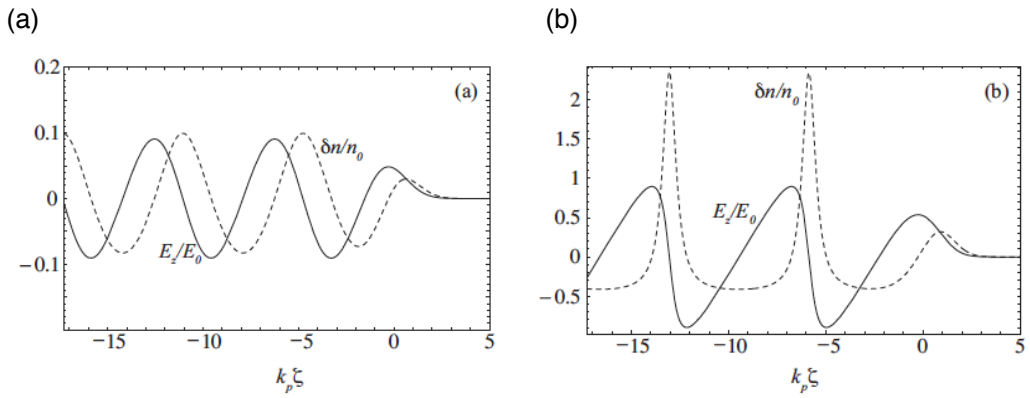

Figure 2.3: Time averaged density variation $\delta n/n_0$ (dashed) and corresponding electric field E_z/E (solid) in an LWFA driven by a Gaussian laser pulse centered at $k_p\zeta = 0$ with intensity length $L = k_p^{-1}$. (a) $a_0 = 0.5$ and (b) $a_0 = 2.0$. From Esarey *et al.*, 2009 [26]

Dawson first proposed the LWFA in 1979 [99], the technology of generating subpicosecond laser pulses was not available yet. Gorbunov and Kirsanov (1987) [41] and Sprangle *et al.* (1988)[95] later reinvented the idea of LWFA after Mourou and colleagues demonstrated table-top TW CPA laser systems [67]. Fig. 2.3 shows a plasma wave driven by a linear polarized Gaussian pulse with the form $a = a_0 \exp(-\zeta^2/4L^2)\cos(k\zeta)$, where pulse length $L = 1/k_p$. Here $\zeta = z - v_g t$ is the longitudinal coordinate in the reference frame of the drive pulse propagating at its group velocity v_g. The solid curve represents the perturbation of plasma density $\delta n/n_0$ and its corresponding normalized axial electric field E_z/E (dashed curve) driven by a mildly relativistic pulse $a_0 = 0.5$ (a) and a highly relativistic pulse $a_0 = 2.0$ (b). For the mildly relativistic pulse, the wakefield is nearly sinusoidal in shape, and its amplitude scales nearly linearly with the amplitude of the drive pulse. These are hall-

marks of a "quasilinear" LWFA. For the highly relativistic pulse, $\delta n/n_0$ and E_z/E become non-sinusoidal, the amplitude of $\delta n/n_0$ saturates near 1, and the period lengthens slightly. These are hallmarks of a "nonlinear" LWFA. The strongly nonlinear LWFA eventually transitions to the "bubble" regime.

2.2.2 Self-modulated laser wakefield accelerator

The first laser wakefield accelerators to be demonstrated in the laboratory were driven by laser pulses much longer than a plasma wavelength ($L \gg \lambda_p$) in plasmas of near atmospheric density ($n_i \sim 10^{19}$ cm^{-3}) [48]. Such high plasma density proved necessary to self-inject electrons into the plasma wave, but laser systems generating TW pulses as short as the plasma period ($\tau_p \sim 10$ fs) were not yet available. Thus available $\tau \sim 1$ ps pulses were used. Much to the surprise of the early investigators, strong collimated MeV electron beams were generated, indicated a high amplitude wake, despite the far off-resonant excitation condition. The explanation that soon emerged was that the long laser pulse ($L \gg \lambda_p$) broke up into a train of short pulses, each with $L \sim \lambda_p$, thereby satisfying the resonant driving condition. This process is called the self-modulation instability. Since forward Raman scattering occurs simultaneously[59], the process is alternatively called the forward Raman instability [28]. The modulation occurs because an initial low-amplitude electron density wave $\delta n(\zeta)/n_0$ creates alternating regions of low and high refractive index within the drive pulse envelope at the peaks and valleys, respectively, of the plasma wave. The local group velocity decreases/increases at

peaks/valleys, causing the pulse amplitude to modulate. The resulting modulated envelope reinforces growth of the plasma wave, which in turn modulates the drive pulse envelope more strongly. The resulting accelerating structure, which is a plasma wave with $\delta n/n_0 \sim 1$, is called the self-modulated LWFA [48, 63, 68].

As a numerical example, consider driving a plasma wake with a 500 fs ($L = 150$ μm) laser pulse of wavelength $\lambda = 1$ μm, power $P = 30$ TW. To drive a standard LWFA, the resonant condition $L \sim \lambda_p$ implies density $n_e = 4.4 \times 10^{16}$ cm^{-3}. However, relativistic self-guiding is negligible at such low density, since $P_c = 425$ TW $\gg 30$ TW (see Eq. 2.9). Moreover, self-injection of electrons does not occur[33]. In contrast, operating in the self-modulated LWFA regime allows both self-guiding and self-injection by using a higher plasma density. To achieve self-guiding, choose a plasma density such that $P = 2P_c$, which implies $n_e = 1.3 \times 10^{18}$ cm^{-3} (Eq. 2.9), about 30 times higher than for the standard LWFA, and $\lambda_p = 30$ μm. Thus $L = 5\lambda_p$, so the self-modulation instability breaks the incident drive pulse into ~ 5 sub-pulses during the interaction. It turns out that self-injection is easily achieved at this density and power. Thus the self-modulated LWFA produces copious electron output, albeit with wide energy spread, whereas the standard LWFA produces nothing. This is why the self-modulated LWFA became the most popular mode of LWFA operation during the decade 1994 to 2004.

To summarize, the self-modulated LWFA has three advantages over the standard LWFA. First, since the self-modulated LWFA operates at higher

plasma density (for given drive pulse duration), it supports a larger accelerating field $E_z \propto \sqrt{n_e}$. Second, also because of higher density, the self-guiding condition $P \gg P_c > 1$ is more readily achieved, yielding longer interaction length with higher a_0, and thus larger E_z. Third, also because of higher density, self-injection occurs more readily. Higher density is also the source of the main *disadvantages* of the self-modulated LWFA. First, the drive laser pulse group velocity, and thus the wakefield phase velocity, is smaller, limit dephasing length and useful acceleration distance. For this reason, self-modulated LWFAs never produced electrons much more energetic than ~ 100 MeV, and usually much less. Secondly, due to the small λ_p and easy self-injection, electrons inject continuously into all portions of the plasma wave. Consequently energy spread was $\sim 100\%$. Even when the tail of the distribution reached ~ 100 MeV, most of the electrons produced had energy < 10 MeV.

2.2.3 Bubble accelerator

The "bubble" regime is an extreme nonlinear version of the standard LWFA, driven by a laser pulse of length Ł $< \lambda_p$ above the wave breaking threshold that is strong enough to completely remove plasma electrons from a region of length $\sim \lambda_p$ behind the pulse. As shown in Fig. 2.4, the laser wake is shaped as a solitary cavity behind a few cycle laser pulse. Ultrashort, quasi-monoenergetic electron bunches emerge from the wake as a low-emittance beam. Discovery of the bubble regime followed the development of terawatt-class laser systems that produced pulses of duration $\tau \leq 30$ fs.

Nevertheless, about two years before the first experimental demonstrations [30, 35, 70], Pukhov and Meyer-ter-Vhen [83] first noticed the unique characteristics of the bubble regime, which they called the "highly nonlinear broken-wave regime", in three-dimensional particle-in-cell simulations. The important features they noticed were localized electron injection into the rear of the electron density cavity, and, as a result, quasi-monoenergetic ($\Delta E/E < 0.1$) electron acceleration. Pukhov and Meyer-ter-Vehn correctly recognized that the ability to produce quasi-monoenergetic, self-injected electron bunches was a major advance over the then popular self-modulated LWFA, since it preserved the advantages of easy self-injection and self-guiding, while overcoming the major disadvantage of wide energy spread. Accordingly, they submitted their paper to the journal *Nature*. However, it was rejected on the grounds that the results were of little practical importance. Events soon proved that judgment to be incorrect.

The first experimental results in the bubble regime were demonstrated in 2004 by three groups [30, 35, 70]. They produced quasi-monoenergetic electron bunches above 100 MeV with few percent energy spread, using a few tens of TW laser system with $\sim$ 30 fs pulse duration. Quasi-monoenergetic GeV-class electron bunches were later produced in the bubble regime by self-guided PW laser pulses propagating in centimeter-long low density (10^{17} cm^{-3}) plasma [107] or by PW pulses propagating in a preformed centimeter-long plasma channel [52, 61, 62].

Scaling laws and rules of thumbs for optimizing laser-plasma accel-

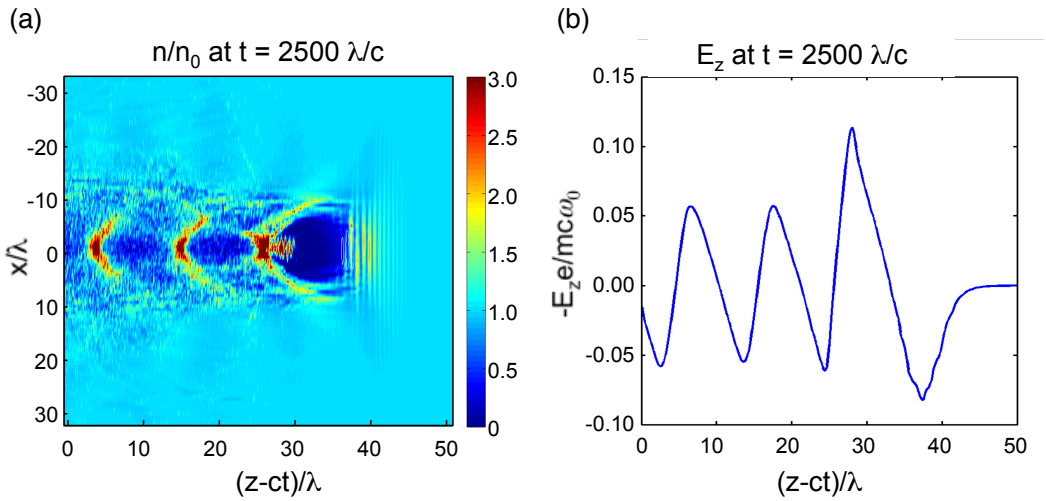

Figure 2.4: 3D simulation by Xi Zhang [65, 103] using the code VLPL [84] for a 30 TW laser pulse with $w_0 = 10$ μm, $a_0 \sim 1.5$, propagating in plasma with density 1.5×10^{19} cm^{-3}. (a) A 2-D (x-z plane) view of the accelerating structure and self-trapped electrons in the first accelerating bucket at propagation distance $z = 2$ mm. Color scale shows electron density in units of 10^{19} cm^{-3}. (b) A line out of the longitudinal wakefield at $z = 2$ mm, showing the wakefield reaches $0.1|eE_z/mc\omega_0|$ within the first bucket.

erators in the bubble regime have now been developed, based on computer simulations [66] and experimental results. The laser pulse length $c\tau$ should be no greater than the blow out radius R (which is on the order of λ_p) — *i.e.* $\tau \leq R/c$ — and focused laser spot size w_0 should be close to $c\tau$. The laser strength parameter a_0 and R are related by

$$k_p R \approx 2\sqrt{a_0}, \tag{2.13}$$

where k_p is the plasma wave number. This equation expresses the balance between the laser ponderomotive force and the electrostatic force of the ion cavity $E_r \sim k_p R$.

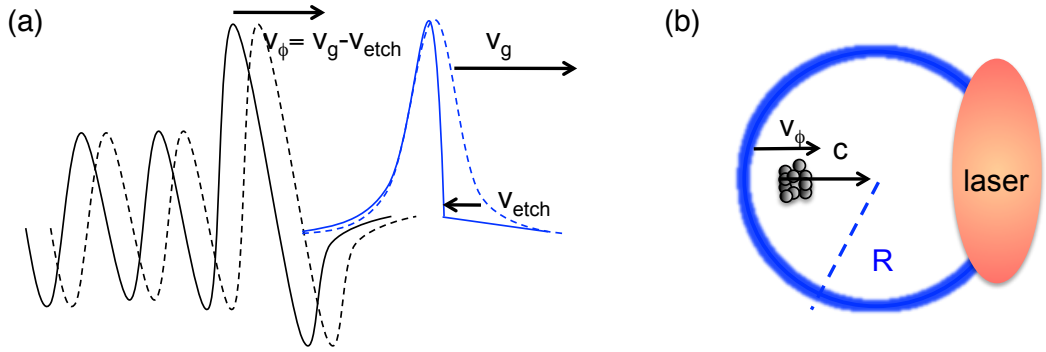

Figure 2.5: (a) Schematic illustration of the effective velocity of the drive laser pulse and the phase velocity of the wake $v_\phi = v_g - v_{etch}$ (solid blue curve), where v_g is group velocity of laser light (dashed, blue), v_{etch} is etching velocity. (b) Schematic illustration of dephasing. In the rest frame of a bubble, the time for the trapped electrons to move from the rear to the center is $t_{dph} = R/(c - v_\phi)$.

During laser propagation, the laser pulse front etches back due to local pump depletion, as shown in Fig. 2.5(a). 1D simulations yield etch velocity $v_{etch} \sim c\omega_p^2/\omega^2$ [19]. The pump depletion length is therefore

$$L_{dpl} = \frac{c}{v_{etch}} c\tau_{FWHM} \simeq \frac{\omega_0^2}{\omega_p^2} c\tau_{FWHM}. \tag{2.14}$$

The effective velocity of the drive pulse, and thus the phase velocity of the wake, is then $v_\phi \simeq v_g - v_{etch}$, where group velocity $v_g \simeq c(1 - \omega_p^2/2\omega^2)$ for $\omega_p << \omega$. The result is $v_\phi \simeq c(1 - 3\omega_p^2/2\omega^2)$. The dephasing length L_{dph} — *i.e.* the propagation distance over which trapped electrons outrun the wake [Fig. 2.5(b)] — is proportional to the time $t_{dph} = R/(c - v_\phi) = L_{dph}/c$ for trapped electrons to move from the rear to the center of the bubble in the rest frame of the bubble, yielding

$$L_{dph} = \frac{cR}{c - v_\phi} \simeq \frac{2\omega_0^2}{3\omega_p^2} R. \tag{2.15}$$

Under optimum conditions ($c\tau \approx w_0 \approx \sqrt{a_0}c/\omega_p$) trapped electrons accelerate monoenergetically to energy [66]

$$E_e \approx 0.16mc^2 \frac{c\tau}{w_0}(\frac{P}{P_{rel}})^{2/3}(\frac{n_c}{n_p})^{1/3}, \tag{2.16}$$

where P is laser power, $P_{rel} \sim 8.5$ GW is a relativistic power unit. The number of electrons so accelerated is [66]

$$N_e \approx \frac{0.53}{k_0 r_e}\sqrt{\frac{P}{P_{rel}}} \tag{2.17}$$

where $r_e = e^2/4\pi\epsilon_0 mc^2$ is classical electron radius.

For our experimental parameters — a 30 TW, 30 fs laser pulse focused to $w_0 = 10\mu m$, $a_0 \sim 1.6$ in plasma of density $n_e \sim 10^{19}$ cm^{-3} ($\lambda_p \sim 10\mu$m) — one expects the bubble to balance at $R \sim 5\mu$m, from Eq. 2.13. From Eq. 2.14, $L_{dpl} \sim 1mm$. From Eq. 2.15), $L_{dph} \sim 0.3$ mm. From Eq. 2.16, $E_e \sim 75$ MeV. From Eq. 2.17, $N_e \sim 230$ pC. These estimates agree fairly well with observed parameters of our accelerator.

Table 2.1 lists selected milestone LWFA experiments carried out over the last 20 years in various regimes. Before the advent of TW short-pulse lasers, early experiments exploited a long-pulse beat-wave scheme, and accelerated electrons up to tens of MeV (Ebrahim *et al.*, 1985 [25]). Since the mid-1990s, efforts in this fields have been concentrated on the short-pulse schemes (Nakajima *et al.*, 1995 [76]) described earlier in this chapter. The results using matched, ultrashort, strongly relativistic laser pulses achieve the bubble regime, and produce quasi-monoenergetic electron spectra (Mangles *et*

Authors, year [Ref.]	Laser	τ_L	E_L (J)	I_p (W/cm2)	L_p (mm)	Type	Energy (MeV)
Ebrahim, 1985 [25]	CO2	1.2ns	50	3×10^{13}	0.5	BW	3.5
Nakajima, 1995 [76]	Nd:glass	1ps	30	10^{17}	0.6	SMWF	18
Umstadter, 1996 [104]	Ti:sapphire	400fs	3	4×10^{18}	0.75	guided WF	2.5
Moore, 1997 [101]	Nd:glass	400fs	1	5×10^{18}	0.6	SMWF	30
Gordon, 1998 [42]	Nd:glass	1ps	20	6×10^{18}	1	SMWF	94
Chen, 1999 [14]	Nd:glass	400fs	2	10^{19}	-	SMWF	40
Malka, 2002 [68]	Ti:sapphire	30fs	1	3×10^{18}	1	forced WF	200
Mangles, 2004 [70]	Ti:sapphire	40fs	0.5	2×10^{18}	0.6	forced WF	70
Geddes, 2004 [35]	Ti:sapphire	55fs	0.5	10^{19}	2	guided WF	86
Faure, 2004 [30]	Ti:sapphire	30fs	1	3×10^{18}	-	bubble	170
Tsai, 2012 [102]	Ti:sapphire	30fs	1	6×10^{18}	3	bubble	100
Wang, 2013 [107]	Nd:glass	150fs	100	6×10^{18}	70	bubble WF	2000
Leemans, 2014 [61]	Ti:sapphire	40fs	16	6×10^{18}	90	guided WF	4200

Table 2.1: A sampling of major LWFA experiments since 1985.

al. [70], Geddes *et al.* [35], and Faure *et al.* [30], 2004). The multi-GeV landmarks were reached recently by Wang *et al.*, 2013 [107] and Leemans *et al.*, 2014 [61].

2.3 Plasma mirror (PM)

Plasma mirrors (PMs) have become standard tools for improving the temporal contrast [23, 36, 50, 111] and spatial profile [40] of intense, ultrashort laser pulses from modern chirped pulse amplified (CPA) laser systems [5, 74, 80, 96]. PMs are solid or liquid [6] targets with low reflectivity for low intensity light, but that switch almost instantaneously to high reflectivity for light intense enough to generate overdense plasma in the target by multiphoton or optical field ionization. The strategy behind contrast/profile improvement is to focus the incoming pulse to a fluence (typically $3 - 300$ J/cm^2 for pulses

of few tens to few hundred fs duration [23, 36, 111]) at which unwanted prepulses and spatial wings are transmitted, whereas the main pulse is reflected as a result of generating plasma above the critical density. For pulses with contrast ratios typical of the output of CPA systems, the main pulse typically reaches an intensity in the range $10^{15} < I < 10^{17}\mathrm{W/cm^2}$ as it reflects from the PM [6, 23, 36, 40, 50, 100, 111]. A pulse thus cleaned by reflecting from one or more primary PMs can subsequently be focused to ultra-relativistic intensity ($I >> 10^{18}$ W/cm^2 for visible or near infrared wavelengths), where its highly nonlinear interaction with a secondary PM can be studied without preexpanding its surface [100]. However, when pulses are focused to relativistic intensity at the primary PM, contrast and profile usually suffer because of premature generation of overdense plasma, which partially reflects the temporal pedestal and wings, and premature hydrodynamic expansion of the PM surface, which distorts the wave front of the reflected main pulse [106]. Recently new applications have emerged that demand high reflectivity at light intensities in the range from 10^{17} to 10^{19} W/cm^2 directly from a primary PM surface. These include retro-reflection of the transmitted drive pulse of a LWFA to produce Compton backscatter x-rays [98, 103], and recycling of such a drive pulse to multi-stage a LWFA [94]. In addition, even for studies primarily devoted to highly nonlinear laser-PM processes such as high-order harmonic generation [9, 100, 105], vacuum heating [10, 43, 58], hole-boring[109], or relativistic transparency [79], quantitative characterization of the reflectivity of the main pulse provides a valuable diagnostic of its relativistic interaction with the target

surface. We will present the first detailed experimental and simulation study of the reflectivity of a PM excited directly at relativistic intensity in chapter 4 and the result of its relativistic application in chapter 5.

2.4 Thomson scattering and Compton scattering

Thomson scattering is classical elastic light scattering from free electrons in the regime in which the photon energy is much smaller than the electron rest energy (511 KeV). In ultra-intense laser fields ($a_0 \gg 1$), the electron motion becomes relativistic and the magnetic $\vec{v} \times \vec{B}$ force exerted on electrons can no longer be neglected. We then enter the nonlinear Thomson scattering regime, in which the electron's motion is no longer linearly proportional to the laser electric field. Fig. 2.6, for example, schematically shows the electron's typical figure-8 trajectory in the electron frame when excited mildly relativistically. The emitted radiation now contains harmonics of the fundamental laser frequency[15]. For example, the second-harmonic Thomson-scattered light is observed to be maximum along the y-axis.

Thomson scattering based on the classical EM wave scattering by a charged particle, however, can not explain the shift in wavelength observed at low intensity as the scattered photon energy approaches the electron rest mass energy. In fact, Compton's experiment demonstrated that light behaves like a stream of particles whose energies are proportional to their frequency. This process is called Compton scattering. The interaction between an electron and an energetic photon results in the electron acquiring part of the photon's

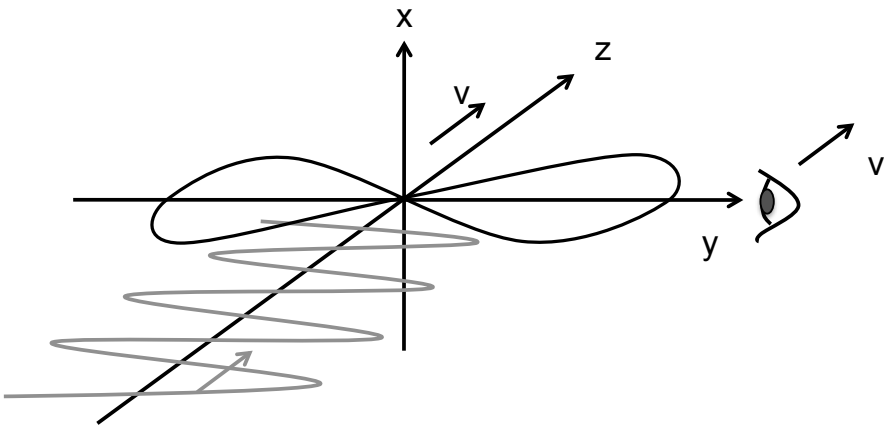

Figure 2.6: Observation of Thomson scattered light. The electromagnetic wave propagates along the z-axis, the electric field is aligned with the y-axis and the electron oscillates in the y-z plane. The electron orbit is shown in the reference frame of the electron (co-moving observer). The second-harmonic Thomson scattered light is observed along the y-axis.

energy, while the photon retains the remaining energy and is emitted in a different direction. Inverse Compton scattering, or Compton backscattering, is a process in which energetic electrons transfer part of their energy to low-energy photons. The photons *gain* energy and shorten in wavelength. For example, the effect is also observed when photons from the cosmic microwave background (CMB) move through the hot gas surrounding a galaxy cluster. One of the more surprising results from X-ray astronomy is that the great volumes of space between galaxies in clusters of galaxies are not empty, as they appear in optical images. Instead, they are filled with a diffuse, hot plasma, with typical temperatures of $T \sim 10^7 - 10^8 K$. The CMB photons are Compton backscattered to higher energies by the electrons in this gas, resulting in the Sunyaev-Zel'dovich effect [8]. Observations of the Sunyaev-Zel'dovich effect

provide a nearly redshift-independent means of detecting density perturbations of the Universe [77].

2.5 Compton Backscatter (CBS) in the linear regime

For the special case of an electron moving relativistically ($\gamma \gg 1$) toward a mildly intense laser pulse ($a_0 < 1$), the scattered photon is relativistically Doppler-upshifted and co-propagates with the electron in the lab frame. Generation of highly directional, narrow bandwidth hard x-ray or γ-ray beams by Compton backscatter (CBS) from relativistic electron beams [11] has many applications including radiation therapy [108], radio surgery [38], industrial CT scanning [51], homeland security [47], and photo-nuclear spectroscopy [57, 90]. For such applications, narrow bandwidth CBS x-rays offer higher signal-to-noise ratio than broadband bremsstrahlung x-rays. High quality CBS x-rays were demonstrated more than a decade ago using conventional electron accelerators [37, 64, 89]. Within the past decade, however, tabletop laser-plasma accelerators (LPAs) [26, 99] that accelerate electrons quasi-monoenergetically [30, 35, 70] to hundreds of MeV [33, 44, 54] or GeV [52, 61, 107] energy within millimeters to centimeters have emerged, opening the possibility of compact CBS x-ray sources compatible with small university laboratories [17, 45, 55]. In this section, I present calculations of the experimental parameters of both electrons and laser pulse needed to optimize CBS.

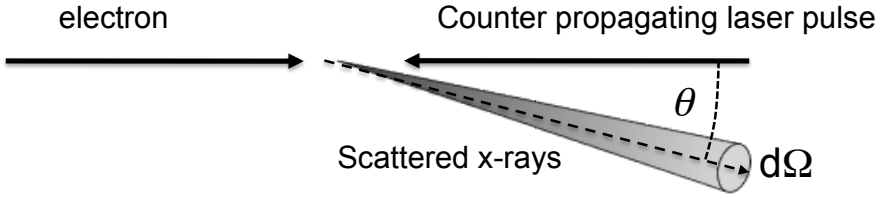

Figure 2.7: Compton backscattering of a weak, non-relativistic laser pulse from a laser accelerated electron. The angle θ is the scattering angle of the photons with respect to the axis, which is also called observation angle. $d\Omega$ is the differential solid angle covered by the detector.

2.5.1 Scattering from a single electron

Considering a non-relativistic laser pulse approaching a counter-propagating electron and scattering from it (see Fig. 2.7). When a *slow* electron oscillates in such a laser field, it radiates in a dipole pattern, which varies slowly with observation angle. If the electron is moving relativistically towards the oncoming laser pulse, on the other hand, it "sees" strongly compressed wavefronts along its propagation direction, due to the relativistic Doppler shift. When this electron, oscillating in this shortened-wavelength field, radiates along its propagation direction, a second Doppler shift shortens the wavelength further. An observer stationed along this direction detects x-ray emission that also varies rapidly in wavelength and intensity as the observation angle changes.

We calculate the CBS radiation in two steps: (1) calculate the scattered radiation pattern in the electron frame of reference; (2) transform it back to the lab frame. The relativistically Doppler-shifted laser wavelength experienced

by the electron in its frame of reference is

$$\lambda_e = \lambda_0 \sqrt{\frac{1-\beta}{1+\beta}} \approx \frac{\lambda_0}{2\gamma}, \tag{2.18}$$

where λ_0 is laser wavelength in the lab frame, λ_e is laser wavelength in the electron frame, $\beta = v/c$, and $\gamma = 1/\sqrt{1-\beta}$ is the Lorentz factor. Comparing the laser field to a static undulator, the relativistic electron experiences a Lorentz-contracted undulator field with wavelength

$$\lambda_e = \lambda_\mu / \gamma \tag{2.19}$$

where λ_μ is the undulator wavelength in the lab frame. The wavelength observed in the lab frame is then

$$\lambda = \lambda_\mu (1 - \beta \cos\theta) \approx \frac{\lambda_\mu}{2\gamma^2}(1 + \gamma^2\theta^2), \tag{2.20}$$

where the last expression is valid for $\theta \ll 1$. Fig. 2.8(a) visualizes Eq. 2.20 for $\gamma = 1.4$ ($v = 0.7c$). Combining Eqs. 2.18, 2.19 and 2.20, one finds

$$\lambda = \frac{\lambda_e}{2\gamma}(1 + \gamma^2\theta^2) = \frac{\lambda_0}{4\gamma^2}(1 + \gamma^2\theta^2). \tag{2.21}$$

Considering radiation emitted only along the z-axis ($\theta = 0$), Eq. 2.21 (rendered in terms of photon energy) simplifies to $\hbar\omega_x = 4\gamma^2\hbar\omega_0$, where ω_x is the CBS frequency, ω_0 the incident laser frequency. The great advantage of CBS over conventional undulators is that the laser wavelength (0.8 μm) is 4 order of magnitude shorter than a conventional undulator period ($\sim$ 1 mm). Consequently the CBS photon energy can be $10^4\times$ higher for a given electron energy. Conversely, the electron energy needed to produce a given x-ray photon energy

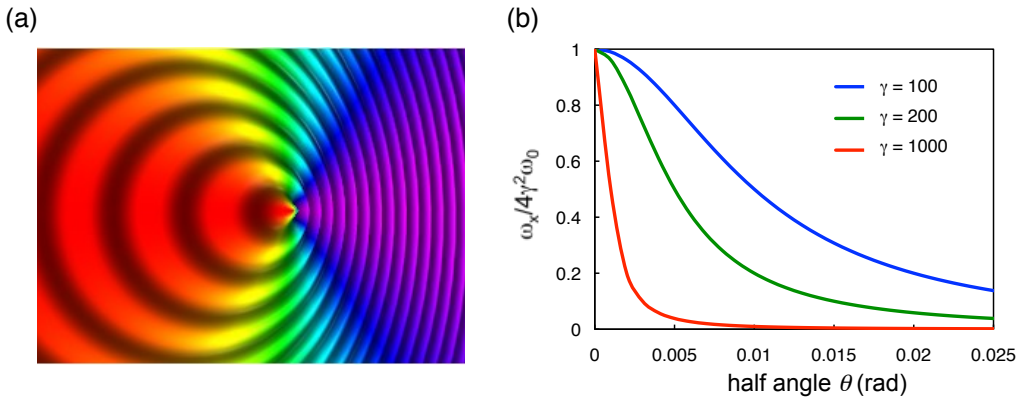

Figure 2.8: (a) A source of light waves moving to the right, relative to observers, with velocity 0.7c. The frequency is higher for observers on the right, and lower for observers on the left. From Wikipedia TxAlien. (b) The normalized scattered photon energy varies as a function of observation angle θ for various electron energy $\gamma = 100, 200, 1000$.

is 100× lower. The emitted radiation has bandwidth $\Delta\lambda_e/\lambda_e \sim 1/N_0$ in the electron frame, where N_0 is the number of laser cycles (or undulator periods). After transforming to the lab frame, we find this bandwidth is emitted into a cone of half angle

$$\theta \sim \frac{1}{\gamma\sqrt{N_0}} \tag{2.22}$$

centered on the electron propagation axis. The higher the electron energy, the smaller the cone angle. Thus for a 100 MeV electron ($\gamma = 196$) colliding with a 30-fs, 800-nm laser pulse, we expect x-ray photon energy 210 KeV on axis, and radiation half-angle $\sim$ 1.4 mrad. The spectral density $d^2I(\theta, \gamma, \omega_x)/d\omega_x d\Omega$ radiated by a single electron per unit frequency $d\omega_x$, per unit solid angle $d\Omega$, can be calculated by integrating the electron's Lièнard-Wiechert potentials. Assuming $a_0 \ll 1$ (so CBS comes mainly from the fundamental frequency),

electrons with $\gamma \gg 1$, and observation angle $\theta \ll 1$, the result is [11, 12, 29]

$$\frac{d^2I}{d\omega_x d\Omega} = r_e mc\gamma^2 N_0^2 a_0^2 (\frac{\omega_x}{4\gamma^2\omega_0})^2 R(\omega_x, \omega_0), \tag{2.23}$$

where r_e is the classical electron radius. The resonance function $R(\omega_x, \omega_0)$ has the form

$$R(\omega_x, \omega_0) = \left[\frac{\sin(\kappa L/2)}{\kappa L/2}\right]^2 \tag{2.24}$$

where $\kappa = k_x(1+\gamma^2\theta^2)/4\gamma^2 - k_0$, k_x and k_0 are CBS and laser wave numbers, respectively, and $L = N_0\lambda_0$ is the interaction length. The condition $\kappa = 0$ corresponds to a Doppler-shifted resonant frequency, which the resonant function is strongly peaked at

$$\omega_r = 4\gamma^2 \frac{\omega_0}{1+\gamma^2\theta^2}, \tag{2.25}$$

or equivalently a resonant electron energy

$$\gamma_r^2 = \frac{\omega_x/4\omega_0}{1-\omega_x\theta^2/4\omega_0}. \tag{2.26}$$

Fig. 2.8(b) shows how normalized CBS photon energy $\omega_r/4\gamma^2\omega_0$ varies with θ for various γ. Clearly CBS photon energy decreases sharply with increasing observation angle, more so as electron energy increases. Thus as electron energy increases, the CBS x-ray beam becomes increasingly collimated.

2.5.2 Scattering from a laser-accelerated electron bunch

The previous section discussed x-ray spectral flux density $d^2I(\theta, \gamma, \omega_x)/d\omega_x d\Omega$ resulting from CBS from a single electron. The total spectral density radiated

by a bunch of electrons is

$$\frac{d^2 I_T}{d\omega_x d\Omega} = \int_0^{\gamma_{max}} f(\gamma) \frac{d^2 I}{d\omega_x d\Omega} d\gamma, \tag{2.27}$$

where $f(\gamma) = \frac{N_e(\gamma)}{d\gamma}/N_b$ is the electron energy distribution of, and N_b the number of electrons in, the bunch. The result depends strongly on the width of the energy distribution $f(\gamma)$, as the following examples illustrate.

CBS spectrum for broad electron energy distribution

Assume $f(\gamma)$ varies slowly compared to $R(\omega_x, \omega_r)$ for fixed ω_x. Beam emittance can be neglected since the angular width of the x-rays typically exceeds the electron beam divergence. For $N_0 \gg 1$, the resonance function R can be approximated as a delta function: $R \approx \Delta\omega_r \delta(\omega_x - \omega_r)$ or $\Delta\gamma_r \delta(\gamma - \gamma_r)$, where $\Delta\omega_r = \omega_r/N_0$ and $\Delta\gamma_r = 2\gamma_r^3 \omega_0/N_0\omega_r$. Therefore,

$$R(\omega_x, \omega_r) = \frac{\gamma_r^3}{2N_0\gamma^2} \delta(\gamma - \gamma_r) \tag{2.28}$$

Combining 2.28, 2.27 and 2.23, one obtains

$$\frac{d^2 I_T}{d\omega_x d\Omega} = \frac{r_e mc}{16} N_0 a_0^2 (\frac{\omega_x}{\omega_0})^{3/2} f\left[\gamma = (\frac{\omega_x}{4\omega_0})^{1/2}\right] \tag{2.29}$$

The number of CBS photon collected within an angle $\theta_c < (\Delta\omega_x/\omega_x)^{1/2}\gamma$ small enough that the intensity distribution is flat over the collecting solid angle $d\Omega = \pi\theta_c^2$, over a small bandwidth $\Delta\omega_x$ can be calculated by dividing Eq. 2.29 by the photon energy $E_x = \hbar\omega_x$ and multiplying by the number of electrons in the bunch N_b

$$N_T = \frac{d^2 I_T}{d\omega_x d\Omega} \frac{1}{\hbar\omega_x} N_b \Delta\omega_x \pi\theta_c^2 \tag{2.30}$$

$$= \frac{\alpha_f}{16} N_0 a_0^2 N_b (\frac{\omega_x}{\omega_0})^{3/2} f\left[\gamma = (\frac{\omega_x}{4\omega_0})^{1/2}\right] \frac{\Delta\omega_x}{\omega_x} \pi\theta_c^2 \tag{2.31}$$

where $\alpha_f = e^2/(4\pi\epsilon_0\hbar c) = 1/137$ is the fine structure constant. The average source brightness is given by

$$B_{ave} = \frac{N_T R_{rep}}{(2\pi r_b \theta_c)^2} = \frac{\alpha_f N_0 a_0^2 N_b R_{rep}}{64\pi r_b^2} (\frac{\omega_x}{\omega_0})^{3/2} f \frac{\Delta\omega_x}{\omega_x} \tag{2.32}$$

in photons s^{-1} mm^{-2} $mrad^{-2}/0.1\%$ BW, where r_b is the electron bunch radius. The peak brightness is $B_{pk} = B_{ave}/(\tau_x R_{rep})$, where τ_x is the x-ray pulse duration, which is approximately equal to the bunch duration.

CBS spectrum for narrow electron energy distribution

The typical electron bunches from laser-bubble accelerators have narrow energy spread ($\Delta\gamma/\gamma \ll 1$, *e.g.* $0.01 - 0.10$). The total number of photons scattered per electron-laser interaction in a specific frequency range $\Delta\omega_x$ ($\Delta\omega_x/\omega_x \ll 1$) per solid angle can be derived from Eq.2.23 and 2.24 by integrating over the range $\Delta\omega_x$, multiplying by the electron number N_b interacting with the laser and dividing by the energy per photon $\hbar\omega$. In particular, the total photon number scattered for narrow energy distribution also derived in previous work[29] is approximately

$$N_T = 2\pi\alpha_f N_0 a_0^2 N_b \frac{\Delta\omega_x}{\omega_x} F_{coll} \tag{2.33}$$

where F_{coll} is a factor determined by the collecting angle, θ_c, of the x-ray detector, and the opening angle of the radiation, θ_T. i.e., $F_{coll} = \theta_c^2/(\theta_c^2 + \theta_T^2)$

$$\theta_T^2 \simeq \left[(\Delta\omega/\omega)^2 + (\Delta\omega/\omega)_0^2 + (\Delta\omega/\omega)_\epsilon^2 + (\Delta\omega/\omega)_i^2\right]^{1/2} /\gamma^2 \tag{2.34}$$

where $(\Delta\omega/\omega)_0 = 1/N_0$, $(\Delta\omega/\omega)_\epsilon = \epsilon_n^2/r_b^2$, ϵ_n is normalized emittance and $(\Delta\omega/\omega)_i = 2\Delta\gamma/\gamma$. The peak brightness is

$$B_{pk} = \frac{N_T}{(2\pi)^2\sigma_r^2\sigma_\theta^2\tau_x} \tag{2.35}$$

where $\sigma_r \simeq r_b$ and $\sigma_\theta \simeq \theta_T$ are source size and divergence angle of the radiation.

2.5.3 Examples based on SM-LWFAs

The SM-LWFA (see Sec. 2.2.2) provides short ($\sim$ 100 fs) electron bunches with a broad energy distribution. Thus CBS using an SM-LWFA injector will be characterized by x-ray photon with broad bandwidth. The approximation $R \approx \Delta\omega_r\delta(\omega_x - \omega_r)$ or $\Delta\gamma_r\delta(\gamma - \gamma_r)$ is valid for this case. The backscattered photon number per frequency interval per unit solid angle can be calculated by dividing Eq. 2.31 by $\Delta\omega_x$ and $\pi\theta_c^2$ and replacing $(\omega_x/4\omega_0)^{1/2}$ by γ:

$$\frac{\Delta N_x}{\Delta\omega_x\Delta\Omega} = \frac{\alpha_f}{8\omega_0}N_bN_0a_0^2\gamma f(\gamma) \tag{2.36}$$

The number of photons detected per energy interval is:

$$\frac{\Delta N_x}{\Delta E_x\Delta\Omega} = \frac{\alpha_f}{8E_0}N_bN_0a_0^2\gamma f(\gamma). \tag{2.37}$$

The CBS photon spectrum is recorded with a constant solid angle with constant energy resolution ΔE_x. In Eq. 2.37, γ can be replaced by $\sqrt{\omega_x/(4\omega_0 - \omega_x\theta^2)}$ or $\sqrt{E_x/(4E_0 - E_x\theta^2)}$ to show its dependence on θ. Assuming an exponential electron energy distribution $f(\gamma) = f_0 exp[-\gamma/T_e]$, Eq. 2.37 becomes

$$\frac{\Delta N_x}{\Delta E_x} = \frac{\alpha}{8E_0}\Delta\Omega N_bN_0a_0^2f_0\sqrt{\frac{E_x}{4E_0 - E_x\theta^2}}exp\left[-\sqrt{\frac{E_x}{4E_0 - E_x\theta^2}}/T_e\right], \tag{2.38}$$

where electron temperature T_e is in units of γ.

Here we use the experimental parameters demonstrated by Schwoerer *et al.* in 2006[92] to verify our calculation. In the experiment, a SM-LWFA driven by a 0.4 J, 85 fs pulse focused to $a_0 \sim 3$ in plasma density of 5×10^{19} cm^{-3} yields $\sim 10^7$ electrons per bunch with an broadband electron distribution($T_e = 7$MeV or $\gamma \simeq 14$). A counter-propagating 40 mJ, 100 fs, $\lambda = 800$ nm laser pulse ($N_0 = 37.5$) at 10 Hz repetition rate was focused to $w_0 = 5\mu$m, $a_0 \sim 0.8$ on the output electron beam. Using Eq. 2.38, CBS photons per shot radiated at all frequencies in the 10mrad collecting angle angle is 10^5, which is in the same order of magnitude as experimental yield, 3×10^4. The average and peak brightness, 10^4 and 10^{16} photons s^{-1} mm^{-2} mrad^{-2}/0.1% BW, respectively, are calculated using Eq. 2.32 and 2.35. Column 2 of Table 2.2 summarizes the calculation parameters and x-ray characteristics. Fig. 2.9(a) shows the backscattered spectrum.

2.5.4 Examples based on bubble accelerator

Column 1 of Table 2.2 lists parameters and x-ray characteristics for CBS from a quasi-monoenergetic electron bunch from a bubble-regime accelerator. Electron beam parameters (70 MeV, 10 fs bunch length, 2% energy spread) from simulations[65, 103] discussed in section 2.2.3 were used; the 800nm, 300mJ, 100fs scattering laser focused to $w_0 = 30\mu$m to achieve $a_0 \sim 0.6$ was assumed. On-axis CBS photon energy, 113KeV, is predicted using Eq. 2.25. For 10 Hz repetition rate and 5 mrad collecting angle, from

Parameter	Bubble accelerator	SM-LWFA
Laser λ_L	0.8	0.8
Laser pulse energy (J)	0.3	0.04
Laser pulse duration (FWHM)(fs)	100	100
a_0	0.6	0.8
Laser cycle N_0	37.5	37.5
Electron beam energy γ	137	exponential
Electron number	1.25×10^9	10^7
Electron spot size (μm)	6	6
Collecting angle (mrad)	5	10
Repetition rate (Hz)	10	10
Ave. brightness (ph $s^{-1}mm^{-2}mrad^{-2}$/0.1%BW)	3×10^9	10^4
Peak brightness (ph $s^{-1}mm^{-2}mrad^{-2}$/0.1%BW)	3×10^{22}	10^{16}
Total photon number /shot	1×10^7	10^5
X-ray pulse (fs)	10	100
X-ray photon energy (KeV)	113	broadband

Table 2.2: Comparison of Compton backscattering source using quasi-monoenergetic electrons from bubble accelerators and broadband electrons from SM-LWFA.

Eqs. 2.33 and 2.35, we expect $N_T = 10^7$ and $B_{pk} = 3 \times 10^{22}$ photons s^{-1} mm^{-2} mrad^{-2} (per 0.1% BW), which exceed the brightness in SM-LWFA by four orders of magnitude despite two orders of magnitude higher total photon number. In chapter 5, we will discuss our experimental measurement of CBS x-rays from a bubble-regime accelerator with approximately the above parameters.

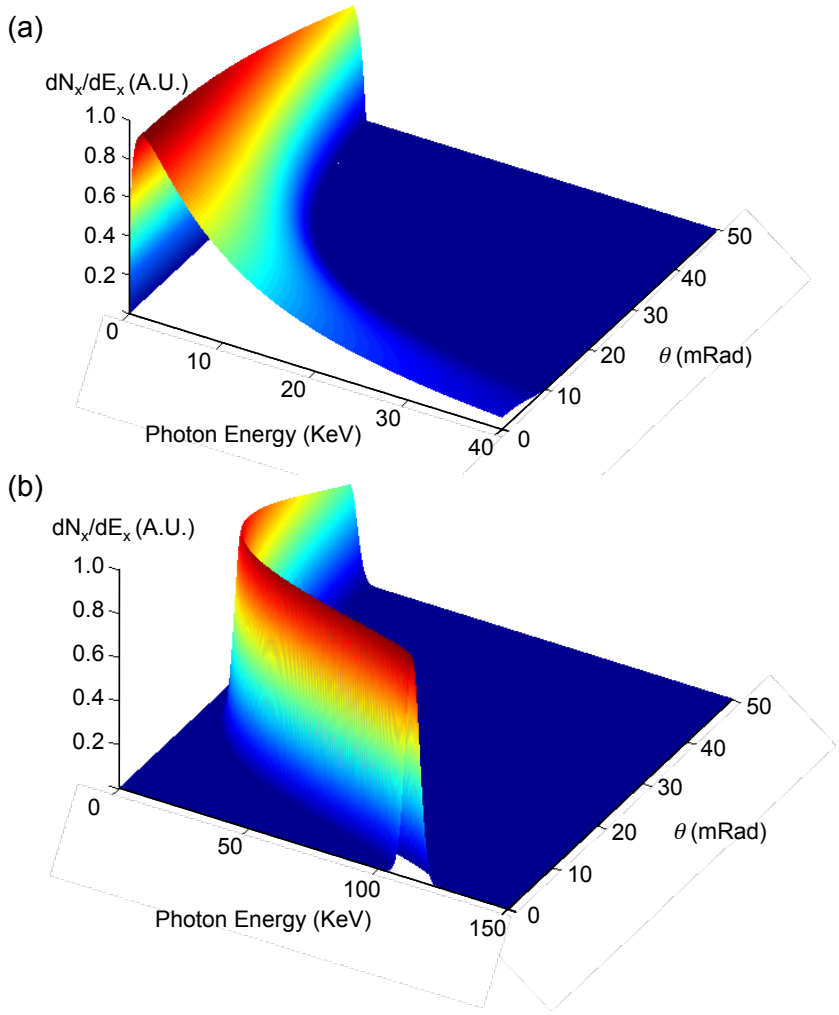

Figure 2.9: Dependence of backscattered spectra on observation angle θ. (a) Angle-resolved backscattered x-ray spectra generated from electrons with an exponential energy distribution ($T_e = 14$ in units of γ) for observation angles in the range $\theta = 0 - 50$ mrad; (b) same for a monoenergetic electron energy distribution peaked at 70 MeV ($\gamma = 136$) and 2% energy spread.

Chapter 3

Global optimization of a tunable, quasi-monoenergetic LPA

Production of bright, coherent, femtosecond hard x-ray pulses by Compton backscatter from compact terawatt-laser-driven wakefield accelerator (LWFA) beams can open a range of ultrafast x-ray science to university laboratories [45], but because of low conversion efficiency and the instability of acceleration in the bubble regime[83] requires careful optimization of charge, energy, energy spread, collimation and repeatability of the electron beam[29]. In this chapter, we discuss global optimization of a terawatt-laser-driven wakefield accelerator by systematically varying laser and target parameters to achieve 100 MeV electrons, 10% energy spread, $\sim$ 100pC charge, 4 mrad divergence and 10 mrad pointing fluctuation with $>$ 90% reproducibility. The central energy of electron beam is tuned from 60 to 100 MeV by varying the plasma density, thereby meeting conditions for producing $\sim 10^7, 80 - 200$keV X-ray photons/pulse by Compton scattering .

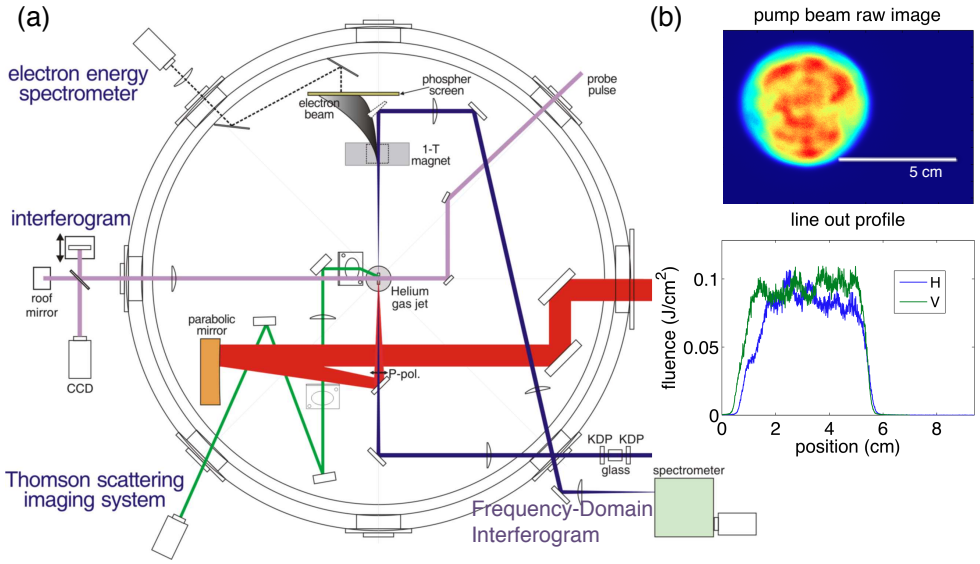

Figure 3.1: (a) Experimental layout. (b) 810 nm pump beam image and lineout profile.

3.1 Experiment setup and laser system

For experiments, 30 TW, 30 fs, 0.8 J, 810nm laser pulses [Fig. 3.1(b)] from the University of Texas Terawatt UT^3 Ti:sapphire system, which operates with 10-Hz repetition rate at central wavelength 800 nm, were focused onto a 1-mm or 3-mm-long supersonic helium gas jet (SmartShell Co., Ltd.) hydrodynamically designed for top-hat density profile with 200 μm sharp edge [Fig. 3.2 (b)]. Fig. 3.1 (a) shows the schematic setup. To drive the LPA, the linearly-polarized laser pulses were focused with f-number 12.5 to Gaussian spot radius $w_0 = 10 \pm 1 \mu$m (intensity profile FWHM $= w_0\sqrt{2\ln 2} = 11.8 \pm 1 \mu$m; the uncertainties indicate rms shot-to-shot fluctuations). The incident beam was carefully optimized to achieve Strehl ratio $> 70\%$and peak intensity $6 \times 10^{18} W/cm^2$

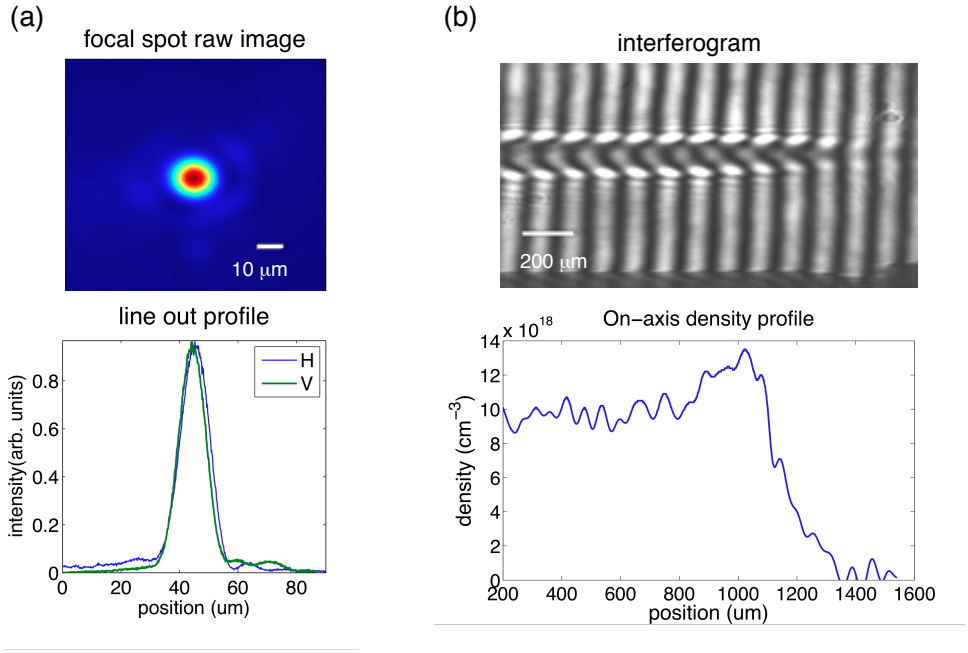

Figure 3.2: (a) Focal spot image and lineout profile. (b) Transverse interferogram taken at gas jet entrance of 1.6-mm field of view and on-axis density lineout profile.

($a_0 \approx 1.6$) at the entrance of the supersonic gas jet (99% helium, 1% nitrogen mixture). A transverse interferometer measured time-averaged plasma density profile $\bar{n}_e(r, z)$ on each shot. A magnetic electron spectrometer, placed downstream from the gas jet, analyzed electron energy on each shot. It consisted of a 1 T magnet that deflected electrons onto a terbium-activated gadolinium oxysulfide (Gd_2O_2S:Tb) phosphor screen (Kasei Optonix model Kyokko PI200), from which, electron-induced fluorescence at 545 nm was imaged onto a 12-bit charge-coupled device (CCD) camera.

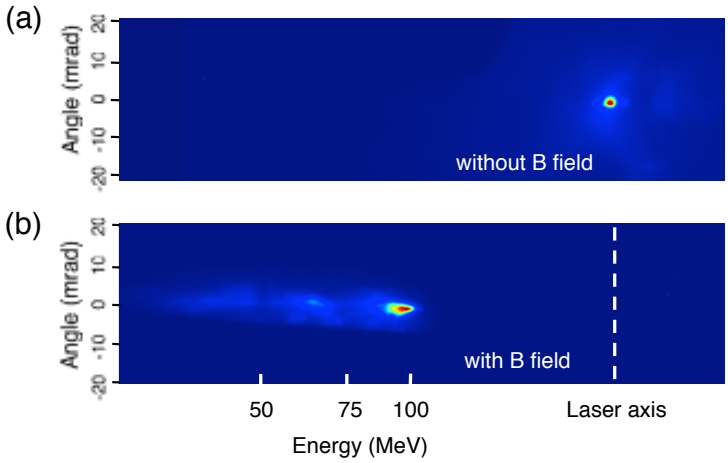

Figure 3.3: Raw images obtained on the LANEX screen. (a) Image of electron beam spatial distribution obtained from the LANEX screen when no magnetic field is applied. (b) Image obtained when magnetic field is applied showing that the electron beam is deviated from laser axis (the white vertical dashed line) and its position corresponds to 100 MeV. (a) and (b) are obtained at an optimum acceleration condition with a plasma density ($n_e = 1.8 \times 10^{19} cm^{-3}$) and a pulse duration of 35 fs (FWHM).

3.2 Global optimization: density, laser focus position, pulse duration, gas jet length, doping nitrogen

Here we demonstrate the generation of high-quality electron beams from a terawatt LWFA with almost 100% shot-to-shot reproducibility, average divergence 4 mrad (FWHM), 10 mrad r.m.s. pointing fluctuation, and average charge $\sim$ 100 pC at $\sim$ 100 MeV. The particular electron beam profile presented in Fig. 3.3(a) has only 2 mrad divergence (FWHM). The electron spectrum in Fig. 3.3(b) has a peak at 95 MeV and $\sim$ 10% energy spread. Both are obtained at an optimum acceleration condition, as discussed below, from a 3-mm He gas jet with $1.8 \times 10^{19}\text{cm}^{-3}$ plasma density and 35 fs drive pulse duration. In

contrast, beams generated from a 1-mm He jet have average peak at 65 MeV with $\sim 90\%$ reproducibility, 10 mrad divergence, at an optimum plasma density of $2.2 \times 10^{19}\mathrm{cm}^{-3}$. Here energy spread was determined by multiplying the vertically-integrated, magnetically-dispersed recorded electron trace dN_e/dx by the magnet dispersion dx/dE to generate an energy distribution dN_e/dE, then taking the ratio of the width E_{FWHM} of the quasi-monoenergetic peak to its central energy E_{peak}. Here N_e is electron number, E electron energy and x horizontal distance along the phosphor screen. The cited energy spread takes into account the low-energy tail of the electron distribution. Charge was determined from integrated fluorescent photon number emitted from the phosphor screen using published calibrations for PI200 [110].

3.2.1 Optimum plasma density

In order to achieve the optimum acceleration, we systematically and extensively investigated how charge, brightness, divergence, pointing, repeatability and energy spectra vary as functions of plasma density, pulse duration and focus position. We varied the plasma density at constant pulse energy (0.8 J on target), pulse duration, and focus position. First of all, the stable and optimum electron beam brightness and divergence were achieved in a narrow range of plasma density ($1.5 - 2 \times 10^{19} cm^{-3}$) for the shortest pulse duration (35 fs) shown in Fig. 3.4. The plasma density was linearly tuned by adjusting gas jet pressure. The averaged on-axis plasma density, n_e, was measured with a transverse interferometer.

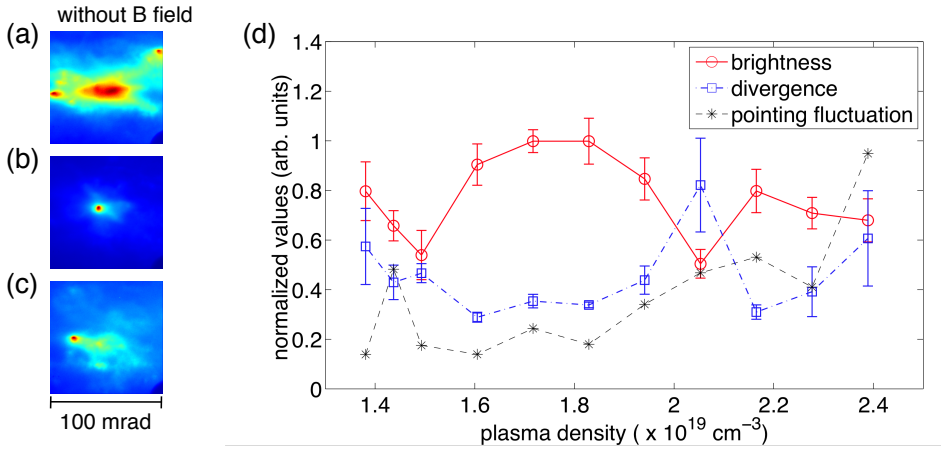

Figure 3.4: (a) - (c) Image obtained on LANEX without applying magnetic field at plasma density of 1.4, 1.8, and 2.4 $\times 10^{19} cm^{-3}$. (d) The normalized brightness, divergence and pointing fluctuation vary as a function of plasma density (pulse duration fixed at 35 fs), where the brightness is evaluated by the peak intensity of the electron profile, the divergence is evaluated by the FWHM of a Gaussian curve fitted to the electron profile, the pointing fluctuation is derived from the standard deviation of the center position of the electron profile imaged on the LANEX screen. Every data point is obtained by averaging over 10-30 shots. Error bars indicate one standard deviation of the 10-30 shots.

In addition, when the electron density was increased from $1.8 \times 10^{19} cm^{-3}$ to $2.4 \times 10^{19} cm^{-3}$, the electron spatial profiles split into several lobes [Fig. 3.4(c)] and the peak electron energy and number decreased [Fig. 3.5(e)]. Below $1.5 \times 10^{19} cm^{-3}$, the divergence and pointing fluctuation of accelerated electrons increased dramatically (Fig. 3.4), although the distribution was still quasi mono-energetic [Fig. 3.5(a)].

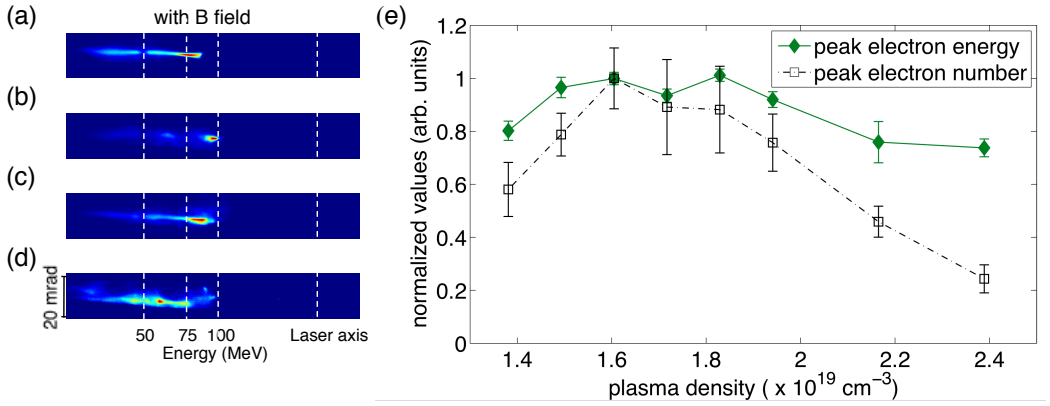

Figure 3.5: (a)-(d) Electron image obtained when magnetic field is applied at plasma density of 1.4, 1.8, 1.9 and 2.2 $\times 10^{19} cm^{-3}$. (e) The normalized peak electron energy and peak electron number vary as a function of plasma density (pulse duration fixed at 35 fs). Peak electron energy is obtained from the peak position of the electron energy distribution as recorded on the LANEX screen with magnetic field applied; peak electron number is obtained by summing up all the electron number along spatial (vertical) axis at peak within a spectral width of 0.3 MeV, which is determined by spectrometer dispersion on a CCD pixel width (0.3 MeV/pixel). Every data point is obtained by averaging over 10-30 shots. Error bars indicate one standard deviation of the 10-30 shots.

3.2.2 Optimum pulse duration

The pulse duration was varied at constant pulse energy by tuning separation of compressor gratings and was measured inside the vacuum chamber by a single-shot auto-correlator located near the target to avoid dispersion from air and optics. We also conducted the experiment at various plasma densities higher and lower than $1.8 \times 10^{19} cm^{-3}$ (optimum density). All the results showed the same trend that stable, optimum electron brightness, divergence, charge and peak energy were achieved with pulse duration shorter than 45 fs (Figs. 3.6 and 3.7). Increasing the pulse duration above 45 fs was

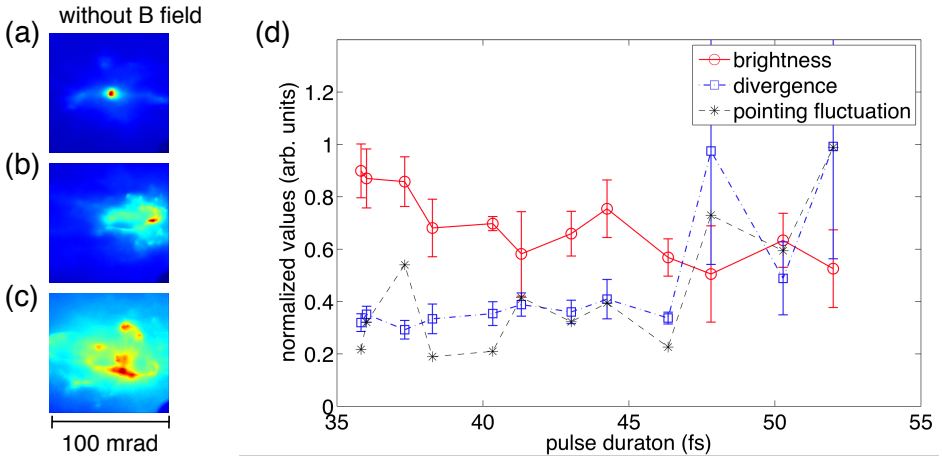

Figure 3.6: (a)-(c) Image obtained on LANEX without applying magnetic field at pulse duration of 35, 41, and 50 fs. (d) The normalized brightness, divergence and pointing fluctuation vary as a function of pulse duration (plasma density fixed at $1.8 \times 10^{19} cm^{-3}$. Brightness, divergence and pointing fluctuations are evaluated as described in the caption of Fig. 3.4.

sufficient to lose repeatability, small divergence and the stable peaked energy distribution. Simulations of previous work [30] also show that the quality of the electron beam is higher when trapped electrons do not interact with laser fields, which increases divergence and energy spread. The argument could explain why higher quality beams are obtained experimentally for shorter pulses and a narrow range of electron density. The evolution of electron brightness, divergence, pointing, and spectra with our experimental parameters also indicates that pulses comparable or shorter than a plasma period are essential for high quality, monoenergetic electron acceleration.

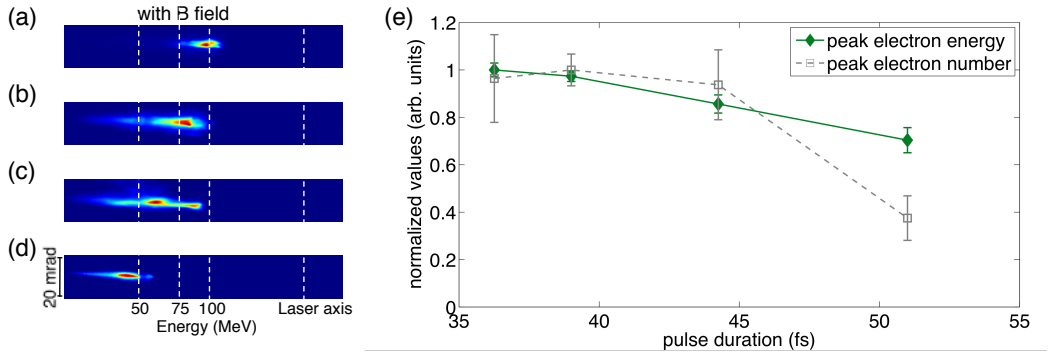

Figure 3.7: (a)-(d) Electron image obtained when magnetic field is applied at pulse duration of 36, 39, 44, and 51 fs. (e) The normalized peak electron energy and peak electron number vary as a function of pulse duration (plasma density fixed at $1.8 \times 10^{19} cm^{-3}$). Peak electron energy and peak electron number are evaluated as described in the caption of Fig. 3.5.

3.2.3 Optimum focus position

We also studied the influence of focus position of the laser pulse with respect to gas jet. Specifically, how the electron brightness, divergence and pointing fluctuation vary as functions of focus position along the laser propagation direction. The result in Figure 3.8 shows that the optimum acceleration happens when the focus is placed close to the front edge of gas jet (0-μm position in Fig. 3.8). The front edge of gas jet is defined as the center of 200-μm up ramp [Fig. 3.2(b)]. The regime of stable acceleration is found to place the focus within $\pm 250\mu$m. When the focus is moved away from the range of $\pm 250\mu$m, the beam loses its pointing stability, small divergence and reproducibility. Technically, we can examine the overlap of the focus position and gas jet edge from the transverse interferogram, which has a spatial resolution

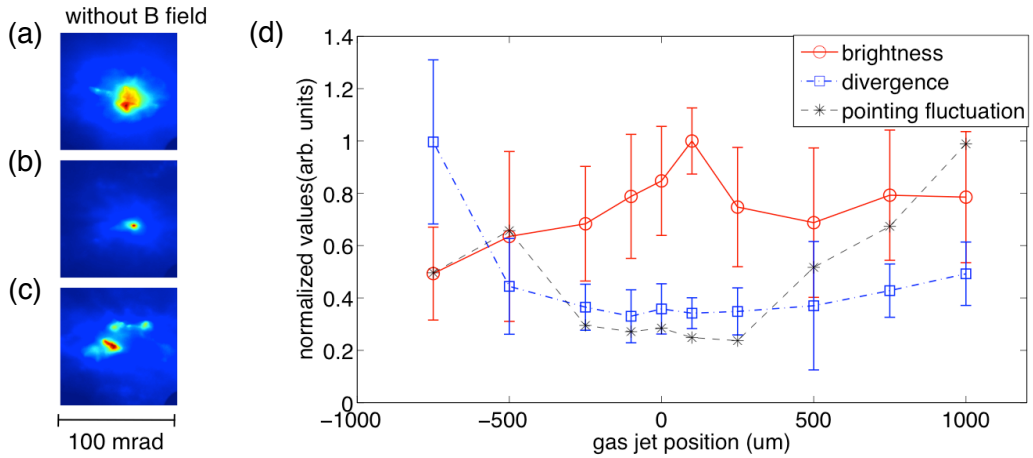

Figure 3.8: (a) - (c) Image obtained on LANEX without applying magnetic field placing focus position at -750 μm, +100 μm, +750 μm with respect to the front edge of gas jet. (d) The normalized brightness, divergence and pointing fluctuation vary as a function of focus position (pulse duration at 35 fs, plasma density at $1.8 \times 10^{19} cm^{-3}$), where brightness, divergence and pointing fluctuations are evaluated as described in the caption of Fig.3.4.

$< 10\mu$m. Although the Rayleigh range of laser focus is $\sim 850\mu$m, the focus center can still be located by lowering the laser intensity such that the ionization channel in interferogram is shorter than 100 μm. The optimum plasma density and pulse duration were all found when focus position was placed at the edge of gas jet.

3.3 Tuning electron energy

The electron beam central energy was tuned from $\sim$ 30 MeV to $\sim$ 110 MeV [Fig. 3.9(b)] of two acceleration length (1mm and 3 mm) by tuning the plasma density from 1.4 to 2.2 $\times 10^{19}$ cm^{-3} in five increments. The yellow high-

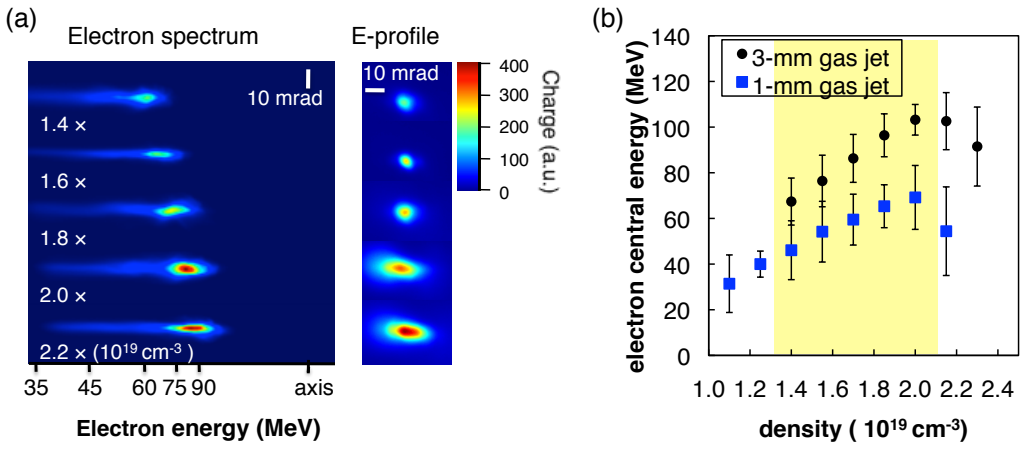

Figure 3.9: (a) Left column: electron spectra observed on PI200 phosphor at five densities 1.4, 1.6, 1.8, 2.0 and 2.2 $\times 10^{19}$cm^{-3}. Right column: electron beam profile recorded 15 cm downstream of gas jet on PI200 phosphor screen with magnet removed at the same five densities. (b) Measured e-beam central energy, plotted vs. density. Each point is the average of 10 shots taken with the same gas jet position and backing pressure.

lighted region in Fig. 3.9(b) represents the range of $\pm 20\%$ optimum density, in which the electron-beams are quasi-monoenergetic. The horizontal error bars represents the 10-shot averaged e-beam energy bandwidth (FWHM). Individual electron-beam spectra [Fig. 3.9(a), left column] and electron-beam profiles [Fig. 3.9(a), right column] from this data set were chosen to best represent the average electron-beam energy and divergence of the set. Electron energy was tuned continuously from $\sim$ 40 to 60 MeV ($\sim$ 60 to 110 MeV) with 1-mm (3-mm) acceleration length while retaining narrow energy and collimation. The choice of 1% nitrogen and 99% helium mixture can provide stable ionization injected electrons at the density lower than optimum condition without

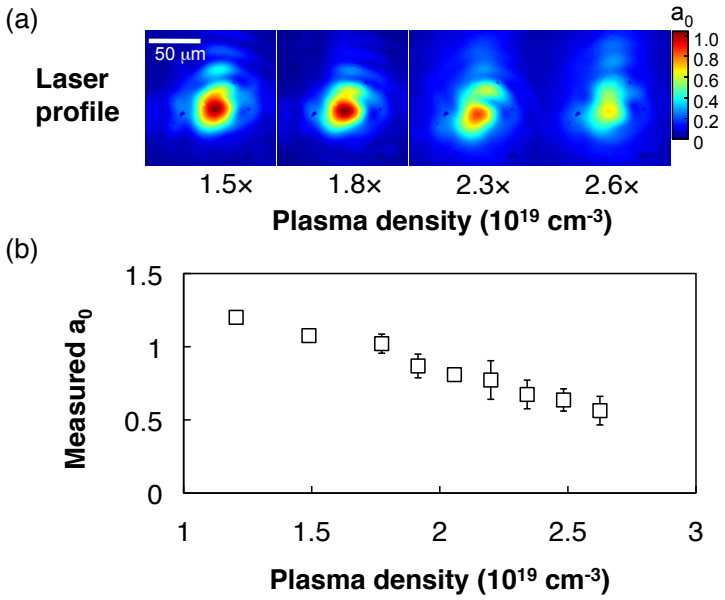

Figure 3.10: (a) Measured laser beam profiles at exit plane of LPA. (b) Measured (black squares) on-axis, time-averaged a_0 of the laser pulse at the gas jet exit as a function of plasma density $\bar{n}_e$.

sacrifice the beam quality.

3.4 Main beam profile after driving LPA

Conversion efficiency from laser pulse to CBS x-rays using PM method depends critically on the intensity profile of the spent drive pulse transmitted through the LPA. We measured transverse laser intensity profile at the 1-mm LPA exit by reflecting the spent drive pulse into an f/10 relay imaging system with a 2-inch diameter pellicle inserted 15 cm downstream of the gas jet. The pellicle left the electron beam unperturbed, so the exit spot profile measurement could be correlated with electron beam properties. The absolute

transmitted intensity was then estimated from the measured profile and transmitted energy, using an estimated pulse duration of 30 fs. We validated this estimate by simulating the transmitted pulse properties for our experimental conditions, will be discussed further in Sec. Discussion, chapter 5.

Fig. 3.10(a) shows images of drive pulse a_0 profiles at the gas jet exit for four $\bar{n}_e$. Although the shapes of these profiles change little with density, peak a_0 decreased about 40% as $\bar{n}_e$ increased from 1.7 to 2.6×10^{19} cm^{-3}. The black squares in Fig. 3.10(b) show how the peak field strength a_0 of the drive pulse at the exit plane of the gas jet varied as a function of $\bar{n}_e$. The absolute a_0 scale was estimated by assuming all measured transmitted pulse energy was contained within the imaged exit profile and that the pulse maintained 30 fs duration. Since the latter are crude approximations, the absolute a_0 scale was further validated through PIC simulations, will be discussed in chapter 5. However, Fig. 3.10(b) represents measured exit-plane axial a_0 without detector averaging, which falls in the range $1.2 > a_0 > 0.9$ (peak intensity $2 > I > 1 \times 10^{18} W/cm^{-3}$) for the n_e range of producing mono-energetic electron-beam.

Chapter 4

PM reflectivity at relativistic regime

Here we present the detailed experimental study of the reflectivity of a plasma mirror (PM) excited at relativistic intensity. Three types of reflectivity measurements are presented: (1) Space and time-integrated reflectivity, measured using energy meters; (2) time-integrated, space-resolved reflectivity, measured by imaging reflected light from the PM surface onto a charge-coupled device (CCD) camera; (3) time- and space-resolved reflectivity, measured by imaging a time-delayed, frequency-doubled, co-propagating probe pulse onto a CCD camera after it reflects from the PM. We describe the experimental setup in Sec. 4.1, and present the experimental results and PIC simulation in Sec. 4.2. Sec. 4.3 presents a discussion and conclusion of the PM performance.

4.1 Experimental setup

Experiments used the 45 Terawatt, Ti: sapphire University of Texas Tabletop Terawatt (UT^3) CPA laser system, which delivers up to 1 J, 810-nm 30-fs FWHM pulses to the target chamber. Fig. 4.1 shows the target chamber setup. The laser beam is split into a main pump beam and a frequency-doubled, low-flux probe beam [Fig.4.1(a)]. The main beam enters the chamber

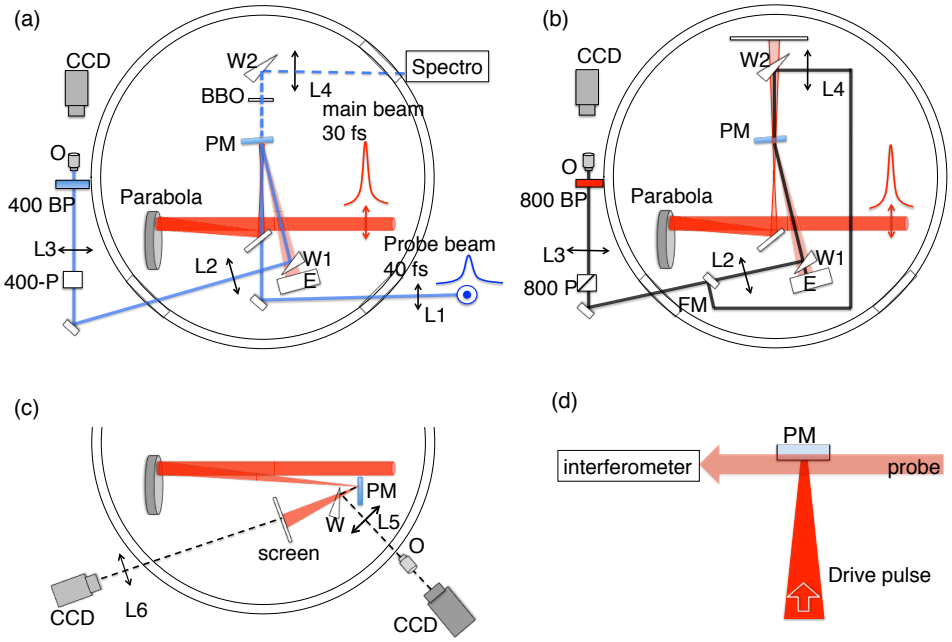

Figure 4.1: The schematic experimental setup. **(a)** Time- and space- resolved measurement. **(b)**Time- integrated, space-resolved reflectivity measurement. **(c)** Relativistic denting effect measurement. **(d)** Transverse interferometer.

with 50-mm-diameter top-hat profile, before it is focused onto the target (PM) with an f/12.5 gold coated parabolic mirror (f = 600 mm). The choice of large f-number (f/12.5, cone angle 4.7 degree) avoids averaging over a large range of angles of incidence. The incident focal spot was optimized to achieve Strehl ratio > 0.5, $w_0 = 10 \pm 1\mu$m (intensity profile $w_{FWHM} = w_0\sqrt{2\ln 2} = 11.8 \pm 1\mu$m; the uncertainties indicate rms shot-to-shot fluctuations), and peak intensity 1.2×10^{19} W/cm^2 ($a_0 \approx 2.1$).

The probe beam, initially of 5-mm diameter, is focused with an f =1000 mm lens to focal spot radius $w_{FWHM} \sim 100\mu$m, which fully overlaps the PM

region. After reflection from the target, a second reflection from a wedge (W1) reduces the probe energy exiting the output window. The part of the probe transmitted through the wedge is collected in a single-shot calorimeter (E). The energy of the incident main pulse was measured with an identical calorimeter. After calibration, the ratio of the reflected and incident energies provides the absolute space- and time-integrated reflectivity. For space- and time-resolved measurements, both reflected probe beam [Fig.4.1(a)] and main beam [Fig.4.1(b)] were imaged (lens L2, L3, and objective lens O) onto a 12-bit CCD camera. The focus position of L2 was adjusted to image the target surface. By switching the band pass filters and polarizers (400/800 BP and 400/800-P), the beam image gives access to a space-resolved reflectivity (800-nm main beam self-reflection) or time- and space-resolved reflectivity (reflected probe beam at various time delays). A second identical set of wedge (W2), lens (L4) and flip mirror [FM, see Fig. 4.1(b)] was inserted to image the original main beam profiles without the PM. The focus of L4 was adjusted such that the images obtained with L2 and L4 could be compared at the same plane, i.e., PM surface, enabling absolute space-resolved reflectivity to be determined [Fig.4.1(b)].

In the probe configuration [Fig.4.1(a)], with PM substrate in place, comparison of images obtained with and without the main beam, at various delays, determined absolute time- and space-resolved reflectivity. Measured, low intensity, reflectivity of the subtract used for the PM is uniformly 5%. Given the magnification of this imaging setup and the CCD pixel size, a pixel

corresponds to 0.6 μm in the object plane. The resolution of the two imaging systems was checked with a reference resolution target to be $\sim 10\mu$m for the main beam and $\sim 5\mu$m for the probe beam. The temporal overlap between the main and probe beams can be, found by observing the spectral interference of the probe beam and the frequency doubled main beam [PM removed, BBO inserted, W2, L4 in Fig. 4.1 (a)]. The bandwidth of the the frequency doubled main beam, 13nm (FWHM), sets the temporal uncertainty, δt (fs) = $533/\delta\lambda$(nm), at least less than 50fs.

For the relativistic denting effect measurement [Fig. 4.1(c)], the main beam was focused right on the surface of a glass slide with peak intensities varying from 10^{16} to 10^{19} W/cm^2. After reflection from the PM target, a second reflection from a wedge (W), 100 mm away from the PM, reduced the energy transmitted through a f=200mm lens (f/5), output window, and an objective lens (L5 and O) onto a 12-bit CCD camera. The focus position of O was adjusted to image the reflected beam profiles at various positions near the target surface. The part of the beam transmitted through the wedge was projected onto a white screen, which was imaged (L6, f = 100mm) onto another 12-bit CCD camera. The beam divergence (or effective f-number) was obtained by dividing the distance from the screen to the PM by the beam diameter, as observed on the white screen. For calibration, the incident main beam was directly projected onto the screen using a flip mirror. The ratio of the integrated images, of the reflected and incident beams, also provided the absolute space- and time- integrated reflectivity.

The transverse interferometer, shown in Fig. 4.1 (d), is used to measure the preplasma density profile in order to determine its scale length (L) on the target surface. Exponential fit to the electron density profile, n_e(x), gives the scale length L, defined by,

$$n_e(x) = N_0 exp(-\frac{x}{L}) \tag{4.1}$$

where N_0 is the maximum measured density, x is the distance from the position of N_0. The laser pulse is focused normally on the target surface by the same f/12.5 parabola to reach peak laser intensity $\sim 1.2 \times 10^{19}$W/cm^2. Contrast measurement shown in 4.6(c)[2], reveals the presence of a prepulse, from about 20ps before the main pulse, at $\sim 10^{15}$W/cm^2 intensity, enough to ignite preplasma expansion. A separate probe beam, of 800nm wavelength and 50fs pulse duration, passes the preplasma parallel to the target surface 1ps before the main pulse reaches the same surface. The interferogram is imaged with a 500μm field of view and $\sim 5\mu$m spatial resolution. The two-dimensional electron density profile of the expanding plasma, in the under dense region of about $5 \times 10^{18} - 5 \times 10^{19}$cm^{-3}, can be resolved from this interferogram. The same interferometer was used to measure the helium plasma density described in chapter 3.

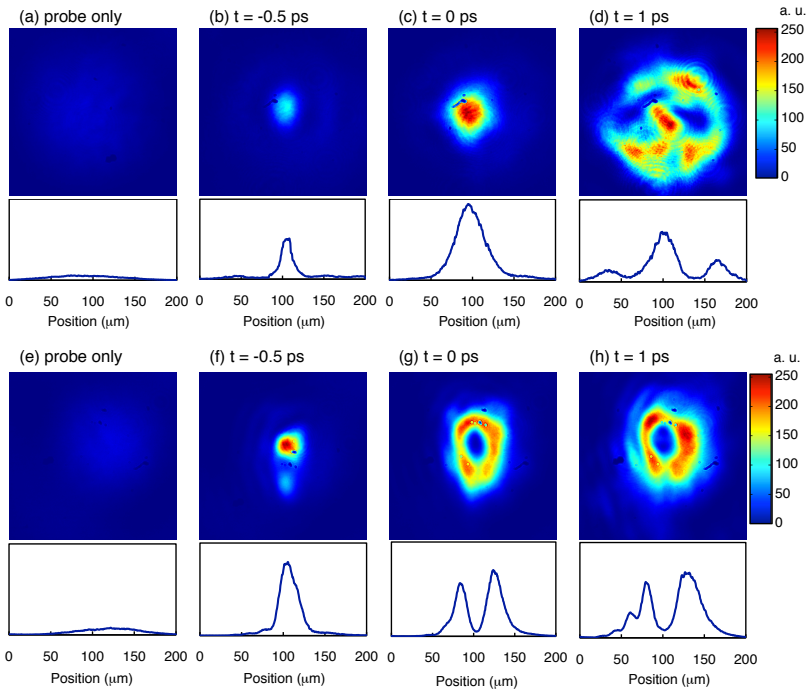

Figure 4.2: The reflected probe beam intensity profiles taken at various time delays with respect to the presence of the main beam (t_0). **(a)** without main beam **(b)** -0.5ps, **(c)** 0ps, **(d)** 1.5ps probe delay with respect to the presence of 10^{17} W/cm^2 main beam. **(e)** without main beam **(f)** -0.5ps, **(g)** 0ps, **(h)** 1.5ps probe delay time with respect to the presence of 5×10^{18} W/cm^2 main beam.

4.2 Results

4.2.1 Temporal dynamics of PM reflectivity measured using the pump/probe technique

Here we present the results of pump/probe measurements of spatial and temporal evolution of the PM reflectivity. The experimental configuration used for these measurements is shown in Fig. 4.1(a). The PM reflectivity was explored over a range of main beam (i.e., pump) intensities from 10^{16}

to 10^{19}W/cm^2, and over probe time delays from -2ps to +4ps relative to the arrival of the main pulse (t_0) on the PM. In Fig. 4.2 , we see two examples of the temporal evolution of the PM reflectivity, at two different main pulse intensities: 10^{17} W/cm^2 for the top row, and 5×10^{18} W/cm^2 for the bottom row. The reflectivity of the PM rises early, and is clearly visible already at -0.5ps relative to t_0, for both cases. There are, however, clear differences in the observed behavior at the two main pulse intensities. For the low intensity, the reflectivity rises gradually; initially it is confined to a region of 10microns - an imprint of the main pulse profile - with reflectivity of 50%; this region grows to 50microns at 0 ps delay, with reflectivity rising to 70%; and finally, at 1ps delay, the reflective region grows to the size of the probe (100 microns) with clear distortions produced by the uneven expansion of the the plasma. In contrast, at high main pulse intensity, the reflectivity increases more rapidly; the reflective region is larger in size initially, at 20microns in diameter, and with 80% central reflectivity at -0.5 ps; at 0ps, the reflective region expands, however a hole appears in the center, forming a reflective ring, yet with still high reflectivity of 70%. The low central reflectivity persists beyond the 1ps delay.

Fig. 4.3 shows the time-resolved center reflectivity trace for different incidence intensities. The probe beam, which had a temporal width of 50 fs (FWHM), was scanned from -1 ps to 2 ps. All the results are for a p-polarized incident beam, with an incidence angle of $\sim$ 4degree. For main beam intensities lower than 10^{18}W/cm^2 [Fig. 4.3 (a)], the reflectivity curve

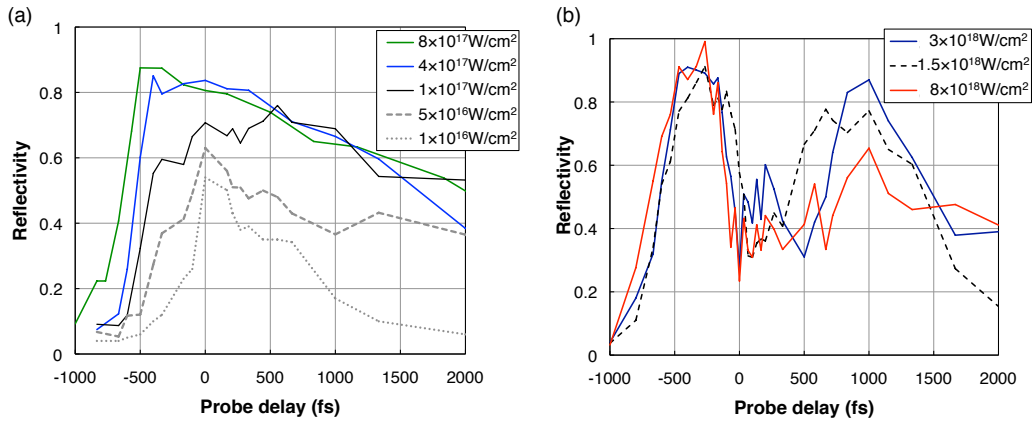

Figure 4.3: Temporal profile of reflectivity probed by a frequency doubled, low fluence, 50-fs pulse at various delay time, after reflection on a PM of glass substrate plate target, for different incident intensities. (a) The incident beam peak intensities are from 10^{16} to 8×10^{17} W/cm^2. (b) The incident beam peak intensities are above 10^{18} W/cm^2

starts to rise to maximum in the range of -0.5ps to 0ps and slowly decays to half of its maximum in 2ps after t_0. When the main beam intensities are increased above 10^{18}W/cm^2 [Fig. 4.3 (b)], the reflective curves show sudden drops near t_0 due to the appearance of reflective holes in the center of profiles shown in Fig. 4.2 (g) and (h). After 1ps delay time, the center reflectivity begins to rise again due to expansion and relaxation. For both spatial and temporal profiles, reflective holes appeared at the region where or when the intensities were higher than 10^{18} W/cm^2. The reason will be explained later in this chapter.

The rise and decay time of reflectivity for mild main beam intensities ($10^{17}-10^{18}$ W/cm^2) are$\sim 1ps$ and $\sim 3ps$ respectively. The triggering of the PM

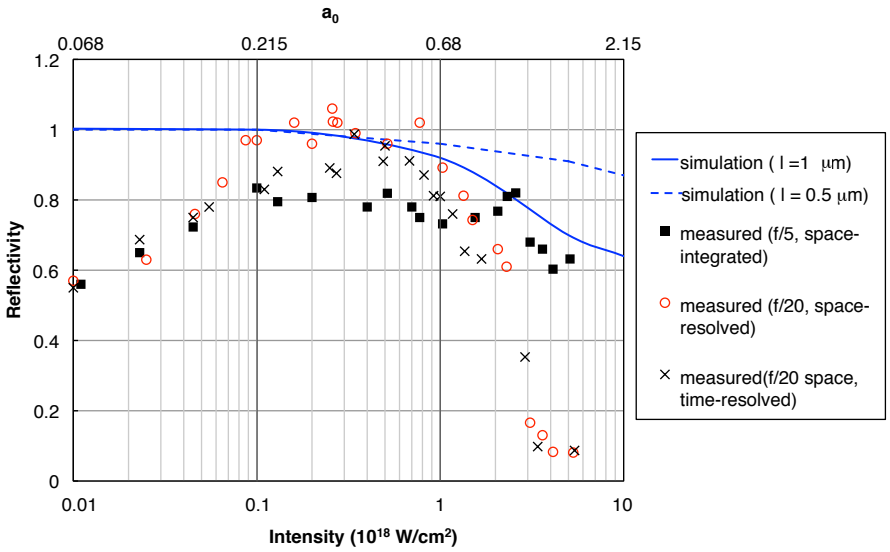

Figure 4.4: Reflectivity of PM vs. intensity. Red circles: measured reflectivity at peak of profile from space-resolved, time-integrated measurement; black cross: measured space- and time-resolved reflectivity; black squares: measured space- and time-integrated reflectivity; blue curves: simulated space- and time-integrated reflectivity, assuming a pre-plasma layer of 1 μm (solid curve) and 0.5 μm (dashed curve).

is observed to start earlier as the intensity increases: the higher the intensity, the earlier the critical intensity is reached. For example, at 10^{18}W/cm^2 , Fig. 4.3 (b), PM triggering is observed at -1ps. This would indicate that the turn-on fluence of a PM at -1ps is 10 J/cm^2 (or several times of 10^{14} W/cm^2) by considering the temporal contrast ratio of the main pulse at -1ps, $10^{-4} - 10^{-3}$[Fig. 4.6(c)]. This measured turn-on fluence agrees very well with the value reported in the previous works [23, 111].

4.2.2 Time-integrated reflectivity of the PM

The time-integrated measurement presents the main pulse self-reflectivity from the PM. Here we demonstrate the results of space-resolved, time-integrated as well as space- and time-integrand reflectivity simultaneously measured with the configuration shown in Fig. 4.1(b). Both results were obtained by taking PM z-scan and energy scan. For the application of Compton backscattering off electron bunch located in a small transverse area (μm scale), the space-resolved, time-integrated measurement can provide the beam-center, local reflectivity. Comparing it to t_0, center reflectivity obtained from space- and time-resolved measurement, the consistency between two can verify our measurement credibility. Meanwhile, the space- and time-integrated measurement presents the reflectivity of total energy as a whole. Fig. 4.4 shows the comparison of three different PM reflectivity measurements and two simulation results varying as a function of main beam peak intencity. In the low intensity regime ($10^{16} - 10^{17}\mathrm{W/cm^2}$), three measurements (red circles: space-resolved, time-integrated; black squares: space-,time-integrated; black crosses: space-, time-resolved) agree well and yield $\sim 60-80\%$ reflectivity. In the mild to relativistic intensity regime ($10^{17} - 10^{19}\mathrm{W/cm^2}$), the space-integrated, wide ($f/5$) cone calorimeter measurements yield $\sim 80\%$ reflectivity for incident intensities from 10^{17} to 2×10^{18} W/cm^2, then drop gradually to $\sim 60\%$ as intensity increases to 5×10^{18} W/cm^2. In contrast, the space-resolved, narrow ($f/20$) cone intensity measurements (black crosses and red circles) yield nearly 100% reflectivity at the peak of the profile for incident intensities from 10^{17} to $\sim 10^{18}$

W/cm^2, then both drop steeply to $< 10\%$ at 5×10^{18} W/cm^2. Evidently the space-integrated measurement yields only 80% reflectivity for $I < 10^{18}$ W/cm^2 because it measures not only the intense center of the focal spot, for which reflectivity is near unity, but the less intense wings, for which reflectivity is only a few percent because overdense plasma is not created. The result is straightforwardly explained if 20% of the pulse energy lies outside the central focus and fails to reach a threshold intensity $\sim 10^{17}$ W/cm^2, which previous work has shown is needed to create a highly reflective overdense plasma [111]. For relativistic intensity, on the other hand, the space-integrated measurement yields much *higher* reflectivity. This discrepancy could be explained either by strong absorption that is localized in the intense center of the pulse profile, or by defocusing of the reflected pulse outside the $f/20$ collection cone due to curvature of the PM surface induced by strong ponderomotive pressure. Below we explore these mechanisms through simulations and further measurement.

4.2.3 Relativistic denting effect on a PM: PIC simulation

To help understand the PM reflectivity results in Fig.4.4, we performed a set of two-dimensional simulations using the multi-dimensional, fully electromagnetic, relativistic PIC code EPOCH[16]. In the simulations, a Gaussian laser pulse with its electric field in the (x, y)-plane, propagated along the x-axis. The beam size was 11 μm (FWHM) with 30 fs pulse duration (FWHM). The simulation box in the (x, y)-plane was 220 μm by 100 μm, with 11000 by 5000 cells, respectively. To simplify the simulation, we assumed a pre-ionized

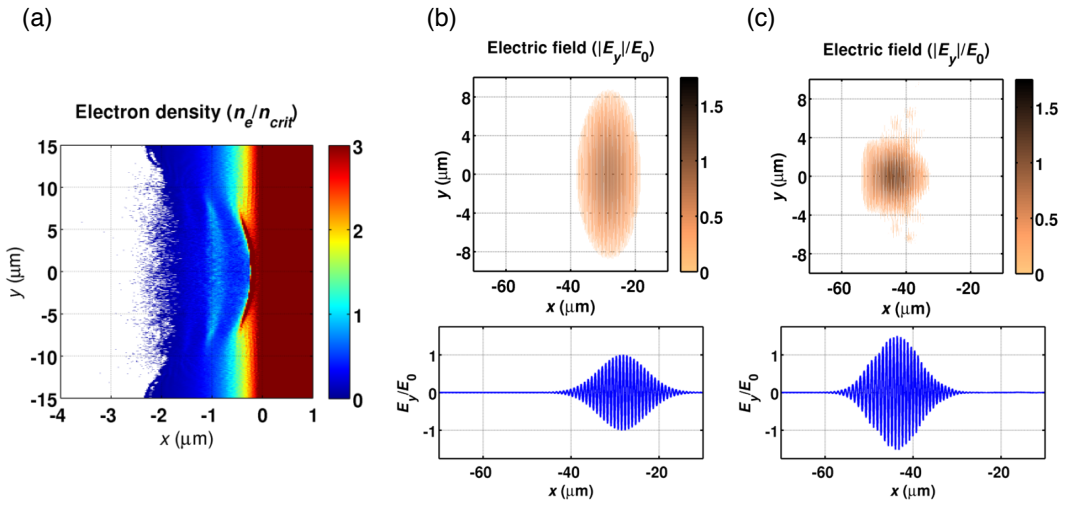

Figure 4.5: Simulations of PM excited at relativistic intensity. **(a)** Simulation: a snapshot of the electron density shortly after the pulse has been reflected. The pulse is less than 20 μm away from the mirror at this point. **(b)**Simulation: a snapshot of the (x, y) and on-axis y-component of the electric field ($|E_y|/E_0$) in the incoming and **(c)** reflected beam at distances less than 50 μm from the plasma surface. The electron density is normalized to the critical density, $n_{crit} \equiv m\omega^2/4\pi e^2$, and the electric field is normalized to $E_0 \equiv a_0 m\omega c/e$. The normalized vector potential in this run is $a_0 = 1.5$ ($I = 5 \times 10^{18}$ W/cm^{-2}).

mirror with its unperturbed surface at $x = x_0$, and electron density for $x > x_0$ set at 50 $n_{\rm crit}$, the ionization levels that would be achieved due to tunneling ionization in a laser field with intensity$> 10^{17}$ W/cm^2. Here $n_{\rm crit}$ is the classical critical density for an electromagnetic wave with $\lambda = 800nm$. A preplasma layer of thickness l at the front surface of the PM was introduced to mimic the interaction of a pre-pulse with the PM. The preplasma electron density profile for $x \leq x_0$ is $n_e = 50 n_{\rm crit} \exp[(x - x_0)/l]$. No additional ionization took place during the PIC simulation.

The blue curves in Fig. 4.4 shows the results of the PIC simulations for

preplasmas with $l = 1.0$ μm (blue solid curve) and $l = 0.5$ μm (blue dashed curve). We calculated reflectivity by taking the ratio of total reflected energy in the laser pulse to the total incoming energy (as in the space-integrated reflectivity measurement). Absorption of laser energy by the PM is the only source of reflectivity decrease in the simulation. For sub-relativistic intensity ($I < 5 \times 10^{17}$ W/cm^2), both simulations yield $\sim 100\%$ reflectivity. Thus the measured 80% spatially-integrated reflectivity must be attributed to 20% of the pulse energy residing in non-Gaussian wings or side lobes that fail to create an overdense plasma. For relativistic intensity, the pulse can transfer energy into longitudinal electron motion in an amount determined by the interaction length (see Ref. [4] for a corresponding discussion and references therein). Thus the reflectivity drops more for preplasma with $l = 1.0\mu$m than for one with $l = 0.5$ μm as I becomes relativistic. The simulation with $l = 1.0$ μm yields $\sim 25\%$ absorption (*i.e.* reflectivity drop) at $I = 5\times10^{18}$ W/cm^2, in good agreement with the spatially-integrated reflectivity measurement. This curve can therefore be used to represent our PM reflectivity for further modeling, as discussed below. However, no reasonable simulation parameters reproduce the dramatic reflectivity drop observed with the spatially-resolved measurement. We therefore conclude that its cause is something other than the absorption.

To pinpoint the cause, we examine the simulated PM surface immediately after a pulse with $I = 5 \times 10^{18}$ W/cm^2 has reflected from it. Fig. 4.5(a) shows a snapshot of the electron density when the reflected pulse is less than 20 μm away from the mirror. Transverse light pressure variation in the incoming

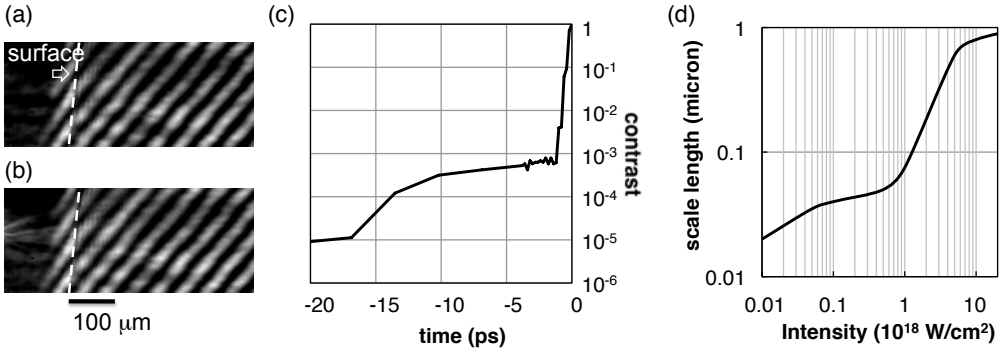

Figure 4.6: (a) Interferogram: main beam was off. (b) Interferogram: 1ps before the main pulse of 6×10^{18} W/cm^2 reaches the target surface. (c) Laser contrast was measured by a third order autocorrelator. (d) The preplasma scale length varied as a function of intensity calculated using laser contrast and ion sound speed $C_s \simeq 50\mu$m/ns [2].

beam produced a concave plasma surface with $\sim 40\mu$m radius of curvature. This curved plasma mirror focuses the reflected pulse in the near-field region, as confirmed by its widened transverse k-spectrum. Thus in the far field, the reflected pulse can diverge outside of the aperture of narrow collecting optics. We therefore attribute the dramatic drop in the narrow ($f/20$) cone reflectivity results to the relativistically curved PM surface rather than absorption. The space-integrated reflectivity measured with larger collecting angle agrees reasonably well with simulation of $l = 1\mu$m with above 60% reflectivity for the intensity of 5×10^{18} W/cm^2.

4.2.4 Relativistic denting effect on a PM: measurement

In the simulation, the absorption and surface denting both depend on the preplasma scale length, which were preset as various values ranging from 0.05 to 5 μm. Since it is an important parameter to be determined, we experimentally measured the scale length by performing transverse interferogram described in Sec. 4.1. The interferogram results shown in Fig. 4.6(b) represents the interference pattern 1ps before main beam of 6×10^{18} W/cm^2 intensity reaching the target surface (dashed line). Comparing to the background pattern [Fig. 4.6(a)], we could barely resolve any density phase shift near the surface. This result implies the preplasma, if formed, should have a scale length $< 5\mu$m, which is the spatial resolution of the interferogram. Although the scale length was not directly measured by interferogram, we can still estimate its value by considering isothermal expansion of an ideal plasma. The speed at which the plasma expands is given by

$$C_s = \sqrt{\frac{ZT_e}{Am_p}} \tag{4.2}$$

where Z is the ion charge state, T_e is electron temperature, A is mass number and m_p is proton mass. In the case of fully ionization, as far as Z/A is concerned, its value is ~ 0.5. However, only low atomic number atoms may be fully ionized. Therefore, Z/A is decreased with the atomic number of target material. In the previous work[2], the measured C_s of carbon material hit by a 10^{15}-W/cm^2 prepulse was 50μm/ns. The C_s of silicon dioxide may be $< 50\mu$ m/ns due to its higher atomic number. The preplasma scale length

can be estimated by L = C_st, where t is the time elapse from the instance the pre pulse of intensity 10^{15}W/cm^2 hits the target to the arrival of main pulse. Thus, by taking account of the temporal contrast information [Fig. 4.6(c)] and C_s($\sim$ 50μm/ns), the scale length seen by main beam intensities varying from 10^{16} to 10^{19} W/cm^2 is estimated, as shown in Fig. 4.6(d), in the range 0.01 and 1 μm, which fall into the range of our simulation assumptions.

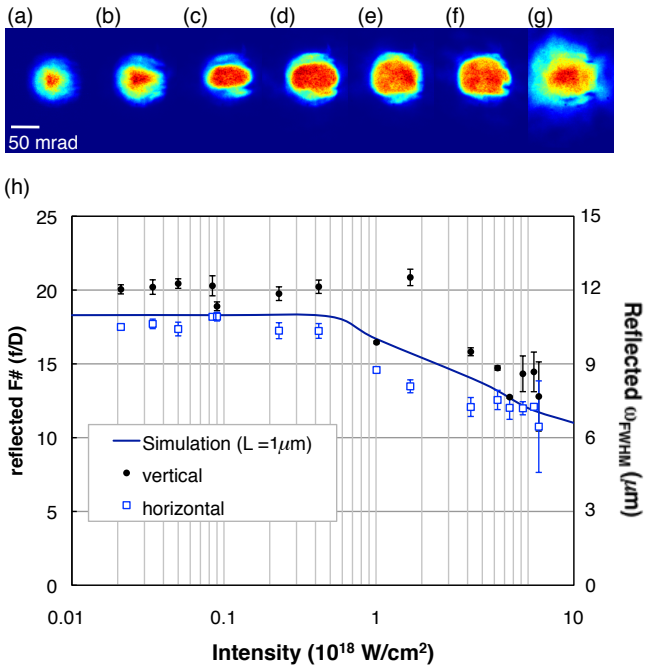

Figure 4.7: The full far-field spatial profiles of the reflected beam corresponding to peak intensities of (a) 8.4×10^{16} (b) 9.0×10^{17} (c)1.7×10^{18} (d) 4.0×10^{18} (e)6.0×10^{18} (f)7.5×10^{18} (g)1.2×10^{19} W/cm^2 on the target surface. (h) shows $F\#$ and its corresponding beam size (ω_{FWHM}) varying as a function of incident beam intensity. Data points are measured from vertical direction(black squares) and horizontal direction(blue squares). The blue solid curve is from simulation result using 1μm scale length. Here $F\#$ = 1/laser divergence and $\omega_{FWHM} = \sqrt{2ln2}(2\lambda F\#/\pi)$.

For revealing the relativistic PM denting effect, we measured the far-field beam divergence and near-field beam focal spot with the configuration shown in Fig. 4.1 (c). The results of far-field divergence measurement are shown in Fig. 4.7. The beam began to be reflected at intensity as low as $10^{15} - 10^{16}$ W/cm^2 with $\sim$ 50mrad divergence ($F\# \sim 20$). The divergence remained constant through out the range of $10^{16} - 10^{18}$ W/cm^2 [Fig.4.7(a), 8.4×10^{16} W/cm^2, and (b), 9.0×10^{17} W/cm^2]. However, the reflected profiles increased in size dramatically once the intensity exceeded 10^{18} W/cm^2 as shown in Fig.4.7(c), 1.7×10^{18} W/cm^2, to (g), 1.2×10^{19} W/cm^2. Fig.4.7 (h) shows the comparison of measured effective $F\#$ on two directions and the simulation result varying as a function of incident intensities. The data points are measured from vertical (black squares) and horizontal (blue squares) direction. The effective $F\#$ is obtained by taking the ratio of the distance between PM and the white screen to the measured beam size ($1/e^2$ intensity). The corresponding transform limited beam size can be estimated by applying the relation $\omega_{FWHM} = \sqrt{2ln2}(2\lambda F\#/\pi)$. Both vertical and horizontal $F\#$ remained constant 20 through out the range of $10^{16} - 10^{18}$ W/cm^2, began dropping once the intensity over 10^{18}W/cm^2 and reached lowest 10 at 10^{19}W/cm^2. The simulation result (blue curve) of 1μm scale length agrees very well with measurement data points. This also confirms the measured scale length $\sim 1\mu$m described earlier in the section. The significant decrease of F# and focused beam size in the range of $10^{18} - 10^{19}$ W/cm^2 indicates relativistic curvature caused beam diverge. In addition, it explains the reason of rapid decrease of

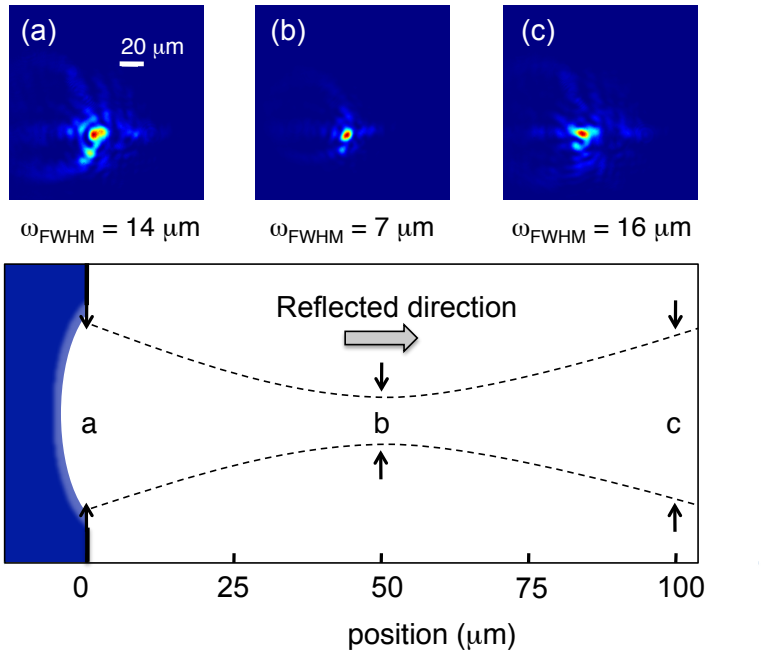

Figure 4.8: Focusing of laser spot by a curved PM in a near-field measurement. The near-field spatial profiles taken at (a) 0, (b)50 and (c)100μm away from surface of PM with main beam intensity of 5×10^{18} W/cm^2. The lower panel shows a spatial map of 100μm near the PM surface. The blue region indicates the area of over dense plasma. a, b, and c indicate the position where the profiles (a), (b) and (c) are taken.

reflectivity in space-resolved measurement using $f/20$ optics.

The near-field measurement using a 5×10^{18} W/cm^2 incident beam focused on PM surface confirmed the refocusing process caused by PM denting surface. By moving the image plane 0, 50 and 100μm away from target surface, the reflected near-field images were found to be refocused from 14μm (FWHM) to 7μm (FWHM) and diverged to 16μm (FWHM) as shown in Fig. 4.8 (a),(b), and(c). The measurement showing the reflected beam focused down to $\sim 7\mu$m

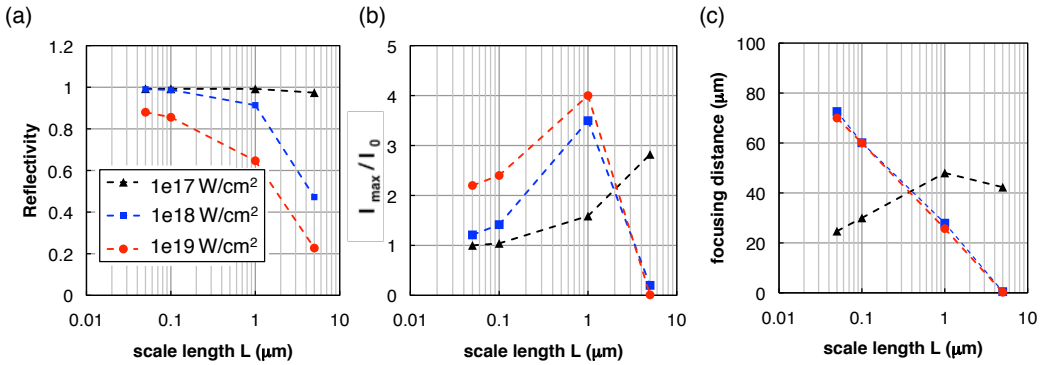

Figure 4.9: Simulation results: (a) The reflectivity (b) The intensity enhancement (c) focusing distance varies as a function of preplasma scale length at 10^{17}, 10^{18} and 10^{19} W/cm^2. The intensity enhancement is determined by the PM curvature is defined by the ratio of initial intensity (I_0) and refocused maximum intensity (I_{max}). focusing distance is the distance from PM to the second focus.

(FWHM) confirmed the far-field divergence measurement at 5×10^{18} W/cm^2. The position where the tightest focus was measured was at $\sim 50\mu$m, which are consistent with our simulation result shown in Fig. 4.5 (c). It can be considered as the focal length of the relativistic PM. In the near-field measurement, the spatial resolution and image depth (twice Rayleigh range) were $\sim 3\mu$m and $\sim 50\mu$m respectively.

4.3 Discussion and conclusion

To help understand the performance of PM especially as a relativistic retro-reflector for Compton scattering purpose, we further investigate the simulation result, especially, the intensity enhancement. It is defined by the ratio of refocused maximum intensity (I_{max}) and initial intensity (I_0). For

example, in one case, a 11μm, 10^{19}W/cm^2 incident beam is 65% reflected by a curved PM (preset with 1μm preplasma scale length) and refocus down to a 4.4μm beam spot, at 25μm away from PM surface. The intensity enhancement (I_{max}/I_0) is a factor of 4. However, the focusing distance, 25 μm, might not be short enough to collide with electron bunch only $\sim$ 10μm following the main pulse. For choosing an optimum condition, we qualitatively plot the simulation results for the reflectivity, intensity enhancement, and focusing distance as a function of preplasma scale length. The results are shown in Fig. 4.9. Apparently, for sub relativistic intensity (10^{17} W/cm^2), the the scale length doesn't alter the reflectivity of PM. However, for relativistic intensity (10^{18} W/cm^2 and 10^{19} W/cm^2), the absorption and enhancement both increase with the scale length. The enhancements for 10^{18} W/cm^2 and 10^{19} W/cm^2 reach peak at 1μm scale length. When scale length increase to 5μm, the reflected beam is seriously filamented and scattered in distribution, which result in very low reflectivity. Fig. 4.9(b) shows the enhancement factor has a optimal condition happening at 1μm scale length for both 10^{18} W/cm^2 and 10^{19} W/cm^2 intensities. We can adjust the 10^{-4} contrast plateau from -50 ps to -1 ps by adjusting the focus position relatively to the position of XPW crystals as well as XPW input energy shown in Fig. 4.10. Through this technique and well characterization of temporal contrast by a third order auto-correlator, we control the 10^{15} W/cm^2 pre pulse at -10ps and achieve the optimal relativistic enhancement on a PM.

In conclusion, we systematically investigated the relativistic PM reflec-

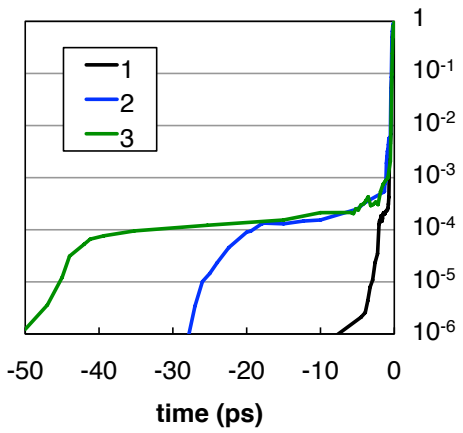

Figure 4.10: Three different temporal contrast profiles achieved by varying the focus position relatively to the position of XPW crystals

tivity with (1) Space and time-integrated; (2) time-integrated, space-resolved; (3) time- and space-resolved measurement as well as EPOCH 2-D PIC simulation. The PM is found to turn on at 10^{15}W/cm^2. The response and decay time for a PM is about 1ps and 3ps for intensity in the range of 10^{18} W/cm^2 and 10^{19} W/cm^2. In the sub-relativistic regime(10^{17} W/cm^2 and 10^{18} W/cm^2), the reflectivity is found to be higher than 90%. In the relativistic regime(10^{18} W/cm^2 and 10^{19} W/cm^2), the divergence of the reflected beam increases outside of the ($f/20$) optics due to relativistic denting effect, although most pulse energy is reflected. Finally, our results show that we control the laser contrast to achieve the optimal condition (1μm scale length) to maximize the denting

enhancement effect (a factor of 4 higher than incident intensity). The measurement result in chapter 3 shows that the spent LPA drive pulse remaining 10^{18} W/cm^2 should be highly reflected by PM. Therefore, the CBS x-ray should be produced by the combination of LPA and PM. The experiment details and result will be discussed in the next chapter.

Chapter 5

Tunable Quasi-monoenergetic CBS X-ray from LPA and PM

5.1 Introduction

CBS x-rays have been generated from LPAs by two methods. In the first, a 100 TW laser system supplied both 1.9 J, 35 fs LPA drive pulses and 0.5 J, 90 fs split-off backscatter pulses. The latter were focused to spot size $w_0 = 22\mu$m, intensity $a_0 \approx 0.3$ onto electrons emerging from the LPA to generate quasi-monoenergetic tunable CBS x-rays up to MeV energy [13, 82]. Under these conditions, stable overlap of backscatter pulse and LPA electrons was achieved despite shot-to-shot pointing fluctuations, as indicated by the high reproducibility ($> 93\%$) and photon number stability (60%) of the CBS x-rays [13, 82]. In the second method, a 30 TW laser system directly supplied only $\sim$ 1 J, 35 fs LPA drive pulses. A plasma mirror (PM) then retro-reflected the drive pulse into the trailing relativistic electrons after the LPA [98]. This method is self-aligning, and thus eliminates sensitivity to laser pointing fluctuations even for very small spot sizes. It is thus a potentially attractive LPA-based Compton x-ray source for laboratories with smaller (tens of TW) laser systems. However, *tunable*, *quasi-monoenergetic* x-rays have not yet been demonstrated by this method, only broadband x-rays centered at

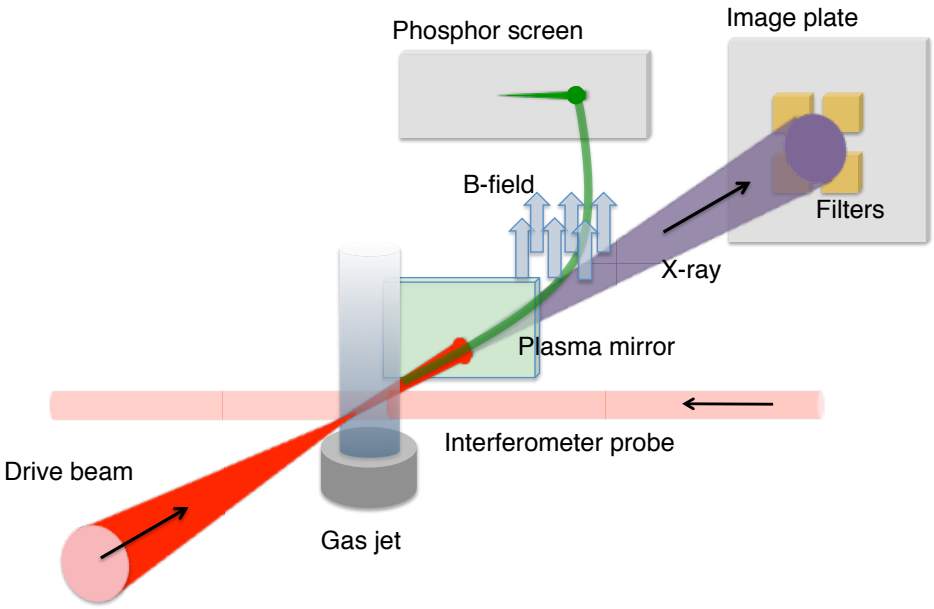

Figure 5.1: Schematic experimental setup for Compton backscatter (CBS). Interaction of a drive laser (red) with a plasma created within the plume of a gas jet accelerates electrons (green), which a magnetic field deflects onto a phosphor screen. The laser pulse ionizes a thin plastic foil placed at the exit of the plasma accelerator, forming a plasma mirror (PM). The retro-reflected drive laser pulse backscatters from the electron beam after the accelerator, creating an x-ray beam (purple) that an imaging plate records after the x-rays pass through a filter pack.

$\sim$ 50 KeV [98]. Moreover, key parameters that determine x-ray brightness, such as the intensity and spatial profile of the laser pulse after driving the LPA and reflecting from the PM, have not been measured, let alone optimized.

5.2 Experimental Procedure

Experiments utilized the 30-TW UT^3 laser system at the University of Texas at Austin, which operates with 10-Hz repetition rate at central wavelength 800 nm (photon energy $E_L = 1.5$ eV). Fig. 5.1 shows the schematic setup. To drive the LPA, 30 fs, 0.8 J linearly-polarized laser pulses were focused with f-number 12.5 to Gaussian spot radius $w_0 = 10 \pm 1\mu$m (intensity profile FWHM $= w_0\sqrt{2\ln 2} = 11.8 \pm 1\mu$m), where the uncertainties indicate rms shot-to-shot fluctuations, and peak intensity 6×10^{18} W/cm^2 ($a_0 \approx 1.6$) at the entrance of a 1-mm supersonic gas jet (99% helium, 1% nitrogen mixture). A transverse interferometer measured time-averaged plasma density profile $\bar{n}_e(r, z)$ on each shot. A magnetic electron spectrometer placed downstream from the gas jet analyzed electron energy on each shot. It consisted of a 1 T magnet that deflected electrons onto a terbium-activated gadolinium oxysulfide (Gd_2O_2S:Tb) phosphor screen (Kasei Optonix model Kyokko PI200) from which electron-induced fluorescence at 545 nm was imaged onto a 12-bit charge-coupled device (CCD) camera.

The divergence, energy and charge of the electron beam were optimized by controlling $\bar{n}_e$, focal spot longitudinal position and drive pulse duration as presented in chapter 3[102]. Electrons were produced in the ionization-injected [71, 78] bubble regime [83] with peak energy as high as ~ 90 MeV [Fig. 5.2 (a)], with energy spread (FWHM) 10% under optimum conditions, and no larger than 20% for all data presented here, ~ 4 mrad divergence, and integrated charge ~ 150 pC for energies > 30 MeV. Electron energy was tuned continu-

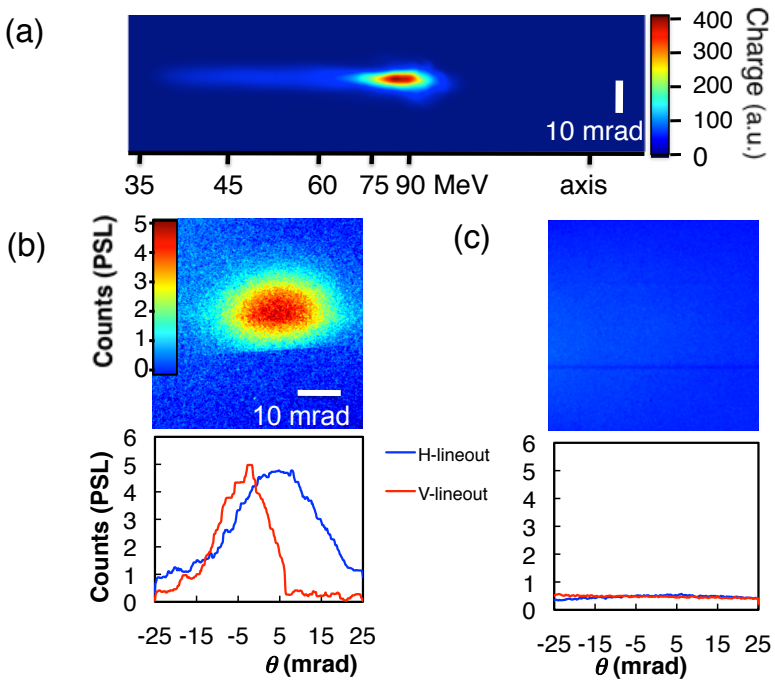

Figure 5.2: **(a)** phosphor screen image of the electron spectrum at plasma density 2.2×10^{19} cm^{-3}, showing peak at 90 MeV. **(b)** and **(c)** x-ray beam profile (top), and horizontal and vertical lineouts (bottom), accumulated over 10 shots with 90μm-thick plastic PM placed either **(b)** at gas jet exit, yielding strong CBS x-rays, or **(c)** 15 mm downstream from gas jet exit, showing no detectable bremsstrahlung background.

ously from $\sim$ 60 to 90 MeV while retaining narrow energy spread and collimation by tuning gas jet backing pressure to vary $\bar{n}_e$ from 1.7 to 2.2×10^{19} cm^{-3}. Conversion efficiency from laser pulse to CBS x-rays depends critically on the intensity profile of the spent drive pulse transmitted through the LPA. We therefore measured transverse laser intensity profile at the LPA exit, with the PM temporarily removed, by reflecting the spent drive pulse into an f/10 relay imaging system with a 2-inch diameter pellicle inserted 15 cm downstream of

the gas jet. The pellicle left the electron beam unperturbed, so the exit spot profile measurement could be correlated with electron beam properties. The absolute transmitted intensity was then estimated from the measured profile and transmitted energy, using an estimated pulse duration of 30 fs. We validated this estimate by simulating the transmitted pulse properties for our experimental conditions, as discussed further in Sec. Discussion.

Conversion efficiency also depends critically on PM reflectivity. PMs are widely used at *sub*-relativistic incident intensities ($a_0 < 1$) to improve the temporal contrast of ultrashort laser pulses that are subsequently focused to ultra-relativistic intensity [23, 36, 50, 111]. Here the intensity incident on the PM is mildly relativistic ($a_0 \geq 1$), a range in which PM reflectivity is not well characterized and can depend sensitively on pulse contrast and intensity. As presented in chapter 4, we measured PM performance at relativistic intensity *without* the gas jet using well-characterized, high-contrast 30 fs pulses incident at 5° from the normal with peak fields in the range $0.2 \leq a_0 \leq 1.6$. Pulses with $a_0 \geq 1$ can depress the PM surface due to their high ponderomotive pressure[24, 106], causing the reflected pulse to focus in front of the PM surface and diverge far from it. This relativistic focusing could potentially increase the intensity that interacts with the trailing electrons, and thereby improve conversion efficiency. We therefore characterized far-field divergence of the time-integrated reflected light using two different collection cones: (*i*) a wide ($f/5$) cone, consisting of an energy calorimeter with 6 cm aperture placed 30 cm from the PM surface; (*ii*) a narrow ($f/20$) cone, in which reflected light

was relay imaged from the PM surface to a CCD camera. Method (i) determined spatially-integrated reflectivity from the ratio of the measured energy to the incident laser pulse energy. Method (ii) determined reflectivity with $\sim 10\mu$m spatial resolution. In this case, reflectivity was determined from the ratio of peak intensity of the reflected beam to the peak incident intensity. For CBS x-ray generation, the PM was inserted $\sim 500\mu$m from the jet exit plane, and reflected the spent pulse at 175 ° to the e-beam direction, to avoid direct retro-reflection into the laser amplifier system. PMs made of 90-μm plastic (household cellophane), 1-mm thick plastic and 1-mm thick fused silica (microscope slide) were tested; all perturbed the transmitted electrons properties only slightly. The PM was translated 500μm transversely after each shot to remove the damaged spot from the path of the next laser pulse, and could be translated longitudinally as far as 2 cm from the jet. Since CBS efficiency fell rapidly to undetectable levels as PM distance from the jet increased, due to expansion of the spent drive pulse, background bremsstrahlung x-rays generated by the highly collimated electrons inside the PM could be characterized at large separations. [Fig. 5.2(c)]

CBS yields x-ray photons of energy $E_X = 4\gamma^2 E_{\mathrm{L}}$, where γ is the electron Lorentz factor. Thus for $E_{\mathrm{L}} = 1.5$ eV, and 90 MeV ($\gamma = 180$) electrons, 185 KeV x-ray photons were expected. A 50 × 50-mm imaging plate (IP, Fujifilm BAS-IP MS 2025 E) placed inside the vacuum chamber 0.8 m from the scattering point detected these photons with high spatial resolution over $\sim$ 60 mrad divergence angle. Because of the low detection efficiency ($\sim$ 0.7

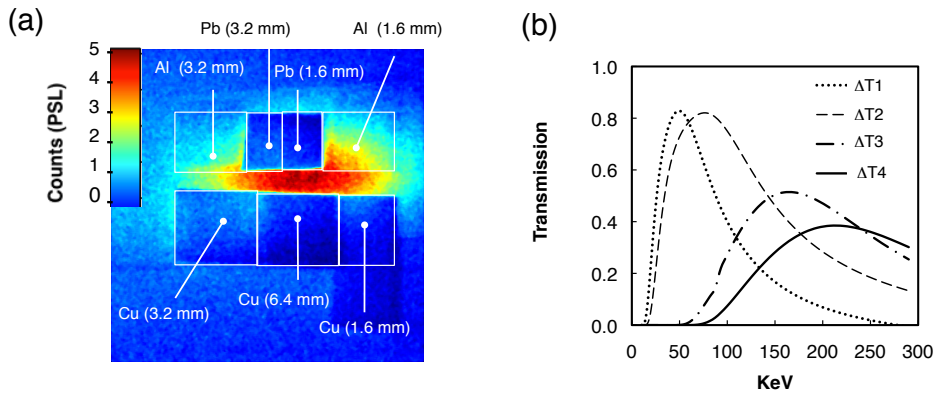

Figure 5.3: CBS x-ray spectra. **(a)** CBS x-ray beam profile accumulated over 10 shots through Al, Cu, and Pb filter combinations. **(b)** Plot of transmission difference (ΔT) spectra of four filter pairs: 1) Al (1.6 mm) and Cu (1.6 mm); 2) Al(3.2 mm) and Cu(3.2 mm); 3) Pb (1.6 mm) and Cu (6.4 mm); 4) Cu (6.4 mm) and Pb (3.2 mm), providing 4 energy bandpass filters peaked at 50, 80, 150 and 200 KeV with FWHM bandwidth of 50, 70, 100, and 120 KeV, respectively.

mPSL/photon [72], where PSL denotes photo-stimulated luminescence), x-ray data was accumulated over ~ 10 shots to achieve adequate signal-to-noise ratio for quantitative analysis. We measured the spatially-averaged x-ray spectrum by comparing transmission through a set of four filter pairs, each composed of different elements, placed symmetrically in horizontal rows immediately (within 5 mrad) above and below the horizontal center line of the x-ray profile [Fig. 5.3(a)], in front of the IP [13, 98]: 1) Al (1.6 mm) and Cu (1.6 mm); 2) Al (3.2 mm) and Cu (3.2 mm); 3) Pb (1.6 mm) and Cu (6.4 mm); 4) Pb (3.2 mm) and Cu (6.4 mm). The differential transmission spectra $\Delta T_i(h\nu_X)$, $i = 1 - 4$) of these filter pairs, plotted in Fig. 5.3(b), provided energy bandpass filters

peaked at 50, 80, 150 and 200 KeV with FWHM bandwidths 50, 70, 100, and 120 KeV, respectively. The transmitted signal through each pair along with IP response curve [72] was used to determine the number of photons with energies within the filter pair's transmission band. To average the spectra spatially, and avoid systematic errors due to inaccuracies or non-uniformities in filter thickness, actuators translated the filter pack horizontally across the beam profile between each of several 10-shot sequences. In addition, data was recorded with filters in different horizontal orders. Within error bars, these variations did not change the extracted spectra. Apart from these filters, the x-ray beam passed through only the 90μm-thick PM and a downstream 20μm-thick Al film (not shown in Fig. 5.1) that deflected laser light transmitted through the PM to a beam dump. These affected the x-ray transmittance and spectrum negligibly. X-ray photon number was obtained by integrating net PSL counts over the x-ray profile recorded on the IP, taking into account the measured x-ray spectrum and the IP response curve [72].

5.3 Experiment Results

5.3.1 CBS x-ray and e-beam properties

Fig. 5.2(b) (upper panel) shows a background-subtracted 10-shot image of the x-ray beam, unobstructed by filters, obtained for the same conditions as the electron spectrum in Fig. 1(b). The x-ray beam diverged $\sim$20 (10) mrad (FWHM) in the horizontal (vertical) direction, as shown in the lower panel of Fig. 5.2(a). Larger horizontal pointing fluctuations of the e-beam ($\sim$ 10 mrad)

were primarily responsible for the asymmetry in the x-ray profile. X-rays were observed for 95% of shots for which the LPA produced quasi-monoenergetic relativistic electrons and the PM was placed at the gas jet exit, although 10-shot averaging was necessary to achieve adequate signal-to-noise ratio to fit a Gaussian curve to the x-ray profile. On most of the 5% of shots that failed to produce x-rays, we observed anomalous large-angle scatter or anomalously low reflectivity from the PM on a nearby detector, suggesting that the transmitted drive pulse struck a local defect on the plastic film. No x-rays were observed in any shots for which the LPA failed to produce relativistic electrons, or the gas jet was turned off. When the PM was moved 15 mm or further away from gas jet, at most a background bremsstrahlung x-ray signal $\sim 10\times$ weaker than the signal shown in Fig. 5.2(b) was observed in conjunction with relativistic electrons. With a 90-μm plastic foil PM, no background bremsstrahlung was detected, as shown in Fig. 5.2(c). All results presented here were obtained with this PM.

Fig. 5.3(a) shows a typical 10-shot-averaged x-ray profile transmitted through the filter pack.

Figs. 5.4(a)-(c) show extracted spatially-averaged x-ray spectra (black dots with error bars) corresponding to the electron spectra shown in the insets. The x-ray spectra are clearly *not* decaying exponentially with increasing photon energy, as in previously reported PM/LPA-based CBS results [98]. Instead spectral intensity rises below, and falls beyond, a peak x-ray energy. The dashed curves in main panels (a)-(c) are CBS spectra calculated from *single-*

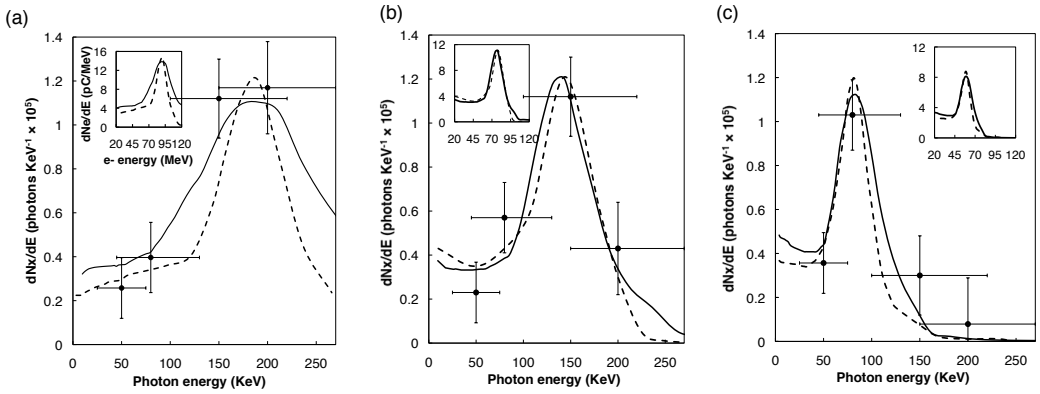

Figure 5.4: **(a)-(c)** CBS x-ray spectra for 3 values of LPA plasma density $\bar{n}_e$ and electron energy E: **(c)** $\bar{n}_e = 2.2 \times 10^{19}$ cm^{-3}, $E = 90$ MeV; **(b)** $\bar{n}_e = 1.8 \times 10^{19}$ cm^{-3}, $E = 75$ MeV; **(c)** $\bar{n}_e = 1.4 \times 10^{19}$ cm^{-3}, $E = 60$ MeV. Data points: mean energy measured in each of the 4 bands. Horizontal error bars: FWHM of each band. Vertical error bars: RMS variation for multiple 10-shot data sets. Solid curves: 10-shot-averaged x-ray spectra calculated from electron spectra for each of 10 shots. Dashed curves: *single-shot* x-ray spectra calculated from single-shot electron spectra. Inset of panel **(a)-(c)**: measured *electron* spectrum at $\bar{n}_e = 2.2, 1.8, and 1.4 \times 10^{19}$ cm^{-3} averaged over 10 shots (solid curve), and single-shot (dashed curve), corresponding to the x-ray spectrum shown in main panel. The axis labels are the same.

shot electron spectra (dashed curves, insets) within the 10-shot sequence that produced each set of x-ray data. The calculated peak energies [(a) 185 keV; (b) 144 keV; (c) 81 keV] agree well with the data points, but the calculated peak widths ($\delta E_X(FWHM)/E_X$) are narrower: (a) 0.44; (b) 0.51; (c) 0.5, respectively. This discrepancy is removed when observed shot-to-shot fluctuations of the electron spectra are taken into account, yielding the 10-shot averaged electron spectra shown by solid curves in the insets of Figs. 5.4(a)-(c). The solid curves in the main panels of Figs. 5.4(a)-(c) show the corresponding cal-

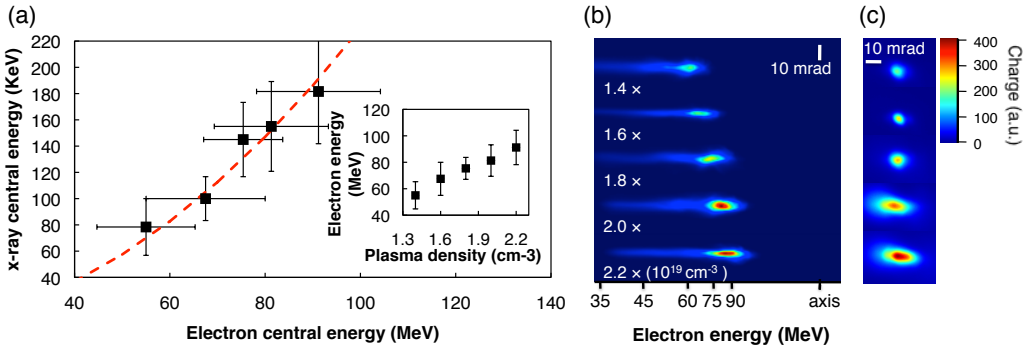

Figure 5.5: **(a)** Measured x-ray central energy, plotted vs. measured electron central energy, compared to $4\gamma^2$ scaling (red dashed line). Inset: electron energy vs. plasma density of a 1-mm gas jet. Each point is the average of 10 shots taken with the same gas-jet position and backing pressure. Error bars represent FWHM of 10-shot averaged e-beam bandwidth. **(b)** Electron spectra observed on PI200 phosphor at five plasma densities: 1.4, 1.6, 1.8, 2.0, and 2.2 $\times 10^{19} cm^{-3}$. **(c)** Electron beam profiles recorded 15 cm downstream of gas jet on PI200 phosphor screen with magnet removed, at the same five densities.

culated 10-shot averaged x-ray spectra, which agree very well with the data, and are somewhat broader: (a) 0.63; (b) 0.56; (c) 0.66. The good agreement with the 10-shot averaged x-ray data points validates the extracted *single-shot* FWHM, which averages 0.5 over our tuning range.

The central x-ray energy E_X was tuned from ∼75 to ∼200 KeV [Fig. 5.5(a), main panel] by tuning the central energy of quasi-monoenergetic LPA electrons from 60 MeV ($\gamma = 120$) to 90 MeV ($\gamma = 180$) [Fig. 5.5(b)] by tuning plasma density from 1.4 to 2.2×10^{19} cm^{-3} in five increments [Fig. 5.5(a), inset]. The horizontal (vertical) error bars in the main panel (inset) of Fig. 5.5(a) represent the 10-shot-averaged e-beam energy bandwidth (FWHM). The vertical error

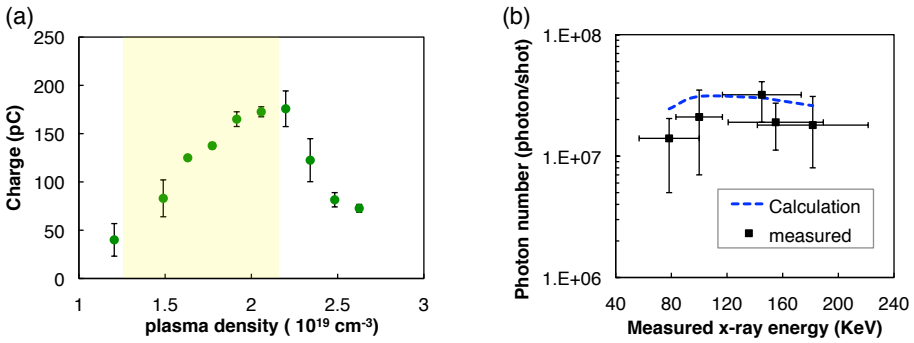

Figure 5.6: **(a)** Measured electron charge from the LPA (green data points) as a function of plasma density $\bar{n}_e$. Shaded yellow region denotes $\bar{n}_e$ range over which the LPA produces quasi-monoenergetic, central-energy-tunable electrons. **(b)** Measured (black dots) and calculated (blue dashed curve) x-ray photon number per shot plotted vs. average central energy of the x-ray beam. Horizontal error bar represents the FWHM of the Gaussian curve fitted to the measured x-ray spectrum. Vertical error bar represents uncertainty caused by fluctuation of background noise relative to the signal.

bars in the main panel of Fig. 5.5(a) represent the corresponding FWHM of the peaked x-ray spectra. The tuned x-ray energy agrees well with the theoretical scaling $E_X = 4\gamma^2 E_L$, shown by the dashed red curve in Fig. 5.5(a).

Fig. 5.6(a) shows the total electron charge (green data points) from the LPA as a function of $\bar{n}_e$. The yellow shaded region denotes the $\bar{n}_e$ range over which the LPA produced quasi-monoenergetic electrons, in which charge varied from 90 to 160 pC. Fig. 5.6(b) shows the x-ray photon number per shot (data points with error bars) plotted as a function of central x-ray photon energy, obtained over the same $\bar{n}_e$ range. Photon number was stable to within 50% of its average value 2×10^7 throughout the tuning range. The blue dashed curve is a calculated photon number, discussed in Sec. Discussion.

5.3.2 Laser intensity after LPA and PM

Fig. 5.7(a) shows images of drive pulse a_0 profiles at the gas jet exit for four $\bar{n}_e$. Although the shapes of these profiles change little with density, peak a_0 decreased about 40% as $\bar{n}_e$ increased from 1.7 to 2.6×10^{19} cm^{-3}. The red squares in Figure 5(b) show how the peak field strength a_0 of the drive pulse at the exit plane of the gas jet varied as a function of $\bar{n}_e$. The absolute a_0 scale was estimated by assuming all measured transmitted pulse energy was contained within the imaged exit profile and that the pulse maintained 30 fs duration. Since the latter are crude approximations, the absolute a_0 scale was further validated through PIC simulations, as discussed in Sec. Discussion.

Fig. 5.7 (c) shows results of PM reflectivity measurements. The spatially-integrated, wide ($f/5$) cone calorimeter measurements (black squares) yielded $\sim 80\%$ reflectivity for incident intensities from 10^{17} to 2×10^{18} W/cm^2, then dropped gradually to $\sim 60\%$ as intensity increased to 5×10^{18} W/cm^2. In contrast, the spatially-resolved, narrow ($f/20$) cone intensity measurements (red triangles) yielded nearly 100% reflectivity at the peak of the profile for incident intensities from 10^{17} to $\sim 10^{18}$ W/cm^2, then dropped steeply to $< 10\%$ at 5×10^{18} W/cm^2. Evidently the spatially-integrated measurement yields only 80% reflectivity for $I < 10^{18}$ W/cm^2 because it measures not only the intense center of the focal spot, for which reflectivity is near unity, but the less intense wings, for which reflectivity is only a few percent because overdense plasma is not created. The result is straightforwardly explained if 20% of the pulse energy lies outside the central focus and fails to reach a threshold intensity

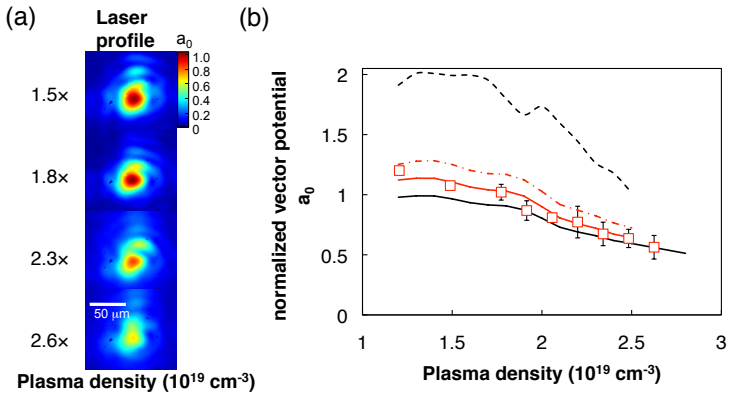

Figure 5.7: **(a)** Measured laser beam profiles at exit plane of LPA, from which measured a_0 values in panel (b) were derived. **(b)** Measured (red squares) and simulated (curves) on-axis, time-averaged a_0 of the laser pulse at the gas jet exit as a function of plasma density $\bar{n}_e$. Black dashed curve: simulated a_0 assuming a sharply bounded plasma exit profile, with no density down-ramp. Red dot-dashed curve: simulated a_0 assuming a 200 μm down-ramp similar to the measured $\bar{n}_e(z)$ exit profile. Red solid curve: a_0 obtained by averaging the calculated a_0 profiles of the previous simulation over a transverse area of 6 μm diameter, to mimic spatial resolution of the detector. Black solid curve: calculated a_0 of the scattering pulse after reflecting from PM, obtained by multiplying a_0 from red dot-dashed curve by PM reflectivity (Fig.5.9, solid blue curve).

$\sim 10^{17}$ W/cm^2, which previous work has shown is needed to create a highly reflective overdense plasma [111]. For relativistic intensity, on the other hand, the spatially-integrated measurement yields much *higher* reflectivity. This discrepancy could be explained by defocusing of the reflected pulse outside the $f/20$ collection cone due to curvature of the PM surface induced by strong ponderomotive pressure as described in chapter 4 (Sec. 4.2.3).

The top row of Fig. 5.5(c) shows $\bar{n}_e$-dependent profiles of electrons recorded on a PI200 screen 35 cm downstream from the LPA with the magnet

removed. Throughout the range $1.4 < \bar{n}_e < 2.2 \times 10^{19}$ cm^{-3} in which the LPA produced quasi-monoenergetic electrons, the electron beam diverges less than 10 mrad, and thus expands negligibly within the 500μm distance between gas jet exit and PM. Since the electron beam exits the LPA typically with only a few microns diameter [13], it is much narrower than the FWHM of the transmitted drive pulse at the point of backscatter, and can be assumed to interact with its peak intensity. For $\bar{n}_e > 2.2 \times 10^{19}$ cm^{-3}, the electron beam divergence increases rapidly to > 20 mrad (not shown).

5.4 Discussion

To help understand and calibrate the exit-plane intensity results in Fig. 5.7 (b), we used the 3D particle-in-cell (PIC) code Virtual Laser Plasma Lab (VLPL) [84] to simulate a 30 fs (FWHM) Gaussian pulse with spot size 11μm (FWHM) and peak intensity 5×10^{18} W/cm^2 propagating into a 200 μm density up-ramp followed by an 800 μm plateau of constant $\bar{n}_e$. For $1.4 < \bar{n}_e < 2.2 \times 10^{19}$ cm^{-3}, the simulated laser pulse self-focused, and formed a plasma bubble that trapped ionization-injected electrons before accelerating them to 60 to 90 MeV, in good agreement with the electron energy measurements in Fig. 5.5(b). Elsewhere we have shown for similar conditions that the VLPL results agree well with bubble dynamics measured with an all-optical streak camera and with electron energy measurements [65]. Here we are concerned with laser intensity transmitted through the LPA. The black dashed curve in Fig. 5.7(b) shows simulated time-averaged on-axis a_0 at the jet exit as a

function of $\bar{n}_e$, for an artificially sharply-bounded jet exit with no density down-ramp. The shape of the curve resembles the data (red squares), but is roughly 2× higher than the crudely estimated absolute a_0 values of the data points. The red dot-dashed curve shows the simulated on-axis exit-plane intensity when a realistic 200 μm density down-ramp, matching the profile observed in the transverse interferometer, was added after the 800 μm plateau. The intensity is now lower because the exiting pulse expands in the down-ramp. The red solid curve shows the result of locally averaging the exit-plane intensity profile within a transverse area of 6 μm diameter, to mimic the spatial resolution of the relay imaging system. This spatial resolution was calibrated directly by imaging a resolution test chart (1951 USAF) placed at the exit plane of the LPA. The result agrees almost perfectly with the data points. Thus the crude procedure described earlier for estimating absolute a_0 values at the jet exit fortuitously agrees with 3D PIC simulations, which also corroborate the observed $\bar{n}_e$-dependence. Most likely the assumption that the central imaged laser profiles [shown in Fig. 5.7(a)] contained *all* of the transmitted pulse energy overestimated the actual energy in this profile, while the assumed 30 fs pulse duration overestimated the actual duration by neglecting front end erosion by the laser-plasma interaction. These two errors evidently canceled, yielding agreement. The dot-dashed red curve in Fig. 5.7(b) thus accurately represents exit-plane axial a_0 without detector averaging, which falls in the range $1.2 > a_0 > 0.9$ (peak intensity $2 > I > 1 \times 10^{18}$ W/cm^2) for the $\bar{n}_e$ range of interest.

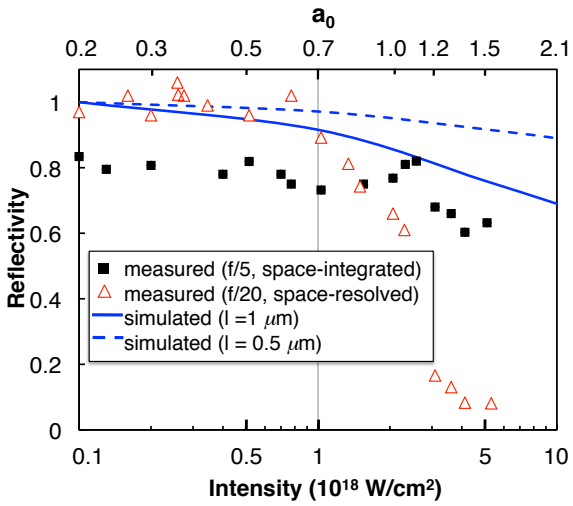

Figure 5.8: Reflectivity of PM vs. intensity. Red triangles: measured reflectivity at peak of laser profile; black squares: measured space- and time-integrated reflectivities, measured by energy meter; blue curves: simulated space- and time- integrated reflectivity, assuming a preformed plasma layer of density scale length of 1μm (solid) and 0.5 μm (dashed).

To help understand the PM reflectivity results in Fig. 5.8, we performed a set of two-dimensional simulations using the multi-dimensional, fully electromagnetic, relativistic PIC code EPOCH[16] as described in chapter 4 (Sec. 4.2.3). The blue curves in Fig. 5.8shows the results of the PIC simulations for preplasmas with $l = 1.0$ μm (blue solid curve) and $l = 0.5$ μm (blue dashed curve). We calculated reflectivity by taking the ratio of total reflected energy in the laser pulse to the total incoming energy (as in the space-integrated reflectivity measurement). Absorption of laser energy by the PM is the only source of reflectivity decrease in the simulation. For sub-relativistic intensity ($I \leq 5 \times 10^{17}$ W/cm^2), both simulations yield $\sim 100\%$ reflectivity. Thus the

measured 80% spatially-integrated reflectivity must be attributed to 20% of the pulse energy residing in non-Gaussian wings or side lobes that fail to create an overdense plasma. For relativistic intensity, the pulse can transfer energy into longitudinal electron motion in an amount determined by the interaction length (see Ref. [4] for a corresponding discussion and references therein). Thus the reflectivity drops more for preplasma with $l = 1.0\mu$m than for one with $l = 0.5$ μm as I becomes relativistic. The simulation with $l = 1.0$ μm yields $\sim 25\%$ absorption (*i.e.* reflectivity drop) at $I = 5\times10^{18}$ W/cm^2, in good agreement with the spatially-integrated reflectivity measurement. This curve can therefore be used to represent our PM reflectivity for further modeling, as discussed below.

Fig. 5.9(a) shows a snapshot of the PM surface immediately after a pulse with $I = 10^{19}$W/cm^2 being reflected less than 20 μm away from the mirror. Transverse light pressure variation in the incoming beam produced a concave plasma surface with $\sim 25\mu$m radius of curvature. This curved plasma mirror focuses the reflected pulse in the near-field region, as confirmed by its widened transverse k-spectrum. Thus in the far field, the reflected pulse can diverge outside of the aperture of narrow collecting optics. We therefore attribute the dramatic drop in the narrow ($f/20$) cone reflectivity results to the relativistically curved PM surface rather than absorption.

The above analysis, together with measured e-beam charge [Fig. 5.6(a)], enables calculation of x-ray photon number based on theoretical work of Ref. [11]. We take a_0 of the backscattering pulse to be a_0 at the exit of the LPA [red dot-

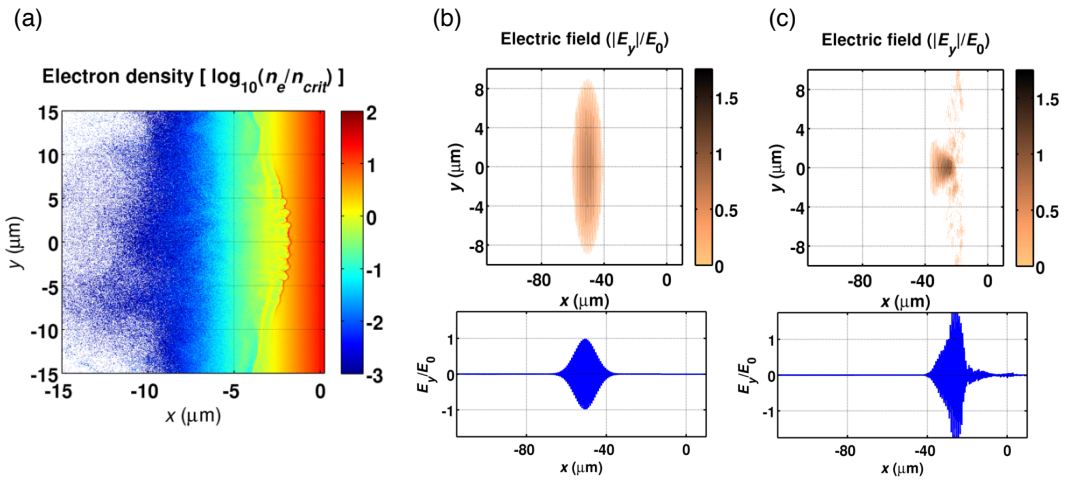

Figure 5.9: Simulations of PM excited at relativistic intensity. **(a)** Simulation: a snapshot of the electron density shortly after the pulse has been reflected. The pulse is less than 20 μm away from the mirror at this point. **(b)**Simulation: a snapshot of the (x, y) and on-axis y-component of the electric field (E_y) in the incoming and **(c)** reflected beam at distances less than 50 μm from the plasma surface. The electron density is normalized to the critical density, $n_{crit} \equiv m\omega^2/4\pi e^2$, and the electric field is normalized to $E_0 \equiv a_0 m\omega c/e$. The normalized vector potential in this run is $a_0 = 2$ ($I = 10^{19}$ W/cm^{-2}).

dashed curve in Fig. 5.7(b)] multiplied by reflectivity of the PM, for which we use the blue solid curve in Fig. 5.7(c). The result, plotted as a function of $\bar{n}_e$, is the black solid curve in Fig. 5.7(a) and ranges from 1.2 to 0.7 within the quasi-monoenergetic tuning range of the e-beam. This corresponds to intensity 4 to 10 times higher than achieved with CBS by a separate counter-propagating laser pulse [82]. The blue dashed line in Fig. 5.6(b) then shows the calculated x-ray photon number vs. central x-ray photon energy. The calculated and measured photon numbers, averaged over x-ray photon energy, are 2.7×10^7 and 2.0×10^7, respectively. The calculated values are within the the error bars

of the measured values, and confirm the weak dependence of photon number on photon energy. This good agreement confirms the analysis of exit driver intensity and PM reflectivity, and shows that the automatic overlap between e-beam and the peak of the reflected scattering pulse is very high.

X-ray brightness can be estimated from the measured beam divergence and photon number distribution, assuming a 6 μm source size [13] and 30 fs x-ray pulse. The result is 10^{19}photons s^{-1} mm^{-2} mrad^{-2} (per 0.1% bandwidth) for 190 KeV x-rays. Energy conversion efficiency from laser pulse to X-ray beam is $\sim 10^{-6}$, while photon conversion efficiency is $\sim 6 \times 10^{-12}$, the highest yet achieved for LPA-based mono-energetic Compton sources.

Our analysis suggests two opportunities for further improving x-ray conversion efficiency and brightness in future work. First, sharpening the density down-ramp at the gas jet exit can potentially improve the transmitted a_0 by as much as a factor of two [see black dashed and red curves in Fig. 5.7(b)], thus quadrupling the intensity of the backscattering pulse. Second, sharper relativistic curvature of the PM surface [see Fig. 5.9(a)] by a more intense transmitted drive pulse could potentially focus the retro-reflected light onto oncoming electrons. As an illustration of this effect for conditions of the present experiments, the waveforms in Figs. 5.9(b)-(c) show snapshots of the (x, y) and y-component of the electric field (E_y) in the incoming and reflected beam, respectively, $\sim 25\mu$m in front the PM surface, where the tightest focus occurs. The reflected beam is visibly more focused due to the curved PM surface, while E_y is $\sim 2\times$ higher [see blue curve in Fig. 5.9(c), compared

to 5.9(b)], corresponding to 4-fold intensity increase. Unfortunately, for current conditions, the electron bunch is only $\sim 10\mu$m behind the laser driver, so backscatter occurs only $\sim 5\mu$m from the PM surface, where the intensity enhancement is negligible. Nevertheless, this enhancement could become significant in LPA experiments at lower $\bar{n}_e$, in which the e-bunch propagates further behind the driver due to larger bubble size, or when the transmitted drive pulse has higher a_0.

5.5 Conclusion

In conclusion, we demonstrated quasi-monoenergetic Compton backscatter X-ray generation using the easily aligned combination of an LPA with a single drive pulse and a PM. The central x-ray photon energy was tuned from 75 KeV to ∼200 KeV, and can be scaled to MeV energy by tuning up e-beam central energy. The Compton source has photon number 2×10^7, divergence $\sim$ 10 mrad, and brightness 10^{19}photons s^{-1} mm^{-2} mrad^{-2} (per 0.1% bandwidth). Drive pulse transmission through the LPA and PM reflectivity were fully characterized by measurement and simulation, yielding a complete quantitative understanding of CBS x-ray properties.

Our analysis suggest that x-ray brightness could be increased as much as 10-fold In future experiments by sharpening the density down-ramp at the gas jet exit, and optimizing PM focus at relativistic intensity. Such improvements might also enable study of nonlinear Compton backscatter, which requires a strongly relativistic scattering pulse.

Chapter 6

Conclusion and outlook

Particle accelerators are among the most powerful tools for scientific discoveries in the twenty first century. At the frontier, where accelerators continue to unravel the knowledge of the universe, the proposed electron-positron linear collider based on current technology would already require tens of km of length as well as extensive needs for maintenance and man power. Laser plasma accelerators, which accelerate particles using plasma wakes driven by a short, intense laser pulse, have demonstrated high energy acceleration over distances shorter by a factor of a thousand. As an active part in this community, we have recently made great achievements in beam quality of hundred MeV LPAs [102] driven by the University of Texas Terawatt laser (UT^3) at Michael Downer's lab. Based on the combination of this LPA and PM, tunable hundred KeV CBS X-ray sources have also been demonstrated [103]. Using the Texas Petawatt Laser, Michael Downer's group recently also demonstrated high quality LPA electrons to world-record 2 GeV [107] and are pursuing improvement toward energies $>$ 10GeV. Enabling new high energy experiments and photon sources requires further improvement in beam energy spread, emittance, and efficiency. To do this , we must understand how the beam is accelerated and how it evolves during acceleration. The proposal of future experiments in this

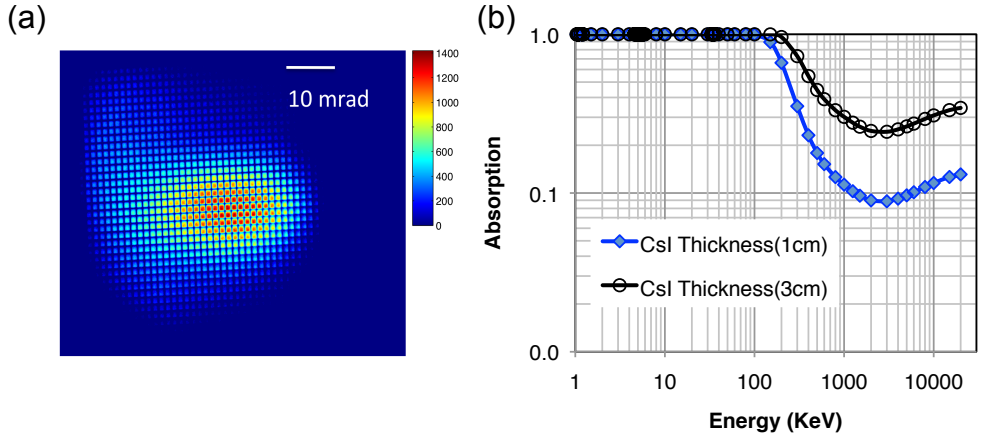

Figure 6.1: **(a)** Single shot CBS x-ray (80 KeV, 5×10^7 photon/shot) 100% absorbed by pixilated CsI(Tl) scintillator with high signal/noise ratio. **(b)** The absorption curve shows high absorption (30%) up to 10 MeV energy.

chapter is to list possible diagnostics for improving beam quality, and creating a compact bright source of ultra-short KeV-MeV photons, by exploiting scattering of a laser from the electron beam.

All these experiments could not be easily achieved without the single-shot X-ray detection technique with spatial and spectral resolution, which should be much more sensitive than image plate detection for high energy photons in the range of 10 KeV - 100MeV. By using the same LPA and PM configuration, we recently successfully demonstrated a single-shot detection of 80 KeV, 5×10^7 photons with a pixilated scintillator[Fig. 6.1 (a)]. The caesiumi odide doped with thallium [CsI(Tl)] scintillator has its absorption curve shows in Fig.6.1 (b) in which 30 cm thick one has high absorption 30% at 10 MeV energy. It will be used as our main X-ray detector in the coming

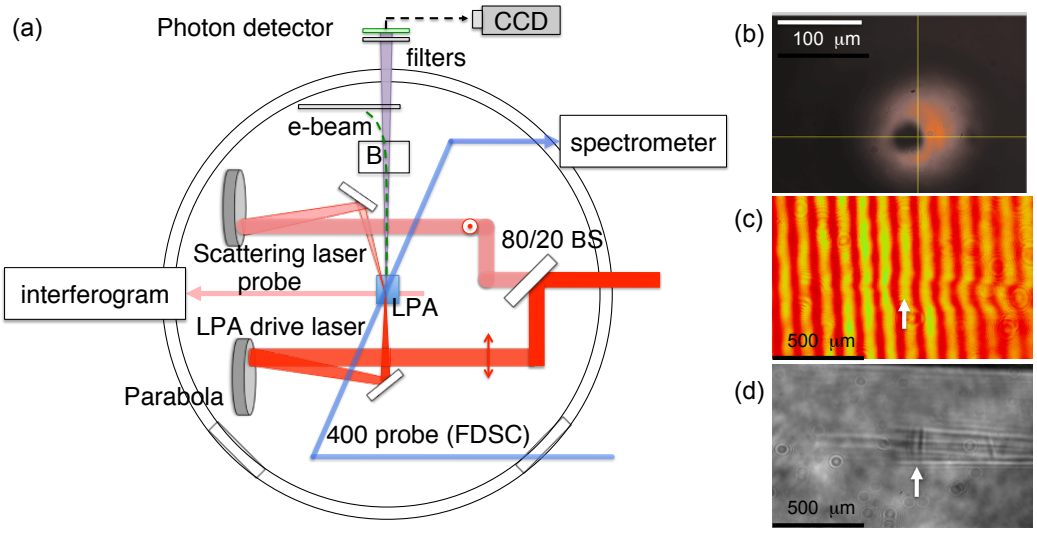

Figure 6.2: **(a)** The layout of CBS for e-beam diagnostics using split-off pulse. The spatial and temporal overlap between scatter and drive pulse can be done through ionization difraction pattern using **(b)** FDSC probe image (observed on spectrometer), **(c)** transverse interferogram and **(d)** transverse shadowgram (same setup as (c)). The arrow in (c) and (d) are the colliding points between two beams.

experiments described below.

6.1 CBS using split-off scatter pulse and e-beam diagnostics

Properties of scattered photons depend on the electron beam, making CBS a powerful tool to understand and improve LPAs. It is also a compact source of high brightness for KeV-MeV energy applications. The LPA is transparent to the low intensity scattering probe laser. This fact allows scattering at different longitudinal locations along the acceleration, revealing evolution of the particle beam energy gain, injection points, energy spread and angu-

lar spread, in conjunction with the FDH [22]and FDSC [65] techniques were developed to maturity in Michael Downer's group. This important combination is unprecedented. The number, emittance, energy, and spread of CBS X-ray photons pinpoint where and how efficiently electrons inject from the surrounding plasma into the laser-driven plasma wave at various injection points and conditions. The ability to precisely probe within the wakefield is unlike any other diagnostic available and would be extremely useful in exploiting various electron injection schemes such as density down ramp, colliding-pulse, and ionization-induced injection that LPA researchers are expiring to optimize and control the acceleration process[27]. The proposed experimental setup is shown in Fig.6.2(a). The LPA is shown at the center of the chamber, where drive pulse and scatter pulse collide. A 80/20 beamsplitter (BS) transmitting 20% of energy for scattering pulse, which is focused by a $f/12.5$ gold coated parabola to a $\sim 11\mu$m spot (FWHM). The maximum peak intensity is thus $\sim 2 \times 10^{18}$ W/cm^2 and $a_0 \sim 1$. The scatter pulse is designed with an oblique angle from LPA and drive pulse axis with S-polarization to prevent feeding back to the laser chain. The spatial and temporal overlap between drive pulse and scatter pulse has been demonstrated in the preliminary experiment using transverse and longitudinal imaging diagnostics. The oblique-angled, frequency-doubled probe pulse serving as FDSC diagnostic has a $\sim 50\mu$m beam size at the interaction region. Fig. 6.2 (b) shows the 0 order image in the spectrometer. The dark hole in the center is the diffraction pattern created by both drive pulse and scatter pulse ionizing the gas. A xyz-stage on a steering mirror of scatter

beam line can be adjusted to overlap the scatter pulse spot with drive pulse spot on xy-plane. Fig. 6.2 (c) and (d) are a transverse interferogram and a shadowgram, respectively. The channels created by scatter pulse (left) and drive pulse (right) are used for overlap on the yz-plane. The colliding point (white arrow) can be adjusted through tuning a delay stage on the scattering pulse, such that the colliding point is adjusted on the z direction. The overlap on y-direction can be done also by adjust the xyz-stage. The resulting CBS photon beam can be detected using a pixilated CsI(Tl) scintillator, which covers the energy range from KeV to MeV level. The energy-angle spectra can be obtained by placing a multi-element filter mosaic in front of the X-ray detector and fitting the observed transmission of each element as done in previous experiment described in chapter 5 and Appendix F.

The combination of high resolution CBS photon diagnostic with FDSC, FDH and VLPL simulations can capture a complete acceleration picture.

6.2 Enhancement of CBS brightness and energy

Our current method relies on a 90μm thick, plastic foil impeding the beam path directly after the LPA; the still focused, spent laser generates an over-dense plasma on the foil surface, acting as a mirror, allowing the pulse to retro-reflect into the oncoming electrons. Although the CBS source has been successfully demonstrated to have photon number 2×10^7, divergence ~ 10 mrad, and brightness 2×10^{19}photons s^{-1} mm^{-2} mrad^{-2} (per 0.1% bandwidth), we believe there is still room for improvement in terms of energy and bright-

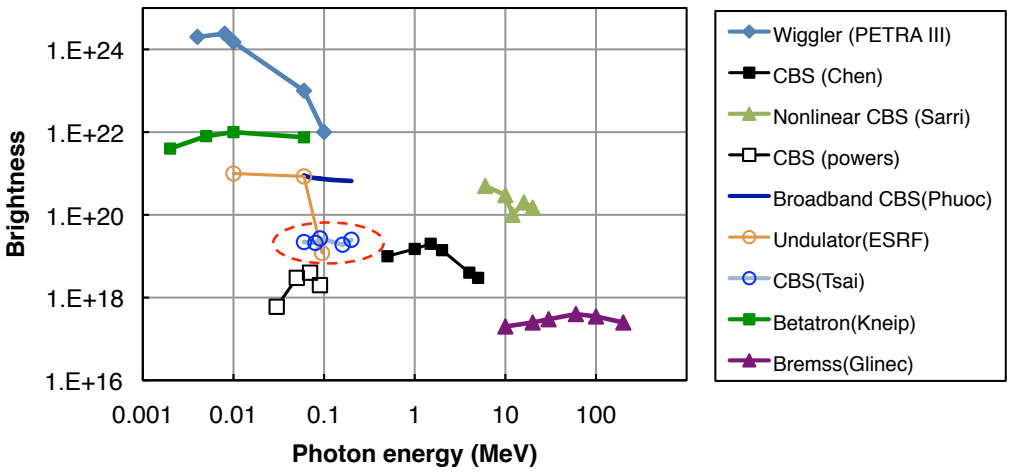

Figure 6.3: Comparison of peak brightness of various short-pulsed x-ray sources reported in recent literature: free-electron laser (PETRA III [1], blue diamonds), solid state undulators (ESRF [87], orange circles), betatron radiation from a LPA (Kneip *et al.*[53], green squares), bremsstrahlung radiation from a LPA and high-Z converter (Glinec *et al.* [39], purple triangles), nonlinear relativistic CBS (Sarri *et al.* [88], green triangles), quasi-monoenergetic CBS with split-off-pulse method (Chen *et al.*[13] and Powers *et al.*[82], black squares), broadband CBS with PM method (Phuoc *et al.*[98], blue line) and quasi-monoenergetic CBS with PM method (our work [103], blue circles). Brightness is expressed in the units of photons s^{-1} mm^{-2} $mrad^{-2}$/0.1% BW.)

ness. Fig. 6.3 compares the brightness of this x-ray source with that of other short-pulse x-ray sources reported recently in the literature: free-electron laser (PETRA III [1], blue diamonds), solid state undulators (ESRF [87], orange circles), betatron radiation (Kneip *et al.* [53], green squares), bremsstrahlung radiation from a LPA and high-Z converter (Glinec *et al.* [39], purple triangles), nonlinear relativistic CBS (Sarri *et al.* [88], green triangles), quasi-monoenergetic CBS with split-off-pulse method (Chen *et al.*[13] and Powers *et al.*[82], black squares), broadband CBS with PM method (Phuoc *et al.*[98],

blue line) and quasi-monoenergetic CBS with PM method (our work [103], blue circles). Our analysis suggests two opportunities for further improving x-ray conversion efficiency and brightness in future work. First, steepening the density down-ramp at the gas jet exit can potentially improve the transmitted a_0 by as much as a factor of two [see black dashed and red curves in Fig. 5.7(b)], thus enhancing four times the intensity of the backscattering pulse. Second, exploiting relativistic denting effect of the PM surface [see Fig. 5.9(a)] by a more intense transmitted drive pulse could potentially focus the retro-reflected light onto oncoming electrons. As illustrated in Figs. 5.9(b)-(c), the snapshots show the (x, y) and y-component of the electric field (E_y) in the incoming and reflected beam, respectively. The tightest focus occurs at $\sim 45\mu$m in front the PM surface. The reflected beam intensity is 2-3 times higher due to focusing by the curved PM surface. Unfortunately, for current conditions, the electron bunch is only $\sim 10\mu$m behind the laser driver, so backscatter occurs only $\sim 5\mu$m from the PM surface, where the intensity enhancement is negligible. Nevertheless, this enhancement could become significant in Petawatt LPA experiments at lower $\bar{n}_e$, in which the e-bunch propagates further behind the driver due to larger bubble size, or when the transmitted drive pulse has higher a_0. It has the potential to generate MeV photons for applications such as gamma neutron activation and pair production. On the other hand, the enhancement could also be possible by placing the thin PM inside the gas jet at the position where both the self-focused laser intensity and electron acceleration reach maximum values without invasively perturbing the gas profile.

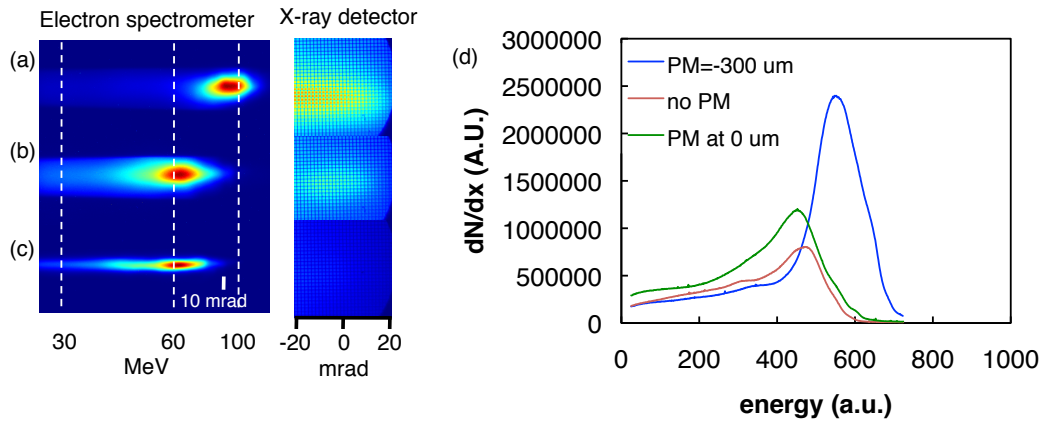

Figure 6.4: **(a)** Measured electron spectrum and X-ray signal by placing PM at -300 μm from gas jet exit. **(b)** Measured electron spectrum and X-ray signal by placing PM at gas jet exit. **(c)** Measured electron spectrum and X-ray signal without the presence of PM. **(c)** Measured electron spectra at the conditions of (a),(b) and (c)

6.2.1 Hundred KeV CBS on Terawatt LPA

In the previous work done by Phuoc *et al*[98], the optimum CBS signal was achieved by placing PM at gas jet exit position. We also obtained the maximum yield at the exit position by investigating various positions outside LPA. However, further verification needs to be done by placing PM inside LPA. Since we have recently developed single-shot detecting technique and the thin PM tape drive roller, we can now do PM experiment inside LPA without perturbing gas profile. Encouragingly, in our preliminary experiment, we found not only the electron central energy changing with PM position, but also the electron charge and CBS signal enhanced with the PM inside the gas jet. Especially, we found the electron central energy, charge number and CBS signal were all peaked when placing the PM at -300μm, which is 700μm

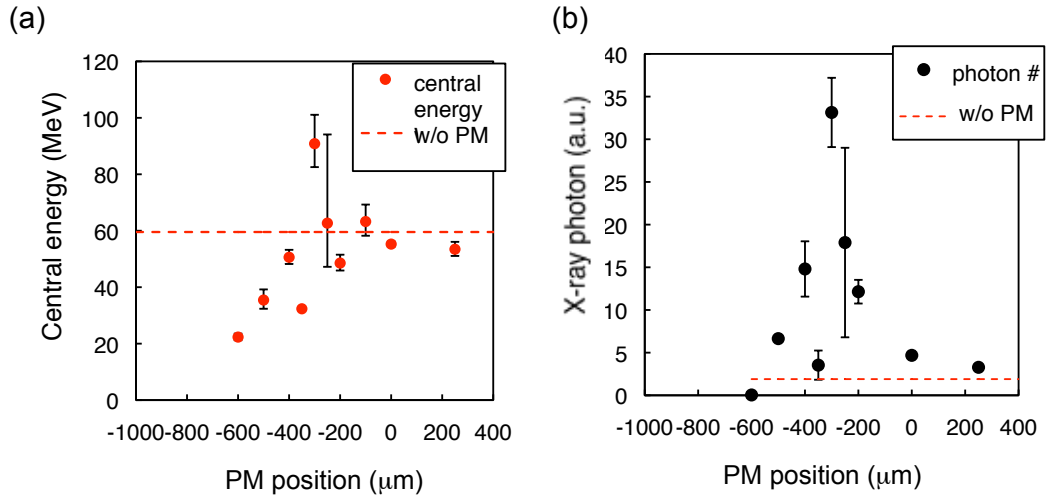

Figure 6.5: **(a)** Measured electron central energy varies as a function of PM position. **(b)** Measured CBS photon number varies as a function of PM position. gas jet entrance: -1000μm; gas jet exit: 0μm.

behind the gas jet entrance. Here -1000 μm is the entrance and 0μm is the exit of LPA.

Fig. 6.4 (a) shows the electron spectrum and CBS beam profile when varying the PM position inside the LPA. Both the central energy and CBS signal are higher than those obtained when placing the PM at 0 μm [Fig. 6.4(b)] or without PM [Fig. 6.4(c)] . In particular, the electron central energy was 100 MeV and CBS signal was enhanced by a factor of seven over placing it outside gas jet [Fig. 6.5(a) and (b)]. The possible reason is that the acceleration happened only in a certain region inside 1mm length. For example, electron bunch was injected at -700μm, gaining energy from -700 to -300μm, dephasing from -300 to 0μm. When PM was inserted inside, it

actually divided the gas jet effective length for laser-plasma interaction. In a sense, it can provide acceleration information at various position. The follow-up experiment should be able to repeat the enhancement result. The seven times CBS enhancement itself is substantial, making us to the brightest source among all LPA based sources. We can further investigate how the electron energy, energy/spatial spread, and charge evolve along the acceleration axis. It can be achieved by partially blocking the gas jet outlet with a razor blade. It creates the equivalent outcome as dividing the gas jet by inserting PM inside. Meanwhile, the spent drive pulse intensity profile will be imaged onto a CCD. To do this, a thin pellicle foil will be applied to reflect drive pulse to the imaging system without perturbing the e-beam. With both scattering pulse intensity along with electron charge and energy, we can explain and justify the measurement result of CBS photon number and energy. It is also potentially a compact and simple experiment proposal for LPA beam diagnostics.

6.2.2 MeV CBS source and positron source on Petawatt LPA

CBS can provide a polarized positron or muon source [21] for HEP experiments by exploiting the fact that the process preserves the polarization of scatter pulse. LPA electron beams are both a compact source of the required energy for generating positrons, and suitable to generate positron beams for future LPA experiments towards colliders. Production of positrons requires scattering with the GeV-class LPA driven by the Texas Petawatt laser. Electrons at 650 MeV would produce 10 MeV photons for subsequent

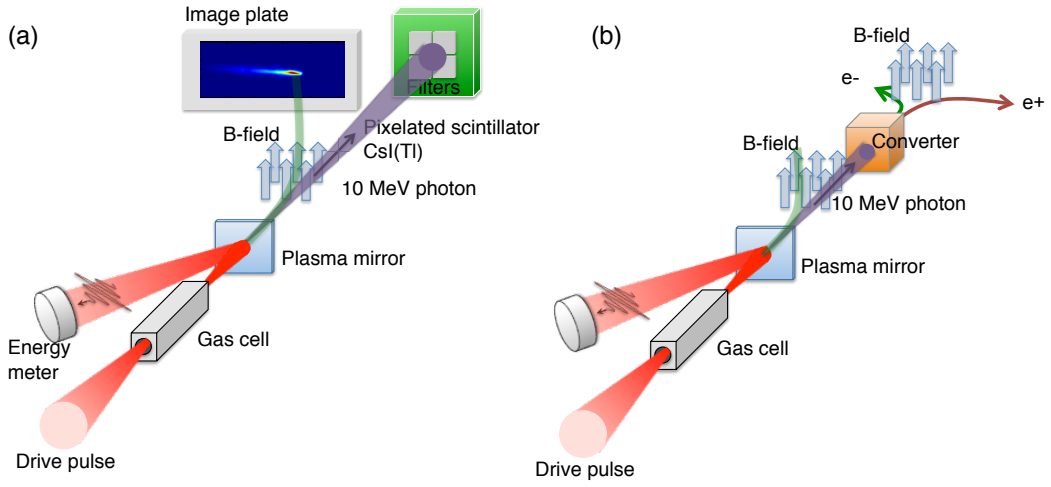

Figure 6.6: **(a)** Setup for 10 MeV CBS generation on Petawatt LPA. **(b)** CBS gamma ray driven positron generation on Petawatt LPA.

conversion to positrons, which would be characterized in the existing electron magnetic spectrometer. In fact, a broader window, roughly across 0.5 -2 GeV, of electron beams energy can be used to effectively generate positrons. A tape drive based plastic PM has been developed. Reflectivity $> 70\%$ for intensity $10^{18} - 10^{19}\mathrm{W/cm^2}$ without degradation in laser spot quality has been demonstrated [103]. Placing PM immediately outside the gas cell would reflect the highest intensity form the spent drive pulse close to $a_0 \sim 1$. This would produce gamma rays with total photon yield in the range of $10^7 - 10^8$. We will first characterize the gamma ray photon number and energy by using the combination of a filter mosaic and a CsI(Tl) array (Appendix F). Moving the PM downstream would allow the laser to diffract before reflection, allowing narrower bandwidth at $a_0 \sim 0.3 - 0.6$ and photon yield $10^6 - 10^7$ range. The petawatt laser pulse has a lower contrast ratio that would critically determine

the performance of a PM. Therefore, the reflectivity of PM is to be measured. A frequency-doubled laser pulse will be used to probe the PM surface at the arrival time of drive pulse to measure the spatial reflectivity. The reflected drive pulse will be collected by an energy meter. The GeV electron beam would be diverted using an existing 1T magnet, which would be mounted right after the PM. The gamma rays would then be converted into electron-positron pairs in a converter [Fig. 6.6 (b)], and analyzed in the magnet spectrometer. Using a target of 0.5 radiation lengths, $\sim$ 1% yield is anticipated[3], or 10^5 positrons/shot.

Appendices

Appendix A

Laser and beam monitor systems for experiments

A.1 Laser systems

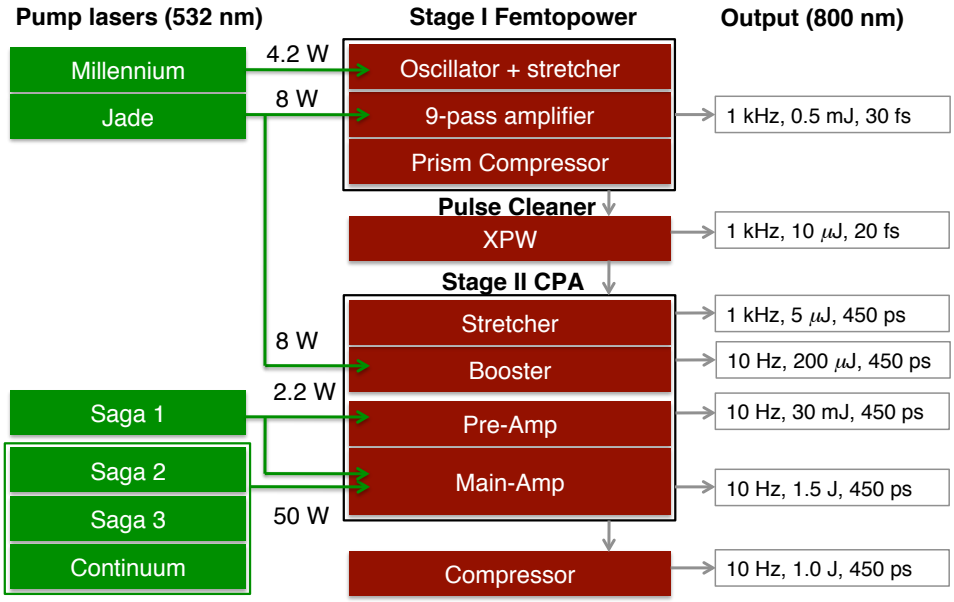

Figure A.1: Schematic diagram of the UT^3 Alpha 10/XS 45 TW laser system

Experiments in this dissertation involving optimization of tunable quasi-monoenergetic LPA, PM reflectivity and CBS x-ray generation utilized the 30-TW UT^3 laser system at the University of Texas at Austin, which operates with 10-Hz repetition rate at central wavelength 800 nm (photon energy

	Femtopower	Booster	Pre-Amp	Main Amp	Compressor
Original spec	800 μJ	850 μJ	30 mJ	1750 mJ	1130 mJ
Current spec	400 μJ	200 μJ	30 mJ	1500 mJ	1000 mJ

Table A.1: Original and current specifications of the UT^3 Alpha 10/XS 45 TW laser system

E_L = 1.5 eV). Fig. A.1 shows the schematic setup and specification. For laser-plasma acceleration experiments, the laser power should exceed the relativistic critical power of plasma P_{cr} $\approx$17$(\omega/\omega_p)^2$ GW. Thus the laser pulse energy varies based on the plasma density. Laser-plasma accelerators at 10^{19} cm^{-3} density that produce 100 MeV electron beams requires multi-terawatt laser power and laser energy of 1 joule, whereas laser-plasma accelerators at 10^{17} cm^{-3} density for multi-GeV electrons needs petawatt laser with 100-J energy per pulse.

Here the laser systems for these experiments are reviewed. The UT^3 Ti:Sapphire laser is a commercial system (Alpha 10/XS) from Thales Lasers. The original and current specifications of the system are shown in Table A.1. The whole system consists of two stages of chirped pulse amplification (CPA) [Fig. A.1]. The first stage is a compact laser system from Femtolasers with one kilohertz output of 30 fs laser pulses centered at 800 nm. The maximum output pulse energy is 1 mJ. However, in practice it is attenuated to 0.2 mJ using a half-wave plate and polarizer in order to avoid optical damage in the cross-polarization wave (XPW) generator for pulse cleaning. The cleaned pulses are chirped to 400 ps in the grating stretcher and amplified to 0.2 mJ in the

booster, then they are sent to amplifiers. The pre-amplifier is pumped by a small portion of the SAGA1 laser (220 mJ). Seed light travels passes through a Ti:Sapphire crystal to be amplified to 40 mJ. The main amplifier has three passes and is pumped by four pump lasers, thus the seed beam is amplified to 1.5 J per pulse. After the grating compressor, the pulse is compressed back to 30 fs, and pulse energy is around 1000 mJ. Using this system, laser energy of widely different orders of magnitude is obtainable by coupling the beam out at different stages. For glass filamentation experiments, the kilohertz output of the front end is directly used to provide microjoule level laser pulses. To study laser filamentation in air, the output from the pre-amplifier is compressed by a separately built grating compressor to yield 20 mJ, 40 fs laser pulses. Laser plasma acceleration experiments were conducted with full laser power.

A.2 Beam monitor systems

The output energy from main amplifier is around 1.5-2 J per pulse. The damage threshold fluence on the compressor gratings is $\sim$ 200 mJ/cm^2. Any hotspot in amplified beam profile is detrimental to gratings. It is necessary to monitor the pump beam laser profiles while operating the experiment. The pump beam monitor cameras are installed in 2011 to serve the purpose of monitoring the pump beam profiles on the Ti:sapphire crystal. The schematic of main amplifier layout and cameras are shown in Fig. A.2. The cameras are taking the leak out light from Y2 mirrors and imaging the position near the crystal surface. The images are processed and presented on a monitor PC on

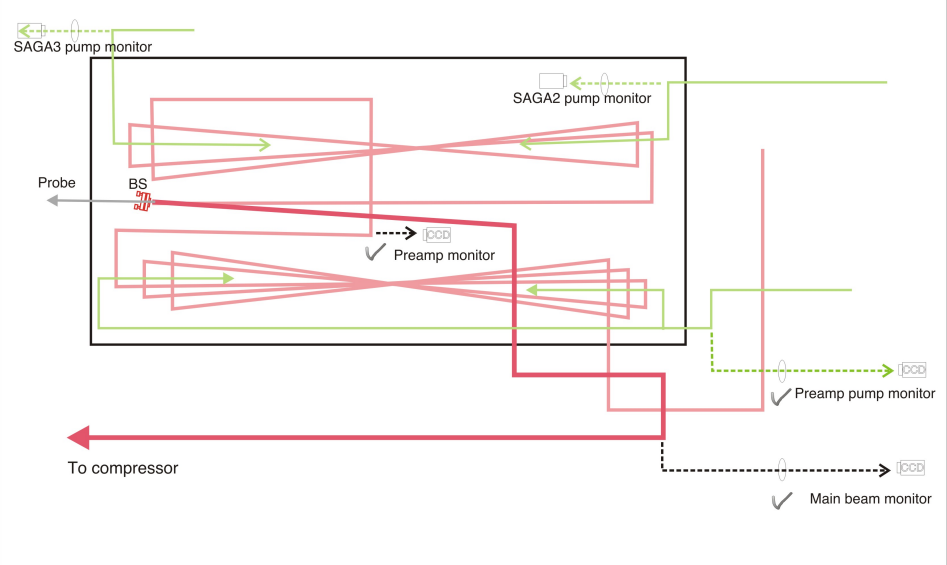

Figure A.2: Schematic diagram of the main amplifier and the beam-monitor cameras

the control desk. A Labview program named " PUMP LASER profile monitor.vi" can show beam intensity profiles, horizontal and vertical lineout, peak fluence, and energy of SAGA1, SAGA2, SAGA3 and Continuum (Fig.A.3).

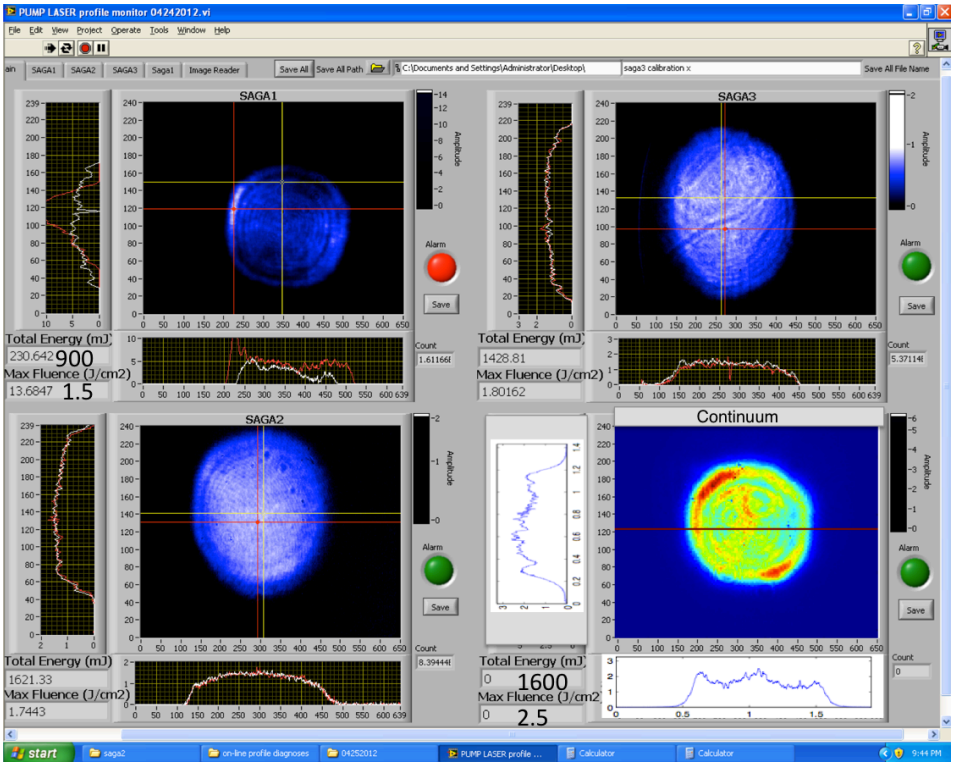

Figure A.3: The screenshot of the pump beam monitor program " PUMP LASER profile monitor.vi". The program can show beam intensity profiles, horizontal and vertical lineout, peak fluence, and energy of SAGA1, SAGA2, SAGA3 and Continuum.

Appendix B

Laser focal spot optimization

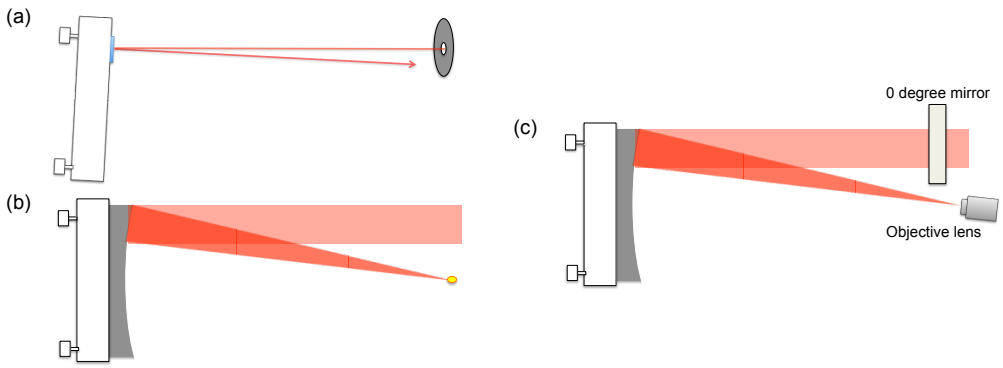

Figure B.1: Schematic of alignment procedure for a parabolic mirror

The laser plasma acceleration experiment demands high-quality focal spot. Any spatial chirp and astigmatism, which are directly leading to poor focus quality and detrimental to acceleration result. To obtain and optimize a good quality focal spot is the first priority to begin with the experiment. The focusing optics we used in the experiment is an Edmund Optics' 6" Diameter $\times$24" focal length, protected gold coated, parabolic mirror. Here I list few basic steps to produce a good quality focus. Before the alignment, a 800-nm IR viewer, a sensitive IR card, and a thin aluminum mirror have to be ready in hand.

1. Remove the parabolic mirror and attach a thin aluminum mirror on the parabolic mirror mount like shown in Fig. B.1 (a). Make sure the incident beam is correctly centered on irises and the aluminum mirror. Use IR viewer to check the reflected beam spot on a far iris. Tweak the mirror mount knobs to center the reflected spot on the iris. This stop is to make sure the normal direction of the mount is parallel to the incident direction.

2. Install the parabolic mirror and open all irises. the vertical level of the incident beam should be in the center of the parabola. The horizontal position of the incident beam is 2" away from the center. The main beam energy is lower than 10 mJ. The focus can ionize air and produce a white spark, which can be seen with bare eyes like shown in Fig. B.1 (b). Tweak the parabola horizontal angle so the spark is most intensive. Tweak also the vertical angle slightly to maximize the spark intensity (shouldn't tweak too much). The energy can be lowered so that the optimization is easier.

3. Instal a 0 degree mirror to attenuate most of the beam energy and a 20× objective lens with a CCD capturing the image like shown in Fig. B.1 (c). The objective lens is mounted on a xyz-stage and the CCD is connected to a image analyzing software, "*energycapture.vi*", which can calibrate the beam size, fluence and energy. The focus can be detected using a sensitive IR card. The xyz-stage of the objective lens is adjusted so that

the beam intensity is maximum and beam waist is minimum. Record the beam fluence and beam FWHM. Adjust the parabola mount to move the focal spot position 1cm upward, downward, left and right. Record the focus information of nine points on this 2×2 cm^2 map. Evaluate the beam quality from nine point. Fine out the optimal position. This step is to achieve fine optimization.

The ideal intensity should be around or larger than 6×10^{18}W/cm^2 with fully amplified energy(1.5 J), 11μm FWHM and $> 70\%$ Strahl ratio. If the focal spot is far from ideal. The very possible causes, according to experiences, can be misalignment of compressor gratings and both telescopes in and out of the main amplifier. The symptom of compressor misalignment is horizontal broadening in beam size, like 50 μm. The misalignment of telescope on amplified beam can cause astigmatism, which results in unsymmetric focus on z direction. The focus is elongated vertically before z_0 and horizontally after z_0, where z_0 is the z position of focus.

Appendix C

Compressor gratings alignment procedure

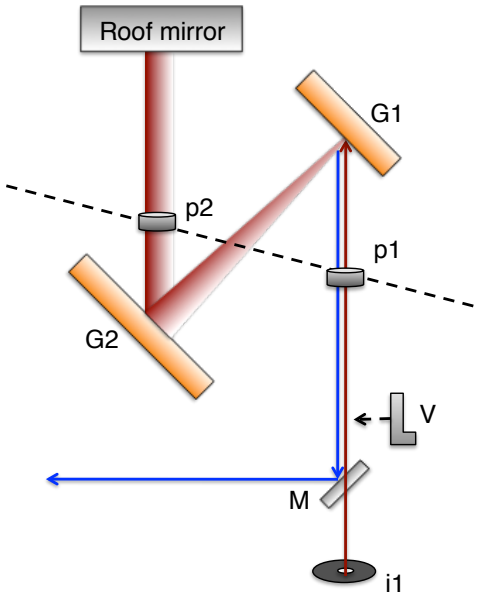

Figure C.1: Schematic diagram of main pulse compressor and checking points of alignment procedure

The main pulse compressor is composed of two holographic gold coated gratings and a rooftop mirror. The schematic of compressor configuration is shown in Fig. C.1. The incident beam is at a level of 30cm from chamber breadboard (red line), while the return beam is down-translated by the rooftop mirror to the level of 25 cm from chamber breadboard (blue line). Both grat-

ings mounted on rotational stages can be adjusted such that the beam is 46.3° incident and −28.42° diffracted to both grating normal direction. The rooftop mirrors composed of two square mirrors placed 45° downward and upward respectively are used to down-translate and retro-reflect the beam. The rooftop mirrors are also adjusted such that the return path overlap the incident path on the vertically plane. The alignment procedure has two parts. The first part is to assume both gratings parallel to each other and return path overlapped incident path on the vertical plane. The steps are as follow:

1. Prepare a 800-nm IR viewer, sensitive IR card, an aluminum mirror mounted on a translating rail track.

2. Place the rail track across the light paths between two gratings (dashed line in Fig. C.1.

3. Adjust the laser energy lower than 30 mJ. Align the incident light beam (center two irises before the first grating using IR card).

4. Translate the aluminum mirror to p1 position and adjust the mirror mount such that the retro-reflected beam return the center of iris 1 (i1, using IR viewer to observe the return spot)

5. Translate the mirror to p2 position and adjust the rotation angle of first grating (G1) such that the retro-reflected beam center the iris 1 (i1).

6. Remove the mirror and track. Place the vertical ruler at the position such that half of the beam is blocked (blue line).

7. Adjust the rooftop mirror such that the returning half beam edge overlaps with the ruler edge. This step is to make sure incident path(red) overlaps with out-going one(blue) vertically. Ideally, two positions along the blue and red lines should be checked

8. Check the output iris (the iris after mirror ,M , and before a single shot auto-correlator), if it's not centered, move the iris to center the beam.

The second part is to optimize the pulse duration by tuning the angle and separation between two parallel gratings. The steps are as follow:

1. Send the output beam to an auto-correlator. The standard procedure of operating an auto-correlator includes the calibration of the time/pixel value, Gaussian-fitting of the correlation trace and readout of pulse duration.

2. Tune the gratings separation until reach the shortest duration. Record the grating angle and pulse duration.

3. Walk off the angle of first grating(G1) by a small amount, for example, 1cm horizontal deviation on the iris of the auto-correlator. Compensate the deviation by adjusting the angle of the second grating(G2). This step is to walk off both gratings with exact the same angle.

4. Translate the grating separation to reach the shortest pulse. Record the angle and pulse duration.

5. Keep doing last two steps until you find the optimal angle. The pulse duration should be as short as 25 fs on specification

6. Secure the rotational stages. Keep the beam sending into the auto-correlator while pumping down

7. In the vacuum, the grating separation will be adjusted again to get the shortest duration(-4000 to -5000 steps on the Zaber motor)

The laser parameters and grating specifications are listed below:

Laser parameter:

1. 10 Hz repetition rate

2. max energy= 1.5 J

3. beam diameter (clear aperture, the diameter which 99% energy enclosed)= 5.5 cm

4. central wavelength= 810 nm

5. bandwidth= 40 nm

6. polarization= P (perpendicular to grooves direction)

7. The pulse duration is compressed from 200 ps to 35 fs

Grating specification:

1. gold coating
2. grating 1 dimension: Height 140($original$170)$\times$ Width 120$\times$ Thickness 30 mm^3
3. grating 2 dimension: Height 165$\times$ Width 220$\times$ Thickness 30 mm^3
4. groove density: 1480 g/mm (holographic, the grooves are parallel to the 170 mm dimension)
5. spectral range: 700-850 nm
6. incidence angle: 46.3°
7. diffraction angle: $-28.42°$
8. surface flatness: lambda/6
9. efficiency $\sim 90\%$ on single pass
10. damage threshold: 0.4 J/cm^2 for ns pulse and $0.1-0.2$J/cm^2 for fs pulse

Appendix D

The interferometry and density reconstruction algorithm

D.1 Interferometry

Interferometry is a standard technique for measuring electron density profile. It restores the phase shift experienced by a probe beam as it transverses the plasma. The phase shift is caused by the variation of refractive index in the plasma as a function of plasma density. The refractive index η is a function of plasma density n_e given by

$$\eta = \sqrt{1 - \frac{n_e}{n_c}} \tag{D.1}$$

where n_c is critical density. If $n_e \ll n_c$, the above equation can be approximated as

$$\eta \approx 1 - \frac{n_e}{2n_c} \tag{D.2}$$

Fig. D.1 (a) shows the coordinate frame in the plasma, in which it is assumed that the absorption is negligible and the plasma has cylindrical symmetry with the axis of pump laser direction (y). The optical path length $l(x)$ of the probe light in the plasma becomes

$$l(x) = 2\int_x^{r_0} \frac{\eta(r)r}{\sqrt{r^2 - x^2}} dr \tag{D.3}$$

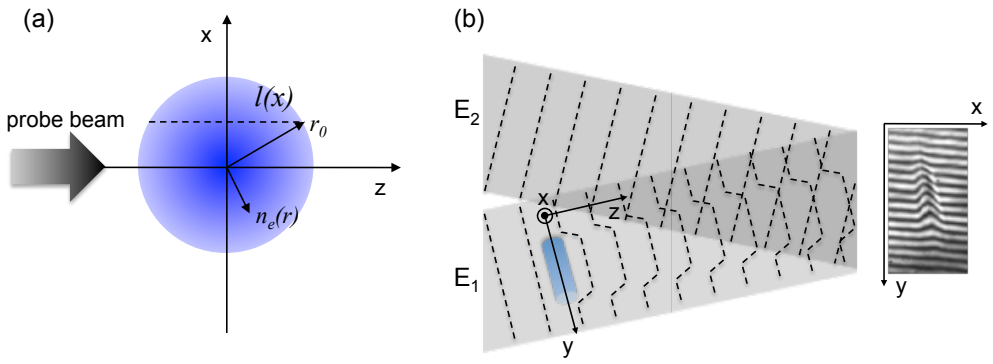

Figure D.1: Schematic of interferometry: (a) Cylindrical symmetric plasma. (b) E_1 and E_2 are probe beam and reference beam respectively.

Here $\eta(r)$ is the refractive index. optical path length $l_0(x)$ in the vacuum is

$$l_0(x) = 2\int_x^{r_0} \frac{r}{\sqrt{r^2 - x^2}} dr \tag{D.4}$$

Therefore, the difference of length between the path in vacuum and in plasma is

$$l(x) - l_0(x) = -\frac{1}{n_c}\int_x^{r_0} \frac{n_e(r)r}{\sqrt{r^2 - x^2}} dr \tag{D.5}$$

The phase shift $\phi(x)$ becomes

$$\phi(x) = -\frac{2\pi}{\lambda n_c}\int_x^{r_0} \frac{n_e(r)r}{\sqrt{r^2 - x^2}} dr \tag{D.6}$$

The radial distribution of electron density $n_e(r)$ can be obtained by applying Abel transformation technique[20].

$$n_e(r) = \frac{\lambda n_c}{\pi^2}\int_x^{r_0} \frac{d\phi(x)}{dx}\frac{1}{\sqrt{x^2 - r^2}} dx \tag{D.7}$$

We can obtain the phase shift of the probe beam from the interferogram. The fringe pattern like the one shown in Fig. D.1 (b) can be described by

intensity distribution

$$I_s = |E_1 + E_2|^2 = |E_0 e^{i(k_0 y + \phi(x,y))} e^{-i\omega t} + E_0 e^{ik_0 y} e^{-i\omega t}|^2 \tag{D.8}$$

$$= 2|E_0|^2 \{1 + \cos[2k_0 y + \phi(x,y)]\} \tag{D.9}$$

The background fringe pattern can be obtained without plasma being presented

$$I_{bg} = 2|E_0|^2 [1 + \cos(2k_0 y)] \tag{D.10}$$

where $\phi(x,y)$ is the phase shift information, k_0 is the spatial-carrier frequency. After fast Fourier transform, both can be written as

$$FFT[I_s] = \delta(\xi) + \frac{1}{2}\delta[\xi + (2k_0 + \psi)] + \frac{1}{2}\delta[\xi - (2k_0 + \psi)] \tag{D.11}$$

$$FFT[I_{bg}] = \delta(\xi) + \frac{1}{2}\delta[\xi + 2k_0] + \frac{1}{2}\delta[\xi - 2k_0] \tag{D.12}$$

where δ denote the Fourier spectra and ξ is the spatial frequency in the y direction. in Fig. D.2 (c) and (d), two Fourier spectra are peaking at different ξ. $\delta[\xi - (2k_0 + \psi)]$ and $\delta(\xi - 2k_0)$ can be extracted. Fig. D.2 (e) and (f) shows the Fourier spectra after extraction. Then both are inverse Fourier transformed to obtain

$$I'_s = IFT\{\delta[\xi - (2k_0 + \psi)]\} = |E_0|^2 e^{i[2ky + \phi(x,y)]} \tag{D.13}$$

$$I'_{bg} = IFT\{\delta(\xi - 2k_0)\} = |E_0|^2 e^{i2ky} \tag{D.14}$$

So we can calculate the phase shift deviding Eq. D.13 by D.14

$$\phi(x,y) = Arg\left[\frac{I'_s}{I'_{bg}}\right] \tag{D.15}$$

Therefore we can solve for electron density substituting $\phi(x,y)$ in Eq. D.7.

D.2 Electron density reconstruction codes

The Electron density reconstruction codes are named "InterferogramPhaseshift.m", "AbelInversion.m", "dPdx2Electrondensity.m". They runs on a personal computer with Windows or Mac operating system. The codes are written in Matlab.

"InterferogramPhaseshift.m"

The first step is to run "InterferogramPhaseshift.m" to calculate phase shift from interferogram. This code written based on Eq. D.15 and its user's guide are list below.

```
% a = InterferogramPhaseShift(1, 'IF-3-73.fit', 'IF-3-71.fit', 'IF-3-73-parameters.txt');

% InterferogramPhaseShift_v6
%
%    Syntax: InterferogramPhaseShift(FigureSwitch, SourceFilename, ReferenceFilename, ParameterFil
%
%       FigureSwitch:
%          FigureSwitch = 0: no figures
%          FigureSwitch = 1: generate figures
%
%       source & reference file:
%          BMP, TIFF or FITS... image file, vertical fringes.
%
%       parameter file (ASCII-type file):
%          element 1: Row_min
%          element 2: Row_max
%          element 3: Column_min
%          element 4: Column_max
%          element 5: Mask_range_up
%          element 6: Mask_range_down
%
%       returned value:
%          phase shift (2-D matrix)
%
%       output files:20psi
%          (1) Matlab binary file, 2-D matrix (.mat)
%          (2) 8-bit BMP file
%
%       example:
%          a = InterferogramPhaseShift(1, 'IF-1-04.fit', 'IF-1-01.fit', 'IF-parameters.txt');
```

```
%
%    Hai-En Tsai 2010

function result = InterferogramPhaseShift_v6(FigureSwitch, SourceFilename,
ReferenceFilename, ParameterFilename)

% Loading the parameter file
ProgramParameters = load(ParameterFilename);
Rmin = ProgramParameters(1);
Rmax = ProgramParameters(2);
Cmin = ProgramParameters(3);
Cmax = ProgramParameters(4);
filter_range_up   = ProgramParameters(5);
filter_range_down = ProgramParameters(6);

% importation of the interferogram
SourceData    = imread(SourceFilename); % SourceData    = SourceData';
SourceData    = double(SourceData(Rmin:Rmax,Cmin:Cmax));
ReferenceData = imread(ReferenceFilename);
ReferenceData = double(ReferenceData(Rmin:Rmax,Cmin:Cmax));
[RowNumber, ColumnNumber] = size(SourceData);

% rescaling, Fourier transformation, and filtering
filter_range      = [filter_range_up, filter_range_down];
SourceSpectrum    = Rescaling_FT_Filtering(SourceData, filter_range);
ReferenceSpectrum = Rescaling_FT_Filtering(ReferenceData, filter_range);

Source_FT      = SourceSpectrum.original;
Source_FT_F    = SourceSpectrum.filted;
Reference_FT   = ReferenceSpectrum.original;
Reference_FT_F = ReferenceSpectrum.filted;


% inverse Fourier transform
Source_back          = ifft(Source_FT_F')';
Source_back_real     = real(Source_back);
Reference_back       = ifft(Reference_FT_F')';
Reference_back_real = real(Reference_back);

if FigureSwitch
    figure;
    colormap(gray(256));
    subplot(4,2,1), imagesc(SourceData),             title('source');
    subplot(4,2,2), imagesc(ReferenceData),          title('reference');
    subplot(4,2,3), plot(abs(Source_FT(1,:))),       title('source spectrum (row 1)');
    subplot(4,2,4), plot(abs(Reference_FT(1,:))),    title('reference spectrum (row 1)');
    subplot(4,2,5), plot(abs(Source_FT_F(1,:))),     title('filted spectrum (row 1)');
    subplot(4,2,6), plot(abs(Reference_FT_F(1,:))), title('filted spectrum (row 1)');
   subplot(4,2,7),imagesc(Source_back_real),       title('filtered source');
    subplot(4,2,8), imagesc(Reference_back_real),    title('filtered reference');
end

% phase shift calculation
PhaseShift = angle(Source_back ./ Reference_back);
PhaseShift = PhaseShift(:,11:ColumnNumber-10);
PhaseShift = PhaseCompensation(PhaseShift);
```

```
PhaseShift = BackgroundSubstration(PhaseShift);

if FigureSwitch
    figure;
    colormap(gray(256));
    colormap(jet);
    imagesc(PhaseShift);
end

% data exportation
temp = strtok(SourceFilename,'.');
OutputFilename  = strcat(temp,'_PhaseShift.mat');
save(OutputFilename,'PhaseShift');
OutputImageName = strcat(temp,'_PhaseShift.bmp');
MaxValue = max(max(PhaseShift));
MinValue = min(min(PhaseShift));
OutputImage = (PhaseShift - MinValue)/(MaxValue - MinValue)*255;
colormap(gray(256));
colormap(jet);
imwrite(OutputImage,colormap,OutputImageName,'bmp');

PhaseShiftmin = -min(min(PhaseShift))

result = PhaseShift;

% ------------------------------------------------------------------------
% OpenImageFile
%    Open an image file. ('FITS','TIF','BMP','JPEG','PNG',and 'HDF'... formats)
%    Return a 2D matrix.
%
%
% ------------------------------------------------------------------------

function result = OpenImageFile(Filename)

[SourceFilename_1 SourceFilename_2] = strtok(Filename,'.');
SourceFilename_2 = SourceFilename_2(2:length(SourceFilename_2));

if strcmpi(SourceFilename_2, 'FITS')
   source = fitsread(Filename);
elseif strcmpi(SourceFilename_2, 'FIT')
   source = fitsread(Filename);
elseif strcmpi(SourceFilename_2, 'FTS')
   source = fitsread(Filename);
elseif strcmpi(SourceFilename_2, 'png')
    source = imread(Filename);
else
   source = load(Filename, SourceFilename_2);
end

dimension = size(source,3);
if dimension == 3
   source = RGB2gray(source);
   image = double(source);
else
   image = double(source);
```

```
end
result = image;

%-------------------------------------------------------------------------
% Rescaling_FT_Filtering
%
%    Rescaling, Fourier transformation and Filtering of the input interferogram
%-------------------------------------------------------------------------

function result = Rescaling_FT_Filtering(input, filter_range)
[RowNumber, ColumnNumber] = size(input);

% rescaling
temp = double(input);
MaxValue = max(max(temp));
MinValue = min(min(temp));
temp = (temp - MinValue)/(MaxValue - MinValue);

% Fourier transformation and filtering
temp_FT = fft(temp')';
mask = zeros(RowNumber, ColumnNumber);
mask(:,filter_range(1):filter_range(2)) = 1;
temp_FT_F = temp_FT .* mask;
spectrum.original = temp_FT;
spectrum.filted   = temp_FT_F;
result = spectrum;


%-------------------------------------------------------------------------
% PhaseCompensation
%
%    Compensate the phase jump from Pi to -Pi and from -Pi to Pi.
%-------------------------------------------------------------------------

function result = PhaseCompensation(PhaseShift)

[RowNumber, ColumnNumber] = size(PhaseShift);

diff_col = zeros(RowNumber, ColumnNumber);
diff_col(:,2:ColumnNumber) = PhaseShift(:,1:ColumnNumber-1)-PhaseShift(:,2:ColumnNumber);
flag_1 = (diff_col > 3) - (diff_col < -3);
flag_2 = cumsum(flag_1,2);

PhaseShift_2 = PhaseShift + 2 * pi * flag_2;

diff_row = zeros(RowNumber, 1);
diff_row(2:RowNumber,1) = PhaseShift_2(1:RowNumber-1,1) - PhaseShift_2(2:RowNumber,1);
flag_3 = (diff_row > 3) - (diff_row < -3);
flag_4 = cumsum(flag_3);
flag_4(:,2:ColumnNumber) = 0;
flag_4 = cumsum(flag_4,2);

result = PhaseShift_2 + 2 * pi * flag_4;

%-------------------------------------------------------------------------
% BackgroundSubstration
```

```
%
%     Substract of the linear background phase
% ------------------------------------------------------------------------

function result = BackgroundSubstration(PhaseShift)

[RowNumber, ColumnNumber] = size(PhaseShift);

x = [1:ColumnNumber];
Background = mean(PhaseShift([11:20,RowNumber-19:RowNumber-10],:));
LinearFit_coefficient      = polyfit(x, Background,1);
LinearFit_BackgroundPhase = polyval(LinearFit_coefficient, x);
BackgroundPhase = zeros(RowNumber, ColumnNumber);
for i = 1:ColumnNumber
    BackgroundPhase(:,i) = LinearFit_BackgroundPhase(i);
end

result = PhaseShift - BackgroundPhase;
```

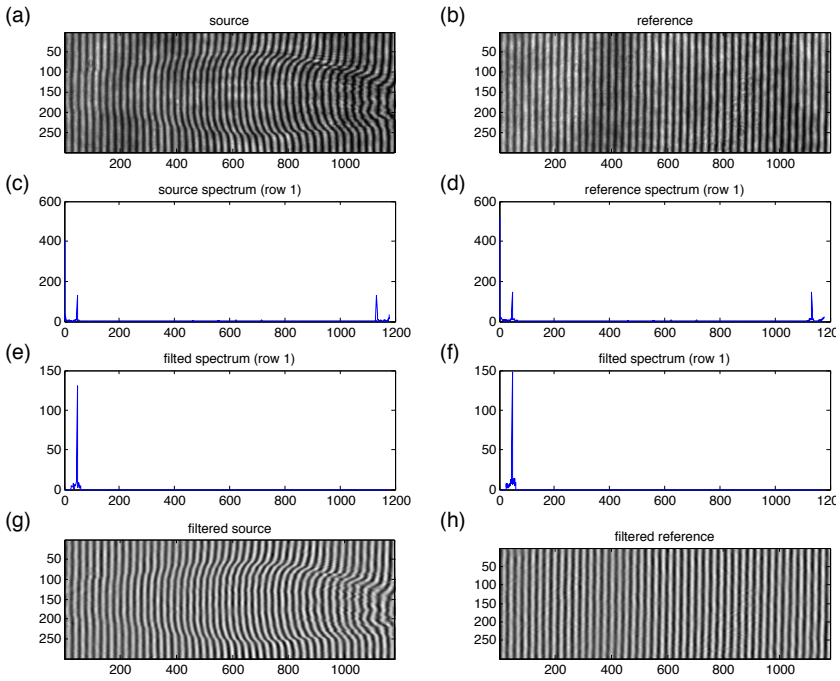

Figure D.2: The raw interferogram images of source (left column) and reference (right column). (a) and (b) are the raw image, (c) and (d) are the Fourier spectra, (e) and (f) are Fourier spectra extracted. (g) and (h) are inverse Fourier transformed interferograms.

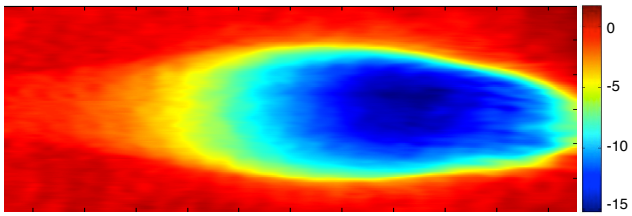

Figure D.3: The phase shift image converted from the interferogram shown in Fig. D.2

The output of "InterferogramPhaseshift.m"

The output of "InterferogramPhaseshift.m" are shown in Fig.D.2 and Fig.D.3. The raw images of source [Fig.D.2(a)] and reference [Fig.D.2(b)] are Fourier transformed to (c) and (d) (Fourier spectra). The Fourier spectra are extracted within interested region to (e) and (f) (Fourier spectra extracted). (g) and (h) are inverse Fourier transformed interferograms. Fig. D.3 is the resultant phase shift image.

"AbelInversion.m"

The next step is to perform Abel inversion based on Eq. D.7. The code, "AbelInversion.m", including its user's manual is listed below. Note that, in the parameter file, the central axis has to be defined by giving left and right row number. Once the axis is determined, the calculation will return radial phase shift, $\phi(r)$ ("dPdx" in the code).

```
% AbelInversion_v5
%
%    Syntax: AbelInversion(FigureSwitch, PhaseShiftFilename, ParameterFilename)
%
%    FigureSwitch = 1: figure on
%    FigureSwitch = 0: figure off
```

```
%
%    parameter file:
%       LeftCenter_RowIndex
%       RightCenter_RowIndex
%       ZeroRange_RowIndex
%       pixel (length calibration, unit: m)
%
%    output files:
%       (1) xxx_PhaseShift_Symmetrized.mat
%              Matlab binary file (.mat)
%              structure.PhaseShift_Symmetrized: 2-D matrix, symmetrized phase shift data (unit: r
%              structure.Position              : 1-D row vector, calibrated position (unit: micron
%       (2) xxx_PhaseShift_Symmetrized.bmp
%              symmetrized phase shift image, 8-bit BMP file.
%       (3) xxx_dPdx.mat
%              Matlab binary file (.mat)
%              structure.dPdx    : 2-D matrix, dPhase/dx (unit: rad/m)
%              structure.Position: 1-D row vector, calibrated position (unit: micrometer)
%       (4) xxx_dPdx.bmp
%              dPhase/dx image, 8-bit BMP file.
%
%    returned value:
%       dPhase/dx, 2-D matrix (unit: rad/m)
%
%    Example:
%       a = AbelInversion(1,'IF-1-01_PhaseShift.mat', 'IF-1-01_Abel-parameters.txt');
%
%

function result = AbelInversion_v5(FigureSwitch, PhaseShiftFilename, ParameterFilename)

% importation of the parameter file
fid = fopen(ParameterFilename,'r');
while feof(fid) == 0
   line = fgetl(fid);
   eval(line);
end
fclose(fid);
Center_RowIndex = round((LeftCenter_RowIndex + RightCenter_RowIndex)/2);

% Loading of the phase-shift file
Source       = load(PhaseShiftFilename);
PhaseShift_1 = Source.PhaseShift;
[RowNumber_1, ColumnNumber_1] = size(PhaseShift_1);

% Rotation of the phase shift image
angle        = (RightCenter_RowIndex - LeftCenter_RowIndex)/ColumnNumber_1 * 180 / pi;
PhaseShift_2 = imrotate(PhaseShift_1, angle, 'bicubic');  % rotated phase shift data
[RowNumber_2, ColumnNumber_2] = size(PhaseShift_2);

% Average of the upper-half part and the lower-half part (symmetrize the phase shift image)
RowNumber_2_half  = min(Center_RowIndex, RowNumber_2 - Center_RowIndex);
PhaseShift_2_up   = PhaseShift_2(Center_RowIndex - RowNumber_2_half + 1:Center_RowIndex,:);
PhaseShift_2_down = PhaseShift_2(Center_RowIndex + 1:Center_RowIndex + RowNumber_2_half,:);
PhaseShift_3      = (flipud(PhaseShift_2_up) + PhaseShift_2_down) / 2;
%PhaseShift_3      = flipud(PhaseShift_2_up);
```

```
%PhaseShift_3       = PhaseShift_2_down;
[RowNumber_3, ColumnNumber_3] = size(PhaseShift_3);

% Noise reducing (cutting the phase image in the supposed-to-be-zero region)
PhaseShift_4 = PhaseShift_3(1:ZeroRange_RowIndex,:);
[RowNumber_4, ColumnNumber_4] = size(PhaseShift_4);

% Solving dPhase/dx (dPdx) by Abel inversion
dPdx_half = Abel(PhaseShift_4) / pixel;      % dPdx unit: rad/m, pixel: length calibration

% Data exportation
PhaseShift_Symmetrized = [flipud(PhaseShift_4);PhaseShift_4];   % (unit: rad)
dPdx                   = [flipud(dPdx_half);dPdx_half];         % (unit: rad/m)
Position               = [1:ColumnNumber_4] * pixel * 10^6;     % (unit: micrometer)

result = dPdx;

temp = strtok(PhaseShiftFilename,'.');
OutputFilename_1 = strcat(temp,'_PhaseShift_Symmetrized.mat');
OutputFilename_2 = strcat(temp,'_PhaseShift_Symmetrized.bmp');
OutputFilename_3 = strcat(temp,'_dPdx.mat');
OutputFilename_4 = strcat(temp,'_dPdx.bmp');

save(OutputFilename_1,'PhaseShift_Symmetrized','Position');

max_PS = max(max(PhaseShift_Symmetrized));
min_PS = min(min(PhaseShift_Symmetrized));
PhaseShift_image = (PhaseShift_Symmetrized - min_PS)./(max_PS - min_PS)*255;
imwrite(PhaseShift_image,jet(256),OutputFilename_2,'bmp');

save(OutputFilename_3,'dPdx','Position');

max_dPdx = max(max(dPdx));
min_dPdx = min(min(dPdx));
dPdx_image = (dPdx - min_dPdx)./(max_dPdx - min_dPdx)*255;
imwrite(dPdx_image,jet(256),OutputFilename_4,'bmp');



if FigureSwitch
    x = [1:RowNumber_2]';
    y1 = PhaseShift_2(:,round(ColumnNumber_2/4));
    y2 = PhaseShift_2(:,round(ColumnNumber_2/4*2));
    y3 = PhaseShift_2(:,round(ColumnNumber_2/4*3));
    y_max = max([y1;y2;y3])+(max([y1;y2;y3])-min([y1;y2;y3]))/5;
    y_min = min([y1;y2;y3])-(max([y1;y2;y3])-min([y1;y2;y3]))/5;
    x_c = [Center_RowIndex, Center_RowIndex];
    y_c = [y_min,y_max];

    subplot(3,2,1), imagesc(PhaseShift_1), title('original phase shift');
    PhaseShift_2_image = PhaseShift_2;
    PhaseShift_2_image(Center_RowIndex:Center_RowIndex + 1,:) = min(min(PhaseShift_2));
    subplot(3,2,3), imagesc(PhaseShift_2_image),  title('rotated phase shift');
    subplot(3,2,5), plot(x,y1,x,y2,x,y3,x_c,y_c), title('vertical line profile'),
    axis([-inf, inf, y_min, y_max]), xlabel('(pixel)'), ylabel('(rad)');
```

```
    PhaseShift_3_image = PhaseShift_3;
    PhaseShift_3_image(ZeroRange_RowIndex,:) = min(min(PhaseShift_3));
    subplot(3,2,2), imagesc(PhaseShift_3_image),  title('symmetrized phase shift');
    subplot(3,2,4), plot(PhaseShift_3(ZeroRange_RowIndex,:)), xlabel('(pixel)'), ylabel('(rad)'),
    title(['horizontal profile, row ' num2str(ZeroRange_RowIndex)]),;
    subplot(3,2,6), imagesc(PhaseShift_4),        title('noise cutted phase shift');

    figure;
    subplot(3,1,1), imagesc(PhaseShift_Symmetrized), title('symmetrized phase shift');
    subplot(3,1,2), imagesc(dPdx),                   title('dPhase/dx');
    subplot(3,1,3), contour(flipud(dPdx),15),        title('dPhase/dx');
end


%-------------------------------------------------------------------------------
%  Abel inversion
%-------------------------------------------------------------------------------

function result = Abel(PhaseShift)

[RowNumber, ColumnNumber] = size(PhaseShift);
r  = [1:RowNumber]';
rr = cumsum(ones(RowNumber));
yy = rr';
%     1          1          1 1 1...1          1 2 3...N
%     2          2          2 2 2...2          1 2 3...N
% r = 3,    y = 3,    rr = 3 3 3...3,    yy = 1 2 3...N
%     :          :          :                  :
%     N          N          N N N...N          1 2 3...N

% Abel inversion kernal:
%    A(i,j) = 1 / sqrt( y(j)^2 - r(i)^2 ) for j > i, A(i,j) = 0 for j <= i

A  = yy.^2 - rr.^2;   % set A(i,j) = y(j)^2 - r(i)^2
A  = A - (A == 0);    % set zero element to become -1, make 1./A possible
A  = 1 ./ A;          % set A(i,j) = 1 / ( y(j)^2 - r(i)^2 )
A  = A .* (A > 0);    % set A(i,j) = 0 for j <= i, keep other A(i,j)
A  = sqrt(A);         % set A(i,j) = 1 / sqrt( y(j)^2 - r(i)^2 )

% Abel inversion delta phase shift:
%    DeltaPS(j,k) = PhaseShift(j+1,k)-PhaseShift(j,k)

DeltaPS = zeros(RowNumber, ColumnNumber);
DeltaPS(1:RowNumber-1,:) = PhaseShift(2:RowNumber,:) - PhaseShift(1:RowNumber-1,:);

result = -1/pi*A*DeltaPS;
```

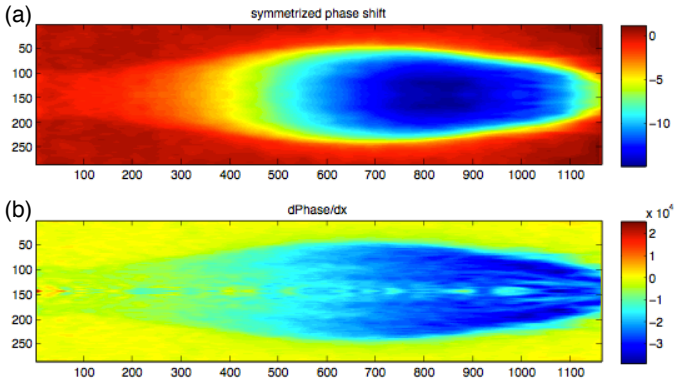

Figure D.4: The output images of "AbelInversion.m": (a)The symmetrized phase shift image. (b) "dPhase/dx" is the resultant radial phase shift information, $\phi(r)$, Abel-transformed from $d\phi/dx$ (Eq. D.7).

The output of "AbelInversion.m"

The output of "AbelInversion.m" is the radial phase shift information, $\phi(z, r)$ [Fig.D.4 (b)]. It is the result of Abel-transformation from symmetrized phase shift image shown in Fig.D.4 (a).

"'dPdx2ElectronDensity.m"

The final step is to calculate radial electron density, $n_e(r)$, based on Eq. D.7. The code "dPdx2ElectronDensity.m" is listed below and the output density profile is shown in Fig. D.5:

```
% a = dPdx2ElectronDensity(1,'IF-2-16_dPdx.mat', 'IF-2-16_Abel-parameters.txt');
% dPdx2ElectronDensity_v1
%
%    Convert the dPhase/dx data to be the electron density of an uniform plasma
%
%    Syntax: dPdx2n_e_plasma(FigureSwitch, dPdxFilename, ParameterFilename)
%
%    FigureSwitch = 1: figure on
%    FigureSwitch = 0: figure off
%
```

```
%    dPdx file:
%       dPhase/dx data, output file from the program 'AbelInversion.m' ( Matlab binary file )
%       structure.dPdx, 2-D matrix.
%
%    parameter file (shared with program 'AbelInversion.m')
%       wavelangth (unit: m)
%
%    output file:
%       Matlab binary file (.mat)
%       structure.ElectronDensity: 2-D matrix, electron density (unit: cm^-3)
%       structure.Position: 1-D row vector, calibrated position (unit: micrometer)
%    Example:
%       a = dPdx2ElectronDensity(1,'IF-1-01_dPdx.mat', 'IF-1-01-Abel_parameters.txt');
%
%
%

function result = dPdx2ElectronDensity_v1(FigureSwitch, dPdxFilename, ParameterFilename)
% region
rmin = 80; rmax =120; cmin =300; cmax = 800;
% Physical constants
   global c
   global epsilon_0
   global q_e
   global m_e
   c         = 2.9979 * 10^8;        % speed of light (m/sec)
   epsilon_0 = 8.8542 * 10^-12;      % permittivity of vacuum (F/m)
   q_e       = 1.6022 * 10^(-19);    % electron charge (Coul)
   m_e       = 9.1094 * 10^(-31);    % electron mass (kg)

% importation of the parameter file
fid = fopen(ParameterFilename,'r');
while feof(fid) == 0
   line = fgetl(fid);
   eval(line);
end
omega = 2*pi*c/wavelength;           % angular frequency of light (rad/sec)
k     = 2*pi/wavelength;             % wave number of light (rad/m)

% Loading of the dPhase/dx file
Source   = load(dPdxFilename);
dPdx     = 1 * Source.dPdx;         % dPhase/dx, (unit: rad/m)
Position = Source.Position;          % calibrated position (unit: micrometer)

% coefficient calculation
%    n_e = A*(B*dPdx+2)*dPdx
A = (epsilon_0 * m_e * omega^2) / (q_e^2 * k);   % (unit: m^-2)
B = 1/k;                                          % (unit: m)

% electron density n_e calculation
ElectronDensity =  A * (B*dPdx+2) .* dPdx / 10^6;  % (unit: cm^-3)

% Data exportation
result = ElectronDensity;
temp = strtok(dPdxFilename,'.');
OutputFilename = strcat(temp,'_ElectronDensity.mat');
```

```
save(OutputFilename,'ElectronDensity','Position');

if FigureSwitch
    figure;
     % imagesc(ElectronDensity);ztitle('electron density (cm^{-3})'),
     mesh(ElectronDensity), title(temp),
     xlabel('(pixel)'), ylabel('(pixel)'), zlabel('electron density (cm^{-3})');
     ElectronDensity= ElectronDensity(rmin:rmax, cmin:cmax);
     [R_center C_center] = find(ElectronDensity == max(max(ElectronDensity)));
      R_center = floor(mean(R_center));
      C_center = floor(mean(C_center));
      mean_density = mean(mean(ElectronDensity(R_center-3:R_center+3, C_center-10:C_center+10)))
end
```

The output of "dPdx2ElectronDensity.m"

The result is electron density profile on both radial and laser propagation direction, $n_e(z, r)$, shown in Fiq.D.5

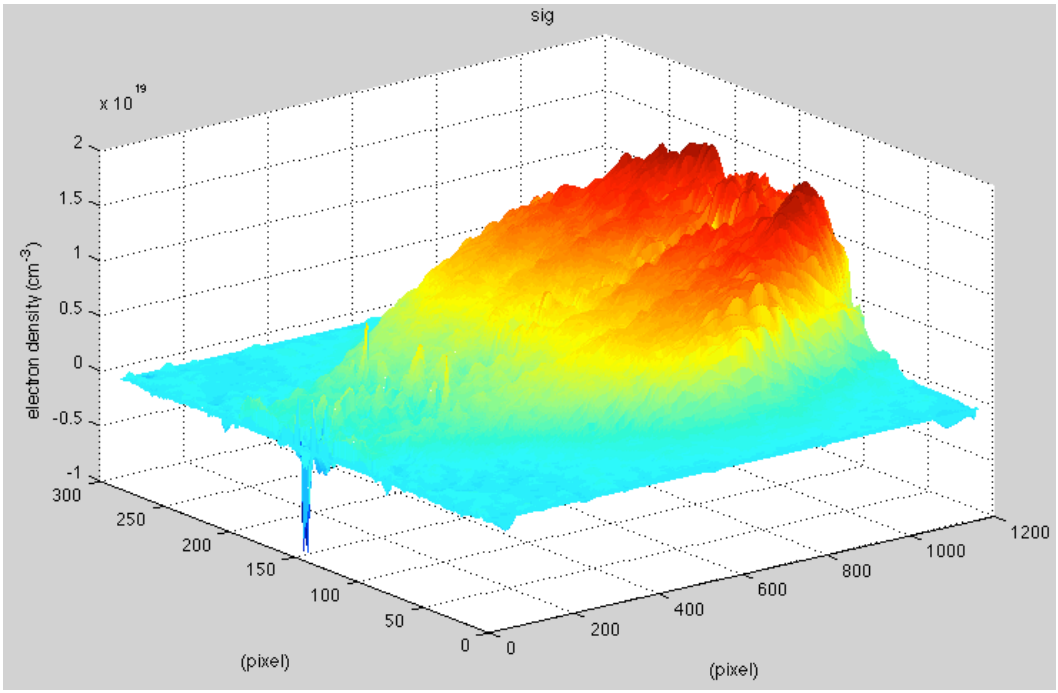

Figure D.5: The output images of "dPdx2ElectronDensity.m" shows the radial electron distribution.

Appendix E

The electron spectrometer: charge and energy analysis algorithm and code

E.1 Electron energy spectrum

The electron energy spectrum is determined by multiplying the vertically-integrated, magnetically-dispersed recorded electron trace dN_e/dx by the magnet dispersion dx/dE to generate an energy distribution dN_e/dE. The energy spread is then taking the ratio of the width E_{FWHM} of the quasi-monoenergetic peak to its central energy E_{peak}. Here N_e is electron number, E electron energy and x horizontal pixel distance along the phosphor screen.

"Espectrum.m"

The following Matlab code is to read magneticlly-dispersed electron profile recorded on the phosphor screen, perform vertical integration and return electron trace dN_c/dx, where N_c is integrated CCD counts, x is position in the unit of CCD pixel.

```
function result = Espectrum(Filename);
 source          = imread(Filename);
 background      =  source(1:50,1:50);
 background      =  mean(mean(background));
 source          = source - background;
 source          = source(300:700,1:700);  % choose the region of interest
```

```
 % find the peak indices
 [R_center C_center] = find(source == max(max(source)));
  R_center = floor( mean(R_center));
  C_center = floor( mean(C_center));

% Horizontal distribution
   H_y = sum(source(1:199,:));
   H_size = max(size(H_y));
   H_x = linspace(1,H_size,H_size)';
   yValue = H_y';
   yValue = double(yValue);
    xValue = H_x';
    xValue = double(xValue);

    % find peak index
      peak = find(yValue == max(yValue));
      peak = floor (mean(peak));
      x_center = xValue(peak)
     %yMax = max(yValue);
     % find x, y  size
      xsize = size(xValue);
      x_range = xsize(2);
      x_max = max(xValue);
      xint = floor(x_max);

    % plot
      xgrid = linspace(0, xint ,xint);
       subplot(2,1,1),imagesc(source);
       subplot(2,1,2), plot(xValue, yValue);

    % data expo

     temp = strtok(Filename,'.');
     OutputFilename1 = strcat(temp,'-sumlineout.txt');
     fid = fopen(OutputFilename1,'w');

     fprintf(fid,' %f\n', H_y);

    OutputImageName = strcat(temp,'_image.bmp');
    source = double(source);
    MaxValue = max(max(source));
    MinValue = min(min(source));
    OutputImage = (source - MinValue)/(MaxValue - MinValue)*255;
    colormap(gray(256));
    colormap(jet);
    imwrite(OutputImage,colormap,OutputImageName,'bmp');
```

The output of "Espectrum.m"

Fig. E.1 is the result of vertically integrated electron trace. The vertical axis is CCD counts, while the horizontal axis is CCD pixel.

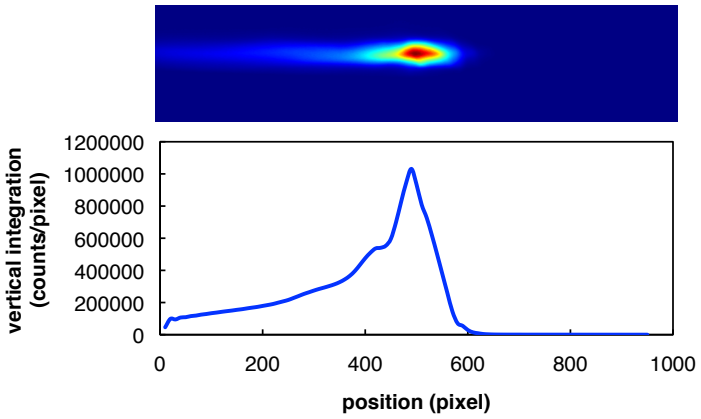

Figure E.1: The output of "Espectrum.m"

Magnet dispersion, dx/dE

The electron deflection position on phosphor screen is a function of electron energy. The function can be written as

$$D = A1+A2 = L\tan(\theta)+R-\sqrt{R^2-T^2} = L\frac{T}{\sqrt{R^2-T^2}}+R-\sqrt{R^2-T^2} \quad \text{(E.1)}$$

The schematic of electron spectrometer is shown in Fig. E.2(a), where T is the length of magnet, L the distance between magnet and phosphor screen, θ deflecting angle, R gyroradius

$$R = \frac{\gamma mv}{qB} = \frac{\gamma mc^2 v}{c^2 qB} \cong \frac{E}{cqB} \quad \text{(E.2)}$$

E is electron energy, B magnetic field, q electron charge. The position-energy function, $D(E)$, can be obtained by combining Eq. E.1 and Eq. E.2. $D(E)$ can translate to the pixel-energy function, $x(E)$, by using the spectrometer calibration value (unit: distance/pixel) as shown in Fig. E.2 (b). The above

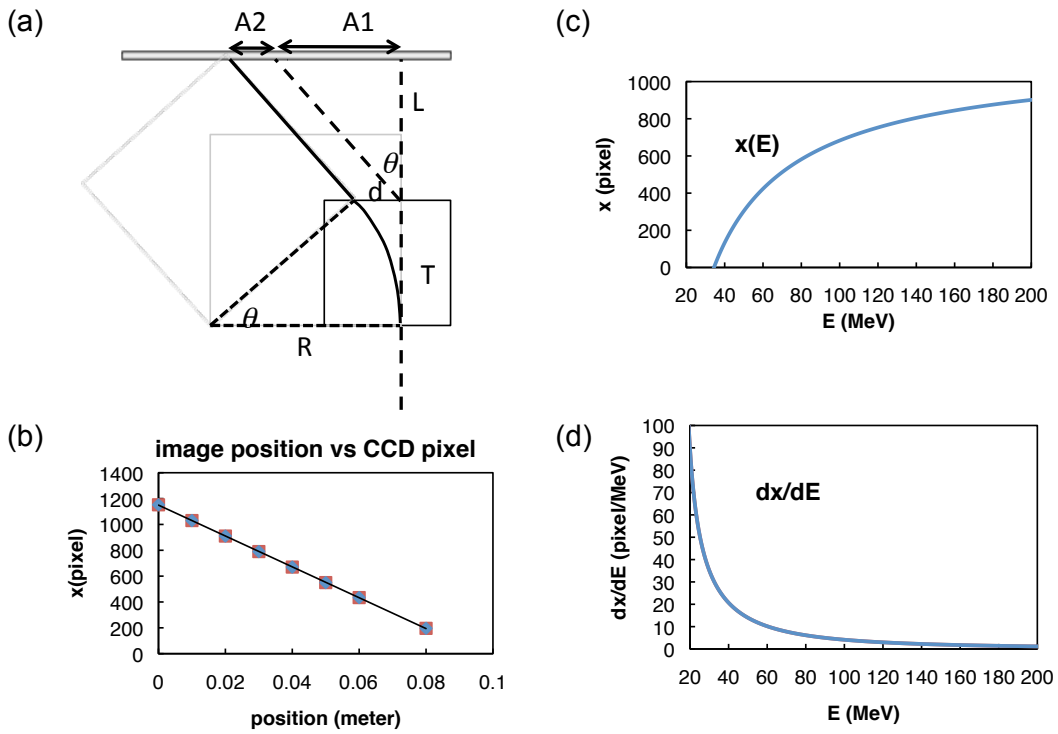

Figure E.2: (a) The schematic of electron spectrometer. (b) Spectrometer calibration: distance/pixel. (c)

described function, $D(E)$ and $x(E)$ [Fig. E.2 (c)], can be obtained on the Excel spread sheet. The magnetic dispersion , dx/dE[Fig. E.2 (d)], can also be obtained from $x(E)$ using simple algebra.

E.2 Electron charge

Charge was determined from integrated fluorescent photon number emitted from the phosphor screen using published calibrations for PI200 [110], taking account of the collecting angle of imaging optics, CCD quantum effi-

ciency, transmission of neutral density filters and color filters. The Matlab code to calculate the total charge number is listed as follow:

```
function result = EchargeCount(Filename);

range = 200 ;
calibration = 12*10^9; %PI-200; LANEX = 7*10^9
a = 1.7/40; % angle
sr = 2*pi*(1-cos(a))/(4*pi);
qe = 0.6; % CCD quantum efficiency
nd = 0.32;% filter attenuation nd 0.5 = 32%; nd 0.3 = 50%
 source           = imread(Filename);
% source           = source(200:800,580:1180);
background        = source(10:30,1200:1300);
background       =  mean(mean(background));
%background       = zeros(size(source));
%background(:,1) = mean(source(:,5:200)')';
%background       = cumsum(background')';
source           = source - background;
source           = source(400:600, 1:800);
source  = medfilt2(source, [4 4 ]);
   Master
  % find the peak indices
  [R_center C_center] = find(source == max(max(source)));
   R_center = floor( mean(R_center));
   C_center = floor( mean(C_center));

   % Sum
   R_up = R_center - range;
   R_dn = R_center + range;
   C_left = C_center - 4*range;
   C_right = C_center + 2*range;
   % source = source(R_up:R_dn, C_left:C_right);

   total_sum = sum(sum(source));
   imagesc(source);
   result = total_sum/sr/calibration/qe/nd
   %result = ? pc
```

Appendix F

Hard X-ray photon and energy analysis

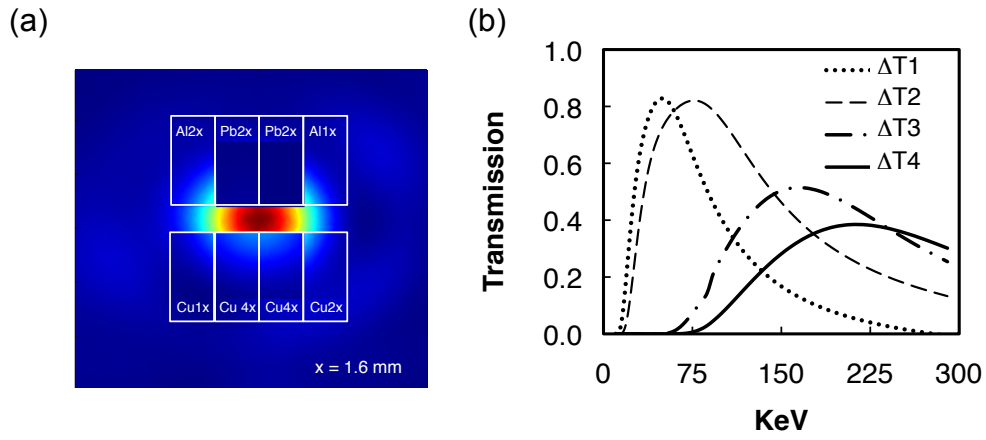

Figure F.1: (a) The simulated x-ray beam profile after absorption through a set of 4 filter pairs. (b) The differential transmission spectra $\Delta T1 - \Delta T4$, of these filter pairs provide 4 energy band pass filters peaked at 50, 80,150, 200KeV.

We measure the spatially averaged x-ray spectra by comparing transmission through a set of 4 filter pairs. Filters are aligned horizontally on upper and lower half of the beam. Fig. F.1 (a) is calculated profile after filters absorption for 150 kev x-ray beam. The differential transmission spectra, $\Delta T1 - \Delta T4$ shown in ig. F.1 (b), of these filter pairs provide 4 energy band pass filters peaked at 50, 80,150,200KeV. So the difference of transmitted signal through each pairs along with IP response curve R was used to determine the photon

number with energies within the filter pairs transmission band (ΔE), written explicitly as

$$\Delta S = \int^{E_i} x_i(E) R_i(E) \Delta T dE \tag{F.1}$$

where i = 1,2,3,4 and E is photon energy, R is the detector response, and S and T are the signal level and transmittance of individual filters, respectively. Assuming the X-ray photon density has a nearly linear slope within each filter pair bandwidth, the photon density can be written as

$$x(E) = x^{ave}[1 + \beta(E - E^{ave})/\Delta E] \tag{F.2}$$

where E^{avg} is the average energy within the bandwidth and β is the slope of the distribution within the bandwidth. The average photon density,

$$x^{ave}(E) = \frac{\Delta S}{\int [1 + \beta(E - E^{ave})/\Delta E] R(E) \Delta T(E) dE} \tag{F.3}$$

is obtained by integrating across the filter-pair bandwidth. We used $\beta = 0$ to calculate the X-ray photon density, but included uncertainty in the slope in the error analysis as

$$\sigma_\beta = \frac{|x^{ave}_{\beta=\beta_{max}} - x^{ave}_{\beta=-\beta_{max}}|}{x^{ave}_{\beta=0}} \tag{F.4}$$

The upper limit of the slope (β_{max}= 4) was estimated from simulations. Other factors contributing to error bars include uncertainty in the filter filter thickness, crosstalk between voxels, and filter bandgap leakage.

Appendix G

Publications by the author while at University of Texas

1. P. Dong, Hai-En Tsai, A. Yi, G. Shvets, M. C. Downer, M. S. Kalmykov, N. H. Matlis, C. McGuffey, S. Bulanov, V. Chvykov, G. Kalintchenko, K. Krushelnick, A. Maksimchuk, T. Matsuoka, A. G. R. Thomas, V. Yanovsky, "Dynamics of nonlinear laser-plasma accelerators (LPA) probed by frequency-domain holography (FDH)." *AIP. Conf. Proc.* **1**, 7008 (2010).

2. Xiaoming Wang, Rafal Zgadzaj, S. A. Yi, V. Khudik, W. Henderson, N. Fazel, Y-Y Chang, R. Korzekwa, H-E Tsai, C-H Pai, and M.C. Downer, "Self-injected petawatt laser-driven plasma electron acceleration in 10^{17} cm^{-3} plasma," *Journal of Plasma Physics*, **78**, 04 (2012).

3. Hai-En Tsai, Chih-Hao Pai, and M. C. Downer, "Global optimization of quasi-monoenergetic electron beams from laser wakefield accelerators," *AIP. Conf. Proc.* **1**, 1507 (2012).

4. X. Wang, R. Zgadzaj, N. Fazel, Z. Li, S. A. Yi, X. Zhang, W. Henderson, Y.-Y. Chang, R. Korzekwa, H.-E. Tsai, C.-H. Pai, H. Quevedo, G.

Dyer, E. Gaul, M. Martinez, A. C. Bernstein, T. Borger, M. Spinks, M. Donovan, V. Khudik, G. Shvets, T. Ditmire and M. C. Downer, "Quasi-monoenergetic laser-plasma acceleration of electrons to 2 GeV," *Nature Communications* **4**, 1988 (2013).

5. Zhengyan Li, Hai-En Tsai, Xi Zhang, Chih-Hao Pai, R. Zgadzaj, X. Wang, V. Khudik, G. Shvets, and M. C. Downer, "Single-shot visualization of evolving laser wakefields using an all-optical streak camera," *Phys. Rev. Lett.* **113**, 085001 (2014).

6. Hai-En Tsai, Xiaoming Wang, Joseph M. Shaw, Zhengyan Li, Alexey V. Arefiev, Xi Zhang, Rafal Zgadzaj, Watson Henderson, V. Khudik, G. Shvets, and M. C. Downer, "Compact tunable Compton x-ray source from laser-plasma accelerator and plasma mirror," *Phys. Plasmas* **22**, 023106 (2015).

7. Hai-En Tsai, Xiaoming Wang, Joseph M. Shaw, Zhengyan Li, Alexey V. Arefiev, Xi Zhang, Rafal Zgadzaj, Watson Henderson, V. Khudik, G. Shvets, and M. C. Downer, "Spatial and temporal characterization of a plasma mirror at relativistic intensity," submitted to *New Journal of Physics*

Bibliography

[1] http://flash.desy.de/.

[2] K. Adumi, K. A. Tanaka, T. Matsuoka, T. Kurahashi, T. Yabuuchi, Y. Kitagawa, R. Kodama, K. Sawai, K. Suzuki, K. Okabe, T. Sera, T. Norimatsu, and Y. Izawa. Characterization of preplasma produced by an ultrahigh intensity laser system. *Physics of Plasmas (1994-present)*, 11(8), 2004.

[3] Gideon Alexander, John Barley, Yuri Batygin, Steven Berridge, Vinod Bharadwaj, Gary Bower, William Bugg, F-J Decker, Ralph Dollan, Yuri Efremenko, et al. Undulator-based production of polarized positrons. *Nuclear Instruments and Methods in Physics Research Section A: Accelerators, Spectrometers, Detectors and Associated Equipment*, 610(2):451–487, 2009.

[4] Alexey V. Arefiev, Vladimir N. Khudik, and Marius Schollmeier. Enhancement of laser-driven electron acceleration in an ion channel. *Phys. Plasmas*, 21(3):033104, 2014.

[5] Sterling Backus, Charles G Durfee III, Margaret M Murnane, and Henry C Kapteyn. High power ultrafast lasers. *Review of scientific instruments*, 69(3):1207–1223, 1998.

[6] Sterling Backus, David M Gold, Howard Nathel, Henry C Kapteyn, Margaret M Murnane, and William White. Prepulse suppression for high-energy ultrashort pulses using self-induced plasma shuttering from a fluid target. *Optics letters*, 18(2):134–136, 1993.

[7] Thomas R. M. Barends, Lutz Foucar, Sabine Botha, R. Bruce Doak, Robert L. Shoeman, Karol Nass, Jason E. Koglin, Garth J. Williams, Sebastien Boutet, Marc Messerschmidt, and Ilme Schlichting. De novo protein crystal structure determination from x-ray free-electron laser data. *Nature*, 505(7482):244–247, 01 2014.

[8] Mark Birkinshaw. The sunyaev–zeldovich effect. *Physics Reports*, 310(2):97–195, 1999.

[9] Antonin Borot, Arnaud Malvache, Xiaowei Chen, Denis Douillet, Grégory Iaquianiello, Thierry Lefrou, Patrick Audebert, Jean-Paul Geindre, Gérard Mourou, Fabien Quéré, et al. High-harmonic generation from plasma mirrors at kilohertz repetition rate. *Optics letters*, 36(8):1461–1463, 2011.

[10] F. Brunel. Not-so-resonant, resonant absorption. *Phys. Rev. Lett.*, 59:52–55, Jul 1987.

[11] P Catravas, E Esarey, and W P Leemans. Femtosecond x-rays from thomson scattering using laser wakefield accelerators. *Meas. Sci. Technol.*, 12(11):1828, 2001.

[12] P. Catravas, E. Esarey, and W. P. Leemans. Radiation sources and diagnostics with ultrashort electron bunches. *Physics of Plasmas (1994-present)*, 9(5), 2002.

[13] S. Chen, N. D. Powers, I. Ghebregziabher, C. M. Maharjan, C. Liu, G. Golovin, S. Banerjee, J. Zhang, N. Cunningham, A. Moorti, S. Clarke, S. Pozzi, and D. P. Umstadter. Mev-energy x rays from inverse compton scattering with laser-wakefield accelerated electrons. *Phys. Rev. Lett.*, 110:155003, Apr 2013.

[14] S.-Y. Chen, M. Krishnan, A. Maksimchuk, R. Wagner, and D. Umstadter. Detailed dynamics of electron beams self-trapped and accelerated in a self-modulated laser wakefield. *Physics of Plasmas (1994-present)*, 6(12), 1999.

[15] Szu-yuan Chen, Anatoly Maksimchuk, and Donald Umstadter. Experimental observation of relativistic nonlinear thomson scattering. *Nature*, 396(6712):653–655, 1998.

[16] Extendable PIC Open Collaboration. *http://ccpforge.cse.rl.ac.uk/gf/project/epoch.*

[17] S. Corde, K. Ta Phuoc, G. Lambert, R. Fitour, V. Malka, A. Rousse, A. Beck, and E. Lefebvre. Femtosecond x rays from laser-plasma accelerators. *Rev. Mod. Phys.*, 85:1–48, Jan 2013.

[18] P. B. Corkum. Plasma perspective on strong field multiphoton ionization. *Phys. Rev. Lett.*, 71:1994–1997, Sep 1993.

[19] CD Decker, WB Mori, K-C Tzeng, and T Katsouleas. The evolution of ultra-intense, short-pulse lasers in underdense plasmas. *Physics of Plasmas (1994-present)*, 3(5):2047–2056, 1996.

[20] Moshe Deutsch and Israel Beniaminy. Derivativefree inversion of abels integral equation. *Applied Physics Letters*, 41(1), 1982.

[21] K Dobashi, T Hirose, T Kumita, Y Kurihara, T Muto, T Omori, T Okugi, K Sugiyama, and J Urakawa. Generation of positrons via pair-creation from compton scattered gamma-rays. *Nuclear Instruments and Methods in Physics Research Section A: Accelerators, Spectrometers, Detectors and Associated Equipment*, 437(2):169–177, 1999.

[22] Peng Dong, S. A. Reed, S. A. Yi, S. Kalmykov, G. Shvets, M. C. Downer, N. H. Matlis, W. P. Leemans, C. McGuffey, S. S. Bulanov, V. Chvykov, G. Kalintchenko, K. Krushelnick, A. Maksimchuk, T. Matsuoka, A. G. R. Thomas, and V. Yanovsky. Formation of optical bullets in laser-driven plasma bubble accelerators. *Phys. Rev. Lett.*, 104:134801, Mar 2010.

[23] G. Doumy, F. Quéré, O. Gobert, M. Perdrix, Ph. Martin, P. Audebert, J. C. Gauthier, J.-P. Geindre, and T. Wittmann. Complete characterization of a plasma mirror for the production of high-contrast ultraintense laser pulses. *Phys. Rev. E*, 69:026402, Feb 2004.

[24] B. Dromey, D. Adams, R. Horlein, Y. Nomura, S. G. Rykovanov, D. C. Carroll, P. S. Foster, S. Kar, K. Markey, P. McKenna, D. Neely, M. Geissler,

G. D. Tsakiris, and M. Zepf. Diffraction-limited performance and focusing of high harmonics from relativistic plasmas. *Nat Phys*, 5(2):146–152, 02 2009.

[25] NA Ebrahim, P Lavigne, and S Aithal. Experiments on the plasma beat-wave accelerator. *Nuclear Science, IEEE Transactions on*, 32(5):3539–3541, 1985.

[26] E. Esarey, C. B. Schroeder, and W. P. Leemans. Physics of laser-driven plasma-based electron accelerators. *Rev. Mod. Phys.*, 81:1229–1285, Aug 2009.

[27] E. Esarey, C. B. Schroeder, and W. P. Leemans. Physics of laser-driven plasma-based electron accelerators. *Rev. Mod. Phys.*, 81:1229–1285, Aug 2009.

[28] E. Esarey and A. Ting. Comment on "cascade focusing in the beat-wave accelerator". *Phys. Rev. Lett.*, 65:1961–1961, Oct 1990.

[29] Eric Esarey, Sally K Ride, and Phillip Sprangle. Nonlinear thomson scattering of intense laser pulses from beams and plasmas. *Physical Review E*, 48(4):3003, 1993.

[30] J. Faure, Y. Glinec, A. Pukhov, S. Kiselev, S. Gordienko, E. Lefebvre, J. P. Rousseau, F. Burgy, and V. Malka. A laser-plasma accelerator producing monoenergetic electron beams. *Nature (London)*, 431(7008):541–544, 09 2004.

[31] Jérôme Faure, Clément Rechatin, A Norlin, A Lifschitz, Y Glinec, and Victor Malka. Controlled injection and acceleration of electrons in plasma wakefields by colliding laser pulses. *Nature*, 444(7120):737–739, 2006.

[32] Gadi Fibich and Alexander L. Gaeta. Critical power for self-focusing in bulk media and in hollow waveguides. *Opt. Lett.*, 25(5):335–337, Mar 2000.

[33] D. H. Froula, C. E. Clayton, T. Döppner, K. A. Marsh, C. P. J. Barty, L. Divol, R. A. Fonseca, S. H. Glenzer, C. Joshi, W. Lu, S. F. Martins, P. Michel, W. B. Mori, J. P. Palastro, B. B. Pollock, A. Pak, J. E. Ralph, J. S. Ross, C. W. Siders, L. O. Silva, and T. Wang. Measurements of the critical power for self-injection of electrons in a laser wakefield accelerator. *Phys. Rev. Lett.*, 103:215006, Nov 2009.

[34] C. G. R. Geddes, K. Nakamura, G. R. Plateau, Cs. Toth, E. Cormier-Michel, E. Esarey, C. B. Schroeder, J. R. Cary, and W. P. Leemans. Plasma-density-gradient injection of low absolute-momentum-spread electron bunches. *Phys. Rev. Lett.*, 100:215004, May 2008.

[35] C. G. R. Geddes, Cs. Toth, J. van Tilborg, E. Esarey, C. B. Schroeder, D. Bruhwiler, C. Nieter, J. Cary, and W. P. Leemans. High-quality electron beams from a laser wakefield accelerator using plasma-channel guiding. *Nature (London)*, 431(7008):538–541, 09 2004.

[36] Matthias Geissel, Marius S. Schollmeier, Mark W. Kimmel, Patrick K. Rambo, Jens Schwarz, Briggs W. Atherton, and Erik Brambrink. Characterizing plasma mirrors near breakdown. *Rev. Sci. Instrum.*, 82(5):–, 2011.

[37] David J. Gibson, Scott G. Anderson, Christopher P. J. Barty, Shawn M. Betts, Rex Booth, Winthrop J. Brown, John K. Crane, Robert R. Cross, David N. Fittinghoff, Fred V. Hartemann, Jaroslav Kuba, Gregory P. Le Sage, Dennis R. Slaughter, Aaron M. Tremaine, Alan J. Wootton, Edward P. Hartouni, Paul T. Springer, and James B. Rosenzweig. Pleiades: A picosecond compton scattering x-ray source for advanced backlighting and time-resolved material studies. *Phys. Plasmas*, 11(5):2857–2864, 2004.

[38] B Girolami, B Larsson, M Preger, C Schaerf, and J Stepanek. Photon beams for radiosurgery produced by laser compton backscattering from relativistic electrons. *Phys. Med. Biol.*, 41(9):1581, 1996.

[39] Y. Glinec, J. Faure, L. Le Dain, S. Darbon, T. Hosokai, J. J. Santos, E. Lefebvre, J. P. Rousseau, F. Burgy, B. Mercier, and V. Malka. High-resolution γ-ray radiography produced by a laser-plasma driven electron source. *Phys. Rev. Lett.*, 94:025003, Jan 2005.

[40] DM Gold. Direct measurement of prepulse suppression by use of a plasma shutter. *Optics letters*, 19(23):2006–2008, 1994.

[41] LM Gorbunov and VI Kirsanov. Excitation of plasma waves by an electromagnetic wave packet. *Sov. Phys. JETP*, 66(290-294):40, 1987.

[42] D. Gordon, K. C. Tzeng, C. E. Clayton, A. E. Dangor, V. Malka, K. A. Marsh, A. Modena, W. B. Mori, P. Muggli, Z. Najmudin, D. Neely, C. Danson, and C. Joshi. Observation of electron energies beyond the linear dephasing limit from a laser-excited relativistic plasma wave. *Phys. Rev. Lett.*, 80:2133–2136, Mar 1998.

[43] M. K. Grimes, A. R. Rundquist, Y.-S. Lee, and M. C. Downer. Experimental identification of "vacuum heating" at femtosecond-laser-irradiated metal surfaces. *Phys. Rev. Lett.*, 82:4010–4013, May 1999.

[44] Nasr A. M. Hafz, Tae Moon Jeong, Il Woo Choi, Seong Ku Lee, Ki Hong Pae, Victor V. Kulagin, Jae Hee Sung, Tae Jun Yu, Kyung-Han Hong, Tomonao Hosokai, John R. Cary, Do-Kyeong Ko, and Jongmin Lee. Stable generation of gev-class electron beams from self-guided laser-plasma channels. *Nat. Photon.*, 2(9):571–577, 09 2008.

[45] F. V. Hartemann, D. J. Gibson, W. J. Brown, A. Rousse, K. Ta Phuoc, V. Mallka, J. Faure, and A. Pukhov. Compton scattering x-ray sources driven by laser wakefield acceleration. *Phys. Rev. ST Accel. Beams*, 10:011301, Jan 2007.

[46] Andreas Henig, Daniel Kiefer, K Markey, DC Gautier, KA Flippo, S Letzring, RP Johnson, T Shimada, L Yin, BJ Albright, et al. Enhanced

laser-driven ion acceleration in the relativistic transparency regime. *Physical review letters*, 103(4):045002, 2009.

[47] Tomasz Jannson, Michael Gertsenshteyn, Victor Grubsky, Pauline Amouzou, and Richard Koziol. In *Defense and Security Symposium*, page 65380A. International Society for Optics and Photonics, 2007.

[48] C Joshi, T Tajima, JM Dawson, HA Baldis, and NA Ebrahim. Forward raman instability and electron acceleration. *Physical Review Letters*, 47(18):1285, 1981.

[49] S. Kalmykov, S. A. Yi, V. Khudik, and G. Shvets. Electron self-injection and trapping into an evolving plasma bubble. *Phys. Rev. Lett.*, 103:135004, Sep 2009.

[50] Henry C. Kapteyn, Abraham Szoke, Roger W. Falcone, and Margaret M. Murnane. Prepulse energy suppression for high-energy ultrashort pulses using self-induced plasma shuttering. *Opt. Lett.*, 16(7):490–492, Apr 1991.

[51] Richard A. Ketcham and William D. Carlson. Acquisition, optimization and interpretation of x-ray computed tomographic imagery: Applications to the geosciences. *Comput. Geosci.*, 27(4):381–400, May 2001.

[52] Hyung Taek Kim, Ki Hong Pae, Hyuk Jin Cha, I Jong Kim, Tae Jun Yu, Jae Hee Sung, Seong Ku Lee, Tae Moon Jeong, and Jongmin Lee.

Enhancement of electron energy to the multi-gev regime by a dual-stage laser-wakefield accelerator pumped by petawatt laser pulses. *Phys. Rev. Lett.*, 111:165002, Oct 2013.

[53] S Kneip, C McGuffey, JL Martins, SF Martins, C Bellei, V Chvykov, F Dollar, R Fonseca, C Huntington, G Kalintchenko, et al. Bright spatially coherent synchrotron x-rays from a table-top source. *Nature Physics*, 7(9):737–737, 2011.

[54] S. Kneip, S. R. Nagel, S. F. Martins, S. P. D. Mangles, C. Bellei, O. Chekhlov, R. J. Clarke, N. Delerue, E. J. Divall, G. Doucas, K. Ertel, F. Fiuza, R. Fonseca, P. Foster, S. J. Hawkes, C. J. Hooker, K. Krushelnick, W. B. Mori, C. A. J. Palmer, K. Ta Phuoc, P. P. Rajeev, J. Schreiber, M. J. V. Streeter, D. Urner, J. Vieira, L. O. Silva, and Z. Najmudin. Near-gev acceleration of electrons by a nonlinear plasma wave driven by a self-guided laser pulse. *Phys. Rev. Lett.*, 103:035002, Jul 2009.

[55] Artem V Korzhimanov, A A Gonoskov, Efim A Khazanov, and Aleksandr M Sergeev. Horizons of petawatt laser technology. *Physics-Uspekhi*, 54(1):9, 2011.

[56] W.L. Kruer. *The physics of laser plasma interactions*. Jan 1988.

[57] E. Kwan, G. Rusev, A. S. Adekola, F. Dönau, S. L. Hammond, C. R. Howell, H. J. Karwowski, J. H. Kelley, R. S. Pedroni, R. Raut, A. P. Tonchev, and W. Tornow. Discrete deexcitations in ^{235}U below 3 mev

from nuclear resonance fluorescence. *Phys. Rev. C*, 83:041601, Apr 2011.

[58] H. Langhoff, B. T. Bowes, M. C. Downer, Bixue Hou, and J. A. Nees. Surface energy transport following relativistic laser-solid interaction. *Physics of Plasmas (1994-present)*, 16(7):–, 2009.

[59] S. P. Le Blanc, M. C. Downer, R. Wagner, S.-Y. Chen, A. Maksimchuk, G. Mourou, and D. Umstadter. Temporal characterization of a self-modulated laser wakefield. *Phys. Rev. Lett.*, 77:5381–5384, Dec 1996.

[60] W. P. Leemans, P. Catravas, E. Esarey, C. G. R. Geddes, C. Toth, R. Trines, C. B. Schroeder, B. A. Shadwick, J. van Tilborg, and J. Faure. Electron-yield enhancement in a laser-wakefield accelerator driven by asymmetric laser pulses. *Phys. Rev. Lett.*, 89:174802, Oct 2002.

[61] W. P. Leemans, A. J. Gonsalves, H.-S. Mao, K. Nakamura, C. Benedetti, C. B. Schroeder, Cs. Tóth, J. Daniels, D. E. Mittelberger, S. S. Bulanov, J.-L. Vay, C. G. R. Geddes, and E. Esarey. Multi-gev electron beams from capillary-discharge-guided subpetawatt laser pulses in the self-trapping regime. *Phys. Rev. Lett.*, 113:245002, Dec 2014.

[62] W. P. Leemans, B. Nagler, A. J. Gonsalves, Cs. Toth, K. Nakamura, C. G. R. Geddes, E. Esarey, C. B. Schroeder, and S. M. Hooker. Gev electron beams from a centimetre-scale accelerator. *Nat. Phys.*, 2(10):696–699, 10 2006.

[63] W. P. Leemans, D. Rodgers, P. E. Catravas, C. G. R. Geddes, G. Fubiani, E. Esarey, B. A. Shadwick, R. Donahue, and A. Smith. Gamma-neutron activation experiments using laser wakefield accelerators. *Physics of Plasmas (1994-present)*, 8(5), 2001.

[64] W. P. Leemans, R. W. Schoenlein, P. Volfbeyn, A. H. Chin, T. E. Glover, P. Balling, M. Zolotorev, K. J. Kim, S. Chattopadhyay, and C. V. Shank. X-ray based subpicosecond electron bunch characterization using 90degree thomson scattering. *Phys. Rev. Lett.*, 77:4182–4185, Nov 1996.

[65] Zhengyan Li, Hai-En Tsai, Xi Zhang, Chih-Hao Pai, Yen-Yu Chang, Rafal Zgadzaj, Xiaoming Wang, V. Khudik, G. Shvets, and M. C. Downer. Single-shot visualization of evolving laser wakefields using an all-optical streak camera. *Phys. Rev. Lett.*, 113:085001, Aug 2014.

[66] Wei Lu, M Tzoufras, C Joshi, FS Tsung, WB Mori, J Vieira, RA Fonseca, and LO Silva. Generating multi-gev electron bunches using single stage laser wakefield acceleration in a 3d nonlinear regime. *Physical Review Special Topics-Accelerators and Beams*, 10(6):061301, 2007.

[67] P Maine, D Strickland, P Bado, M Pessot, and G Mourou. Generation of ultrahigh peak power pulses by chirped pulse amplification. *Quantum electronics, IEEE Journal of*, 24(2):398–403, 1988.

[68] Victor Malka, J Faure, JR Marques, F Amiranoff, JP Rousseau, S Ranc, JP Chambaret, Z Najmudin, B Walton, P Mora, et al. Characterization

of electron beams produced by ultrashort (30 fs) laser pulses. *Physics of Plasmas (1994-present)*, 8(6):2605–2608, 2001.

[69] Victor Malka, S Fritzler, E Lefebvre, M-M Aleonard, F Burgy, J-P Chambaret, J-F Chemin, K Krushelnick, G Malka, SPD Mangles, et al. Electron acceleration by a wake field forced by an intense ultrashort laser pulse. *Science*, 298(5598):1596–1600, 2002.

[70] S. P. D. Mangles, C. D. Murphy, Z. Najmudin, A. G. R. Thomas, J. L. Collier, A. E. Dangor, E. J. Divall, P. S. Foster, J. G. Gallacher, C. J. Hooker, D. A. Jaroszynski, A. J. Langley, W. B. Mori, P. A. Norreys, F. S. Tsung, R. Viskup, B. R. Walton, and K. Krushelnick. Monoenergetic beams of relativistic electrons from intense laser-plasma interactions. *Nature (London)*, 431(7008):535–538, 09 2004.

[71] C. McGuffey, A. G. R. Thomas, W. Schumaker, T. Matsuoka, V. Chvykov, F. J. Dollar, G. Kalintchenko, V. Yanovsky, A. Maksimchuk, K. Krushelnick, V. Yu. Bychenkov, I. V. Glazyrin, and A. V. Karpeev. Ionization induced trapping in a laser wakefield accelerator. *Phys. Rev. Lett.*, 104:025004, Jan 2010.

[72] AL Meadowcroft, CD Bentley, and EN Stott. *Rev. Sci. Instrum.*, 79(11):113102, 2008.

[73] A Modena, Z Najmudin, AE Dangor, CE Clayton, KA Marsh, C Joshi, V Malka, CB Darrow, C Danson, D Neely, et al. Electron acceleration from the breaking of relativistic plasma waves. 1995.

[74] G Mourou and D Umstadter. Development and applications of compact high-intensity lasers. *Physics of Fluids B: Plasma Physics (1989-1993)*, 4(7):2315–2325, 1992.

[75] Gerard A. Mourou, Toshiki Tajima, and Sergei V. Bulanov. Optics in the relativistic regime. *Rev. Mod. Phys.*, 78:309–371, Apr 2006.

[76] K. Nakajima, D. Fisher, T. Kawakubo, H. Nakanishi, A. Ogata, Y. Kato, Y. Kitagawa, R. Kodama, K. Mima, H. Shiraga, K. Suzuki, K. Yamakawa, T. Zhang, Y. Sakawa, T. Shoji, Y. Nishida, N. Yugami, M. Downer, and T. Tajima. Observation of ultrahigh gradient electron acceleration by a self-modulated intense short laser pulse. *Phys. Rev. Lett.*, 74:4428–4431, May 1995.

[77] Jeremiah P Ostriker and Ethan T Vishniac. Effect of gravitational lenses on the microwave background, and 1146+ 111b, c. *Nature*, 322:804, 1986.

[78] A. Pak, K. A. Marsh, S. F. Martins, W. Lu, W. B. Mori, and C. Joshi. Injection and trapping of tunnel-ionized electrons into laser-produced wakes. *Phys. Rev. Lett.*, 104:025003, Jan 2010.

[79] Sasi Palaniyappan, B Manuel Hegelich, Hui-Chun Wu, Daniel Jung, Donald C Gautier, Lin Yin, Brian J Albright, Randall P Johnson, Tsutomu Shimada, Samuel Letzring, et al. Dynamics of relativistic transparency and optical shuttering in expanding overdense plasmas. *Nature Physics*, 8(10):763–769, 2012.

[80] Michael D Perry and Gerard Mourou. Terawatt to petawatt subpicosecond lasers. *Science*, 264(5161):917–924, 1994.

[81] I.V Pogorelsky. Ultra-bright x-ray and γ sources by compton backscattering of {CO2} laser beams. *Nuclear Instruments and Methods in Physics Research Section A: Accelerators, Spectrometers, Detectors and Associated Equipment*, 411(1):172 – 187, 1998.

[82] N. D. Powers, I. Ghebregziabher, G. Golovin, C. Liu, S. Chen, S. Banerjee, J. Zhang, and D. P. Umstadter. Quasi-monoenergetic and tunable x-rays from a laser-driven compton light source. *Nat. Photon.*, 8(1):28–31, 01 2014.

[83] A. Pukhov and J. Meyer-ter Vehn. Laser wake field acceleration: the highly non-linear broken-wave regime. *Appl. Phys. B*, 74(4-5):355–361, 2002.

[84] Alexander Pukhov. Three-dimensional electromagnetic relativistic particle-in-cell code vlpl (virtual laser plasma lab). *Journal of Plasma Physics*, 61(03):425–433, 1999.

[85] C. P. Ridgers, C. S. Brady, R. Duclous, J. G. Kirk, K. Bennett, T. D. Arber, A. P. L. Robinson, and A. R. Bell. Dense electron-positron plasmas and ultraintense γ-rays from laser-irradiated solids. *Phys. Rev. Lett.*, 108:165006, Apr 2012.

[86] Christian Rischel, Antoine Rousse, Ingo Uschmann, Pierre-Antoine Albouy, Jean-Paul Geindre, Patrick Audebert, Jean-Claude Gauthier, Eckhart Froster, Jean-Louis Martin, and Andre Antonetti. Femtosecond time-resolved x-ray diffraction from laser-heated organic films. *Nature (London)*, 390(6659):490–492, 12 1997.

[87] A. Rousse, P. Audebert, J. P. Geindre, F. Falliès, J. C. Gauthier, A. Mysyrowicz, G. Grillon, and A. Antonetti. Efficient K α x-ray source from femtosecond laser-produced plasmas. *Phys. Rev. E*, 50:2200–2207, Sep 1994.

[88] G. Sarri, J. Corvan, D. W. Schumaker, M. Cole, J. A. Di Piazza, H. Ahmed, C. Harvey, H. Keitel, C. K. Krushelnick, P.D̃. Mangles, S. Z. Najmudin, D. Symes, G.R̃. Thomas, A. M. Yeung, Z. Zhao, and M. Zepf. Ultrahigh brilliance multi-mev γ-ray beams from nonlinear relativistic thomson scattering. *Phys. Rev. Lett.*, 113:224801, Nov 2014.

[89] R. W. Schoenlein, W. P. Leemans, A. H. Chin, P. Volfbeyn, T. E. Glover, P. Balling, M. Zolotorev, K.-J. Kim, S. Chattopadhyay, and C. V. Shank. Femtosecond x-ray pulses at 0.4 angstrom generated by 90 degree thomson scattering: A tool for probing the structural dynamics of materials. *Science*, 274(5285):236–238, 1996.

[90] E. C. Schreiber, R. S. Canon, B. T. Crowley, C. R. Howell, J. H. Kelley, V. N. Litvinenko, S. O. Nelson, S. H. Park, I. V. Pinayev, R. M. Prior,

K. Sabourov, M. Spraker, W. Tornow, Y. Wu, E. A. Wulf, and H. R. Weller. First measurement of the near-threshold ^{2}H$(\gamma, n)p$ analyzing power using a free-electron laser based γ-ray source. *Phys. Rev. C*, 61:061604, May 2000.

[91] H. Schwoerer, P. Gibbon, S. Düsterer, R. Behrens, C. Ziener, C. Reich, and R. Sauerbrey. Mev x rays and photoneutrons from femtosecond laser-produced plasmas. *Phys. Rev. Lett.*, 86:2317–2320, Mar 2001.

[92] H. Schwoerer, B. Liesfeld, H.-P. Schlenvoigt, K.-U. Amthor, and R. Sauerbrey. Thomson-backscattered x rays from laser-accelerated electrons. *Phys. Rev. Lett.*, 96:014802, Jan 2006.

[93] A Shabat and V Zakharov. Exact theory of two-dimensional self-focusing and one-dimensional self-modulation of waves in nonlinear media. *Soviet Physics JETP*, 34(1):62, 1972.

[94] Thomas Sokollik, Satomi Shiraishi, Brian Shaw, Antony Gonsalves, Kei Nakamura, Jeroen van Tilborg, Eric Esarey, Carl B. Schroeder, Carlo Benedetti, Csaba Toth, and Wim Leemans. Staged laser plasma accelerators. *AIP Conference Proceedings*, 1507(1), 2012.

[95] P Sprangle, E Esarey, A Ting, and G Joyce. Laser wakefield acceleration and relativistic optical guiding. *Applied Physics Letters*, 53(22):2146–2148, 1988.

[96] Donna Strickland and Gerard Mourou. Compression of amplified chirped optical pulses. *Optics communications*, 55(6):447–449, 1985.

[97] Guo-Zheng Sun, Edward Ott, Y. C. Lee, and Parvez Guzdar. Self-focusing of short intense pulses in plasmas. *Physics of Fluids (1958-1988)*, 30(2), 1987.

[98] K. Ta Phuoc, S. Corde, C. Thaury, V. Malka, A. Tafzi, J. P. Goddet, R. C. Shah, S. Sebban, and A. Rousse. All-optical compton γ-ray source. *Nat. Photon.*, 6(5):308–311, 05 2012.

[99] T. Tajima and J. M. Dawson. Laser electron accelerator. *Phys. Rev. Lett.*, 43:267–270, Jul 1979.

[100] C Thaury, F Quéré, J-P Geindre, A Levy, T Ceccotti, P Monot, M Bougeard, F Réau, P dOliveira, P Audebert, et al. Plasma mirrors for ultrahigh-intensity optics. *Nature Physics*, 3(6):424–429, 2007.

[101] A Ting, CI Moore, K Krushelnick, C Manka, E Esarey, P Sprangle, R Hubbard, HR Burris, R Fischer, and M Baine. Plasma wakefield generation and electron acceleration in a self-modulated laser wakefield accelerator experiment. *Physics of Plasmas (1994-present)*, 4(5):1889–1899, 1997.

[102] Hai-En Tsai, Chih-Hao Pai, and M. C. Downer. Global optimization of quasi-monoenergetic electron beams from laser wakefield accelerators. *AIP. Conf. Proc.*, 1507(1):330–335, 2012.

[103] Hai-En Tsai, Xiaoming Wang, Joseph M. Shaw, Zhengyan Li, Alexey V. Arefiev, Xi Zhang, Rafal Zgadzaj, Watson Henderson, V. Khudik, G. Shvets, and M. C. Downer. Compact tunable compton x-ray source from laser-plasma accelerator and plasma mirror. *Physics of Plasmas (1994-present)*, 22(2):023106, 2015.

[104] Donald Umstadter, S-Y Chen, A Maksimchuk, G Mourou, and R Wagner. Nonlinear optics in relativistic plasmas and laser wake field acceleration of electrons. *Science*, 273(5274):472–475, 1996.

[105] J van Tilborg, BH Shaw, T Sokollik, S Rykovanov, S Monchocé, F Quéré, Ph Martin, A Malvache, and WP Leemans. Spectral characterization of laser-driven solid-based high harmonics in the coherent wake emission regime. *Optics letters*, 38(20):4026–4029, 2013.

[106] H. Vincenti, S. Monchocé, S. Kahaly, G. Bonnaud, Ph. Martin, and F. Quéré. Optical properties of relativistic plasma mirrors. *Nat Commun*, 5, 03 2014.

[107] Xiaoming Wang, Rafal Zgadzaj, Neil Fazel, Zhengyan Li, S. A. Yi, Xi Zhang, Watson Henderson, Y. Y. Chang, R. Korzekwa, H. E. Tsai, C. H. Pai, H. Quevedo, G. Dyer, E. Gaul, M. Martinez, A. C. Bernstein, T. Borger, M. Spinks, M. Donovan, V. Khudik, G. Shvets, T. Ditmire, and M. C. Downer. Quasi-monoenergetic laser-plasma acceleration of electrons to 2 gev. *Nat. Commun.*, 4, 06 2013.

[108] K. J. Weeks, V. N. Litvinenko, and J. M. J. Madey. The compton backscattering process and radiotherapy. *Med. Phys.*, 24(3):417–423, 1997.

[109] S. C. Wilks, W. L. Kruer, M. Tabak, and A. B. Langdon. Absorption of ultra-intense laser pulses. *Phys. Rev. Lett.*, 69:1383–1386, Aug 1992.

[110] Y. C. Wu, B. Zhu, K. G. Dong, Y. H. Yan, and Y. Q. Gu. Note: Absolute calibration of two drz phosphor screens using ultrashort electron bunch. *Rev. Sci. Instrum.*, 83(2):026101, 2012.

[111] Ch. Ziener, P. S. Foster, E. J. Divall, C. J. Hooker, M. H. R. Hutchinson, A. J. Langley, and D. Neely. Specular reflectivity of plasma mirrors as a function of intensity, pulse duration, and angle of incidence. *J. App. Phys.*, 93(1):768–770, 2003.

Vita

Hai-En Tsai was born in Kaohsiung, Taiwan. He received the Bachelor of Science degree in Physics in July, 2002 and Master of Science degree in Optical Engineering in July, 2005 from the National Taiwan University. From 2005 to 2009, he was hired by Au Optronics Corporation as a senior optical engineer in Shin-Chu, Taiwan. He was accepted and started graduate studies in the University of Texas at Austin in August, 2009.

Permanent address: 2600 Gracy Farms Lane, Apt 334
Austin, Texas 78758

This dissertation was typeset with LaTeX[†] by the author.

[†]LaTeX is a document preparation system developed by Leslie Lamport as a special version of Donald Knuth's TeX Program.